Max-Planck-Institut für
Biogeochemie

TECHNICAL REPORTS
23

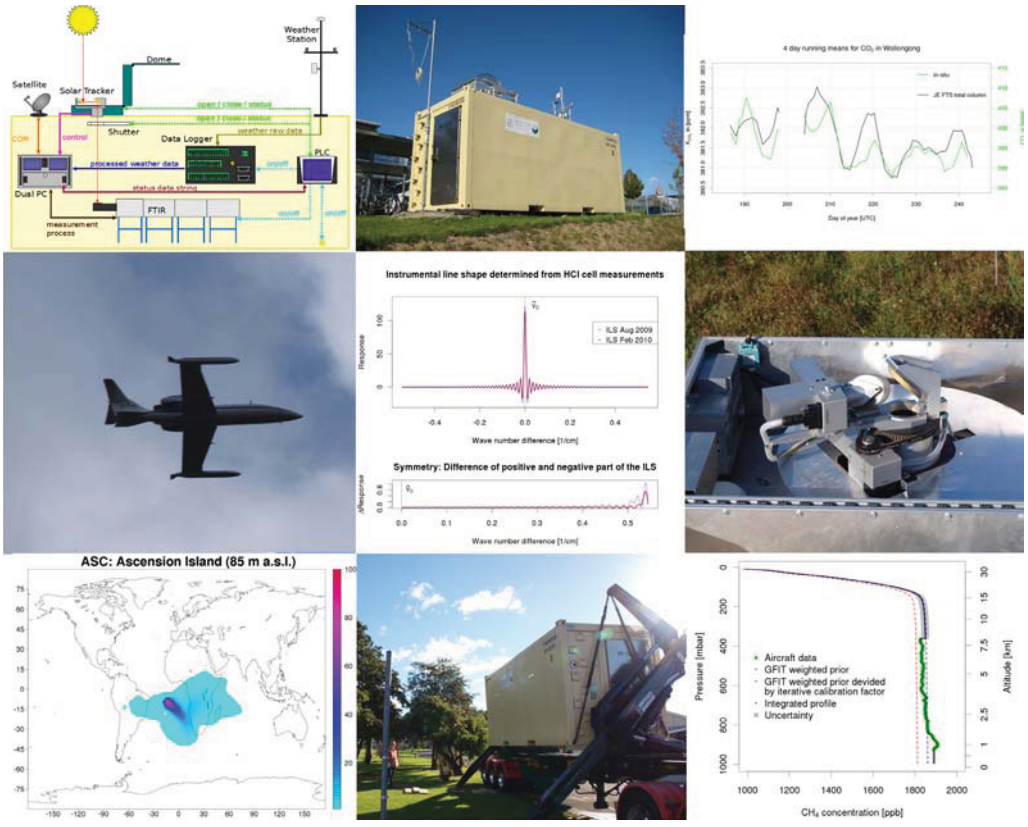

Measurement of climate-relevant trace gases via infrared spectroscopy

by
Marc Geibel

ISSN 1615-7400

MAX-PLANCK-GESELLSCHAFT

Technical Reports - Max-Planck-Institut für Biogeochemie 23, 2011

Max-Planck-Institut für Biogeochemie
P.O.Box 10 01 64
07701 Jena/Germany
phone: +49 3641 576-0
fax: + 49 3641 577300
http://www.bgc-jena.mpg.de

Measurement of climate-relevant trace gases via infrared spectroscopy

Atmospheric Remote Sensing Group

by

Marc Christoph Geibel

This work has been submitted as a PhD thesis to the Faculty of Chemical and Earth Sciences, Friedrich Schiller University Jena,
and was sucessfully defended on 15.06.2011.

”Eine neue wissenschaftliche Wahrheit pflegt sich nicht in der Weise durchzusetzen, daß ihre Gegner überzeugt werden und sich als belehrt erklären, sondern vielmehr dadurch, daß ihre Gegner allmählich aussterben und daß die heranwachsende Generation von vornherein mit der Wahrheit vertraut gemacht ist.”

MAX PLANCK (1858-1947)

Contents

List of Figures

List of Tables

List of Abbreviations

AC	alternating current
AK	averaging kernel
ARS	Atmospheric Remote Sensing group of the MPI-BGC Jena
AT	air temperature
BGC	Biogeochemistry
CIA	collision induced absorptions
CSIRO	Commonwealth Scientific and Industrial Research Organisation, Australia
DC	direct current
DIC	dissolved inorganic carbon
DMF	dry air mole fraction
ESRL	Earth System Research Laboratory
ESSP	Earth System Science Pathfinder
FFT	fast Fourier transformation
FTIR	Fourier transform infrared
FTS	Fourier transform spectrometer

GFIT	TCCON retrieval software
GH	geopotential height
GOSAT	Greenhouse Gases Observing Satellite
GWP	global warming potential
HITRAN	High Resolution Transmission database
IR	infrared
ILS	instrumental line shape
IMECC	Infrastructure for Measurements of the European Carbon Cycle
IPCC	Intergovernmental Panel on Climate Change
IPP	Interferogram Processing Software
NASA	National Aeronautics and Space Administration
NCEP	National Centers for Environmental Prediction
NDIR	non-dispersive infrared
NIES	National Institute for Environmental Studies, Japan
NIR	near ifrared
NOAA	National Oceanic and Atmospheric Administration, USA
OCO	Orbiting Carbon Observatory
OPD	optical path difference
PBL	planetary boundary layer
PLC	Programmable Logic Controller

SCIAMACHY	Scanning Image Absorption Spectrometer for Atmospheric Cartography
SH	specific humidity
SIC	solar intensity variations
SZA	solar zenith angle
TCCON	Total Carbon Column Observation Network
TP	tropopause pressure
UoW	University of Wollongong, Australia
UPS	Uninterruptible Power Supply
VMR	volume mixing ratio
ZOTTO	Zotino Tall Tower Observation Facility
ZPD	zero path difference

Definitions

Units

Definition	Unit	Abbreviation
parts per billion	nMol/Mol	**ppb**
parts per million	μMol/Mol	**ppm**

Physical quantities

Quantity	Definition	Unit	Symbol
wavelength		$\mathbf{nm}$	λ
wavenumber	$1/\lambda$	$\mathbf{cm^{-1}}$	ν

Total column abundance: Dry air mole fraction

Abbreviation	Definition	Symbol
DMF	Fraction of moles of a particular component of air divided by the total number of moles of gas in the same sample. The calculation does not include water vapor in the air sample.	X_{gas}

Abstract

This work introduces a new fully automated FTIR system for ground-based total column measurements of atmospheric greenhouse gases. It is part of the Total Carbon Column Observation Network (TCCON), which has the main role to provide data for calibration and validation of satellite based measurements of greenhouse gases. This work describes the development of the system in three parts: design and setup, calibration, and testing.

Chapter 2 describes the principal components and the design concept of the system. The focus lies on reliability and low maintenance effort to facilitate operation at remote sites. This is realized through the interaction of independent subsystems that are kept as simple as possible. Critical components are redundant as much as possible.

To monitor the instrument's stability, the instrumental line shape of the FTIR is determined from HCl cell measurements. These measurements show that during a period of six months this ILS changes only slightly. From these results one can expect that – once aligned – the instrument will be very stable over long time periods.

During the installation phase at Jena, Germany, the instrument measured column-averaged X_{CO_2}, X_{CO} and X_{CH_4}. Compared to ground-based in-situ CO_2 VMR measurements, the FTIR total column X_{CO_2} show an expected offset in the morning which mostly disappeared with the breakup of the nighttime planetary boundary

layer. This effect demonstrates the reduced sensitivity of X_{CO_2} measurements to mixing processes in the planetary boundary layer and confirms results of model simulations. Otherwise, the X_{CO_2} measurements show a distinct diurnal cycle. A part of seasonal cycle measured over Jena during the installation phase corresponded to TM3 simulation results that were extrapolated to 2009 values.

After the system was set up, it took part in the IMECC aircraft campaign. Goal of this campaign was to calibrate six European TCCON instruments to o an existing network of in-situ measurements of greenhouse gases. The results of this campaign are presented in Chapter 3. For CH_4 the earlier calibration factor from Wunch et al. (2010) can be confirmed. By adding the IMECC calibration points to the dataset, the uncertainty in the derivation of the calibration factor is reduced by $\sim 68\%$. The assumption of a uniform calibration factor for the whole TCCON network is verified.

A sensitivity study shows, that the limited vertical coverage of the aircraft data has an impact on the calibration factor, resulting in biased estimates. To address this, an iterative method was developed to determine the calibration factor. A test of this approach shows, that the calibration factor derived by the classical method introduces a $\sim 7\mathbf{ppb}$ offset for the FTS DMFs which could be removed by the iterative method. Further investigation will assess, whether a generalization of this approach for other species such as CO_2 is suitable.

In Chapter 4 the results of a measurement campaign in Wollongong, Australia, are presented. Goal of this campaign was the intercomparison to a similar instrument of the University of Wollongong (UoW) and the assessment of setup procedures under field conditions in order to prepare long term deployment at remote locations.

After transport, the spectrometer was severely misaligned but could be realigned to TCCON standards. A time series of spectral data could be acquired,

containing nearly 2800 measurements. Compared to measurements from the instrument of the UoW, the data analysis shows a larger scatter in the data of the Jena FTS. This is caused by oscillations of the solar tracker that lead to differences between true and calculated airmass. For the intercomparison, the scatter can be annihilated by the calculation of daily median values. At the current state, no quality control of the Jena FTS data is performed and the data of both instruments are processed with different versions of the TCCON retrieval software (GFIT). Despite this, the resulting correlation shows that for the majority of the data both instruments agree within TCCON requirements.

For further analysis, a quality control of the data of the Jena FTS has to be established. Besides that, the scatter of the data has to be reduced. A possible solution for this problem might be the filtering of the low-frequency oscillation of the solar tracker in the interferograms. For this, the interferogram preprocessing software (IPP) needs to be modified. Furthermore, a uniform data processing with the same GFIT version for the data of both FTS is indispensable, since this eliminates offsets created by unequal spectroscopy.

Once the pointing problems of the Solar Tracker are solved, respectively their effects are compensated and other minor damages are repaired, the system is ready to be set up at its final destination Ascension Island. There it will be able to contribute to TCCON and to serve as a validation source for current and upcoming satellite missions. However, the data processing and pre-screening is to be improved to maximize the quality of the output products. For the long-term operation of the system, the experience of this campaign shows, that it is crucial to keep the solar tracker mirrors clean. To identify possible contamination of the solar tracker mirrors, the intensity of the quadrant diode has to be checked and - if necessary - a cleaning of the mirrors has to be performed.

Chapter 1

Introduction

1.1 Overview

The anthropogenic climate change is probably one of the most fundamental tasks for mankind to cope with. In the past 100 years, the mean global temperature has risen by 0.74 +/-0.18 $^{\circ}\mathrm{C}$ (Solomon et al. (2007), Brohan et al. (2006)). The slope of this temperature rise is increasing throughout the recent years. Large parts of the trend of global warming can be explained by anthropogenic effects (Lean and Rind, 2009). An increase in temperature leads to interaction with other aspects of the Earth's climate. Investigations show indications of increased strength and frequency of extreme weather events and changes in precipitation (Parry et al. (2007), Rosenzweig et al. (2008)). Besides that, there are signs of rising sea levels as well as melting of glaciers and permafrost.

Responsible for the Earth's temperature are two factors: The incoming solar radiation and Earth's reflecting and absorbing behavior. The amount of energy absorbed by the Earth's surface is about 240 $\mathbf{Wm^{-1}}$. To balance this incoming energy the Earth emits long-wave radiation (IR). Without the atmosphere, the emission of 240 $\mathbf{Wm^{-1}}$ would correspond to a sourface temperature of -19 $^{\circ}\mathrm{C}$.

The actual Earth surface temperature, however, is much higher (on average about 14 °C).

Atmospheric trace gases like CO_2, N_2O, CH_4, O_3, and H_2O are able to absorb energy in the IR. They absorb some of the Earth's re-emitted energy, and themselves re-emit energy diffuse in all directions. By this effect theses gases in their natural concentrations increase the surface temperature by ∼33 °C and make the planet habitable. These effect is called the natural greenhouse effect.

This natural effect has been severely altered by humans since the beginning of the industrial revolution. Due to the excessive combustion of fossil fuel, land-use change and deforestation, the amount of of greenhouse gases have increased drastically. This man-made change in concentration of the greenhouse gases is called the anthropogenic greenhouse effect.

The influence of individual greenhouse gases on the anthropogenic greenhouse effect depends on their atmospheric abundance and lifetime, and their radiative efficiency. The radiative efficiencies of the major greenhouse gases and their global warming potential (GWP) in relation to CO_2 are shown in Table 1.1.

Table 1.1: Radiative efficiency and global warming potential (GWP) for selected species on a 100 year time horizon as presented by the IPCC (Solomon et al. (2007)).

Species	Lifetime [years]	radiative Efficiency [$Wm^{-2}ppb^{-1}$]	GWP (100 yr)
CO_2	varying	1.4×10^{-5}	1
CH_4	12	3.7×10^{-4}	25
N_2O	114	3.03×10^{-3}	298

In the last 200 years the amount of atmospheric CH_4 more than doubled from the pre-industrial values of $\sim$ 700 $\mathbf{ppb}$ to now more than 1774 $\mathbf{ppb}$ (Solomon et al., 2007). Atmospheric CO_2 has been increased by 35% within the same time.

To understand the influence of this increase on Earth's temperature and climate one has to understand the global carbon cycle.

1.2 The global carbon cycle

The global carbon cycle plays a very important role in climate change since two major anthropogenic greenhouse gases CO_2 and CH_4 are carbon-based molecules. To be able to predict and diminish the present and future climate change, the understanding of the carbon cycle is indispensable.

The global carbon cycle refers to the cycling of carbon through soil, water and atmosphere on different temporal and spatial scales (see Fig. 1.1).

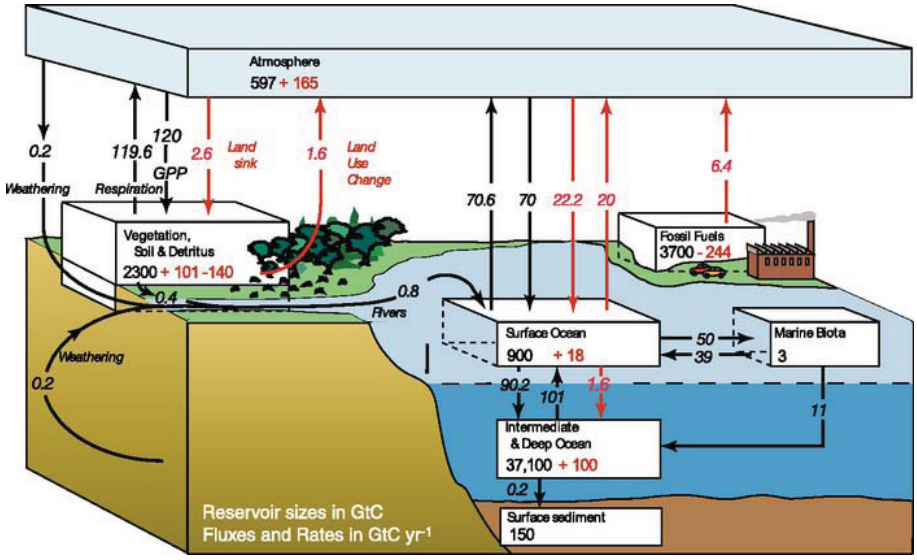

Figure 1.1: Illustration of the global carbon cycle. The numbers are taken from the IPCC (Solomon et al. (2007)).

In this illustration natural fluxes are symbolized by black arrows. The numbers show, that these fluxes are nearly balanced. Anthropogenic contributions to the carbon cycle are symbolized by red arrows. The biggest reservoir, the sedimentary

rocks, contain about 80 % of the total carbon amount in the form of carbonate and organic compounds. Second biggest reservoir is the ocean that contains dissolved inorganic carbon (DIC). This reservoir contains over 50 times more carbon than the atmosphere.

Although the numbers of the anthropogenic contributions are quite small compared to the natural fluxes, they cause an imbalance. The reason for that is that they mainly affect the relatively small reservoir of the atmosphere. This leads to an accumulation of carbon in form of CO_2 and CH_4 in the atmosphere. The reaction of the natural fluxes (e.g. the role of the ocean) to that increase is not yet fully understood.

1.3 Surface measurement networks

Since the fluxes of the carbon cycle can not be measured directly, the best approach to quantify the anthropogenic change is to measure the atmospheric concentration of CO_2 and CH_4 in the atmosphere. The longest record of surface measurements of atmospheric CO_2 has the Mauna Loa Observatory, Hawaii (Keeling et al. (1976), Keeling and Whorf (2005)). It started observations in 1968 and the record illustrates the change in atmospheric CO_2 very clear (see. Fig. 1.2). In the last 50 years the CO_2 concentration increased by $\sim$60 $\mathbf{ppm}$.

In the last two decades, the number of surface measurement stations increased to over 100, forming a relatively dense global network (see Fig. 1.3) that is operated by institutions like NOAA ESRL, CSIRO, NIES and the MPI for Biogeochemistry.

Products like CarbonTracker (Peters et al. (2007)) and GLOBALVIEW-CO2 (GLOBALVIEW-CO2, Masarie and Tans (1995)) use the data from a global surface network and the results of global transport models (Gurney et al. (2002),

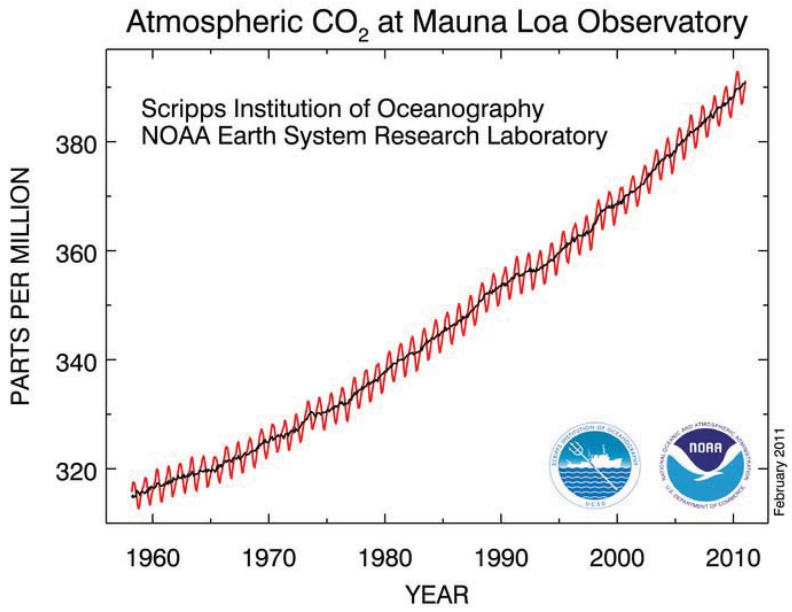

Figure 1.2: Observational record of CO_2 in-situ measurements at Manua Loa, Hawaii (Tans, 2011). The black line shows the trend,the red line the concentration with seasonal variability.

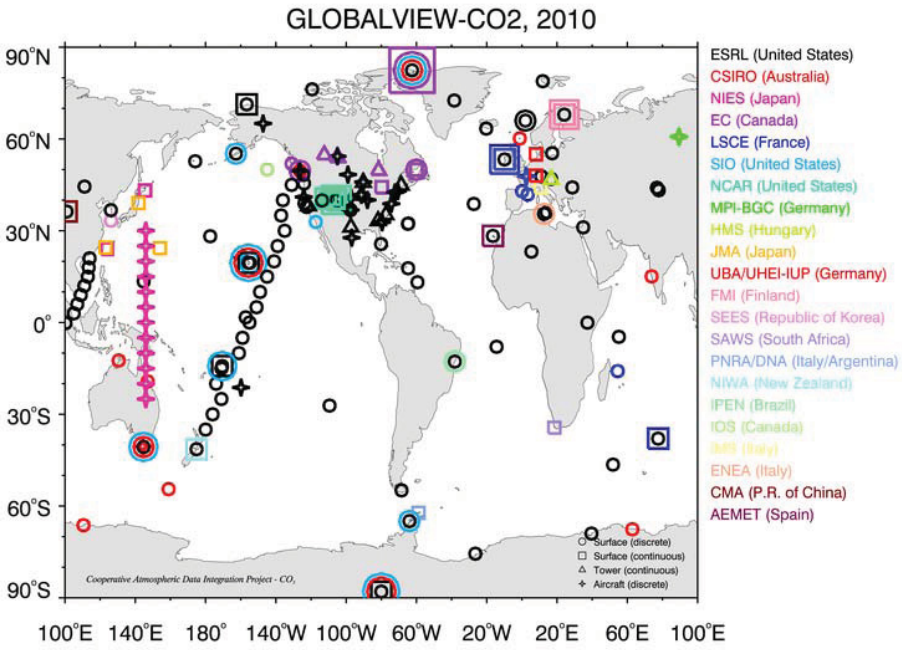

Figure 1.3: Illustration of the global distribution of sampling locations for measurement records used to derive GLOBALVIEW-CO2. This figure is taken from GLOBALVIEW-CO2.

Rayner et al. (1999), Tans et al. (1990)) to create surface flux estimations of CO_2 on regional to global scales.

The main advantages of the surface measurements are that they are highly accurate and that they can be obtained with moderate effort even in remote locations. A major disadvantage is that they can be strongly influenced by local sources and sinks. Besides, they can only provide measurements from within the atmospheric boundary layer. Tall towers, like those from MPI for Biogeochemistry in Bialystok (Poland, Popa et al. (2010)), Ochsenkopf (Germany, Thompson et al. (2009)) and ZOTTO (Siberia, Winderlich et al. (2010)), give the opportunity to perform measurements at different height levels (usually $< 300\ \mathrm{m}$). This allows to measure air that represents a larger influence area. However, they are still measuring most of the time in the planetary boundary layer (PBL). Despite the high accuracy of the measurements themselves, imperfect representation of vertical mixing near the surface in atmospheric transport models still leads to large uncertainties in modeled tracer mixing ratios (Gerbig et al., 2008).

Measurements of total column dry mole fractions are less affected by spatial and temporal variability than near-surface in situ data. Nevertheless, they still retain information about surface fluxes (Gloor et al., 2000). Those measurements can be performed by satellites or ground-based Fourier Transform Infrared (FTIR) spectrometers (see Sections 1.5 and 1.7).

1.4 Atmospheric remote sensing from space

Although the global in-situ network is quite dense and provides accurate measurements, it is affected by local sources and sinks and is still unable to achieve global coverage. Remote sensing of greenhouse gases from space offers the opportunity to solve both problems. There are several different techniques and spacecrafts

(Bréon and Ciais, 2010). The most prominent satellite instruments are:

- The **Scanning Image Absorption Spectrometer for Atmospheric Cartography (SCIAMACHY)** on ENVISAT. It was launched in 2002 and has eight sensor channels that cover the spectral area from ultra-violet (240 $\mathbf{nm}$) to short-wave infrared (2380 $\mathbf{nm}$) with a resolution of 0.2 - 1.5 $\mathbf{nm}$. The maximum spatial resolution of the instrument is 26 $\mathbf{km}$ x 15 $\mathbf{km}$ in Nadir mode (Bovensmann et al. (1999), http://www.iup.uni-bremen.de/sciamachy/). The broad spectral coverage allows the detection of trace gases, clouds and aerosols.

- The **Greenhouse Gases Observing Satellite (GOSAT)**. It was launched in 2009 and as a joint-venture of Japanese Space Agency (JAXA) and the National Institute for Environmental Studies (NIES). The satellite is equipped with two sensors: a thermal and near-infrared Fourier Transform Spectrometer (TANSO-FTS) and a cloud and aerosol imager (TANSO-CAI) (Kuze et al., 2009). The TANSO-FTS has three narrow bands in the short-wave infrared region (0.76, 1.6, and 2.0 $\mu\mathbf{m}$) and a wide thermal infrared band (5.5 $\mu\mathbf{m}$ - 14.3 $\mu\mathbf{m}$) at a spectral resolution of $\sim$0.2 $\mathbf{cm^{-1}}$. The spatial maximum resolution of the TANSO-CAI is 0.5 $\mathbf{km}$ (1.5 $\mathbf{km}$ for channel 4) and 10.5 $\mathbf{km}$ for the TANSO-FTS. The retrieval of the acquired data provides column-averaged dry air mole fractions (DMFs) of CO_2 and CH_4.

- The **Orbiting Carbon Observatory (OCO)** of NASA's Earth System Science Pathfinder (ESSP) program (Crisp et al., 2004). The design of OCO is based on three parallel, high-resolution spectrometers to measure the O_2 A-band at 0.76 $\mu\mathbf{m}$ and the CO_2 bands at 1.61 and 2.06 $\mu\mathbf{m}$. The maximum spatial resolution is 1.29 $\mathbf{km}$ x 2.25 $\mathbf{km}$. For the retrieved column-averaged CO_2 DMFs the targeted precision of the is 1 $\mathbf{ppm}$ on regional scales. The

satellite was launched in 2009 but failed reaching its orbit. The replacement, OCO-2, is announced to be launched 2013.

Measurements performed by satellites, however, have to be validated and calibrated. This task can be fulfilled by the Total Carbon Column Observation Network (TCCON).

1.5 The Total Carbon Column Observing Network (TCCON)

The Total Carbon Column Observing Network (TCCON) is an association of ground-based Fourier Transform Spectrometer (FTS) systems. It was formed to deliver highly precise and accurate high-resolution near-infrared (NIR) spectral data. From these, total column dry mole fractions (DMF) of CH_4, CO, CO_2, HF, HCl, HDO, H_2O and N_2O are retrieved. O_2 can also be retrieved, similarly to the OCO retrieval. TCCON currently consists of 18 different FTS stations that are spread globally. The global coverage, however, is still to be improved. A map of present, future and possible TCCON sites is shown in Figure 1.4.

Figure 1.4: Global map showing present and future sites in the TCCON.

The targeted precision of CO_2 total column DMFs is $\sim$0.25% (< 1 ppm) (Wunch et al., 2011). The instruments that are used in TCCON are Bruker IFS 125HR spectrometers equipped with room-temperature Indium Gallium Arsenide (InGaAs) and Silicon (Si) detectors. With these detectors the entire spectral region from 3900 to 15500 $\mathbf{cm^{-1}}$ is covered simultaneously with a spectral resolution of 0.02 $\mathbf{cm^{-1}}$.

TCCON complements the in-situ measurement network by delivering column integrals of the CO_2 volume mixing ratios (VMR) profiles that are less sensitive to diurnal variations in atmospheric boundary layer height and details of vertical transport in general (Gerbig et al., 2008). However, the reduced sensitivity of total column measurements makes the identification of seasonal and latitudinal variations challenging.

TCCON stations also refer as validation source for satellite instruments like GOSAT (Yokota et al., 2009) and the upcoming OCO II. Unlike surface measurements, the data can be used directly for the validation since the data product (total column abundances) is similar.

1.6 IR absorption of greenhouse gases

To be categorized as a greenhouse gas, a species must be able to absorb photons in the infrared spectrum. This absorption takes place at frequencies that are distinctive for the individual species creating so called absorption lines. Different vibrational states of the molecule lead to changes in the electric dipole momentum. This allows the molecule to interact with electromagnetic radiation by absorbing or emitting photons of certain frequencies.

Linear molecules have less vibrational degrees of freedom than non-linear molecules. Heteronuclear diatomic molecules like CO are able to absorb in the

infrared spectrum but have only one vibrational mode. In contrast, the vibrational mode of homonuclear diatomic molecules like N_2 can not be observed in the infrared spectrum. These molecules have no distinct absorption lines. However, collisions with other molecules can cause a temporal change electric dipole momentum. This allows collision induced absorptions (CIA) at a broader spectral range.

An exception is O_2 which has absorption lines in the infrared even though it is a homonuclear diatomic molecule. It has two unpaired electron spins creating a magnetic dipole moment (Janssen, 1993). Thus, O_2 interacts with electromagnetic radiation but the effect is much weaker than the effect of a electric dipole moment. Nevertheless, the vast amount of O_2 molecules in the atmosphere makes a detection of this absorption possible.

1.7 Fourier transform infrared spectroscopy

The principle of Fourier Transform Infrared (FTIR) spectroscopy is based on a two-beam Michelson interferometer. A schematic overview of that interferometer type is shown in Figure 1.5. The heart of this interferometer is a beam splitter that divides the incoming beam of radiation into two paths. One path travels to a fixed mirror, while the other goes to a movable mirror (scanner mirror). This scanner is used to introduce an optical path difference (OPD) δ in the distance the beams travel. The beams A and B (see Figure 1.5) are re-combined and passed to a detector that measures the light intensity.

The resulting interference pattern is a function of intensity over OPD and is dependent on the wavelength λ of the source radiation. Total constructive interference is achieved for:

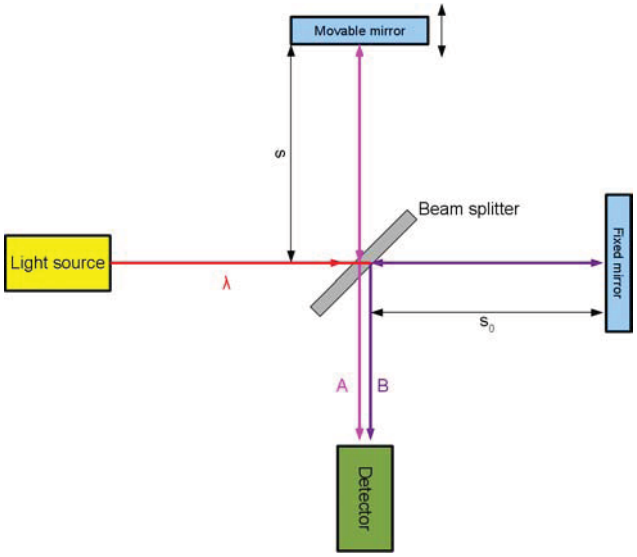

Figure 1.5: Principle of a Michaelson interferometer. The optical path difference (OPD) is defined as: OPD = $\delta = \frac{s-s_0}{2}$.

$$OPD = n\lambda \; with \; n \in \mathbb{N} \tag{1.1}$$

Total destructive interference is achieved for:

$$OPD = (2n+1)\frac{\lambda}{2} \; with \; n \in \mathbb{N} \tag{1.2}$$

Assuming both partial beams have the same maximum amplitude ξ_{max}, the amplitude ξ_A of partial beam A follows:

$$\xi_A(t) = \xi_{max} \; sin(\omega t + \varphi) \tag{1.3}$$

with ω - angular frequency, t - time, φ - phase

Further assuming the scanner mirror is moving with a constant velocity, the amplitude ξ_B of partial beam B follows:

$$\xi_B(t) = \xi_{max}\ sin\left(\omega t + \varphi + \frac{2\pi\ \delta}{\lambda}\right) \tag{1.4}$$

with ω - angular frequency, t - time, φ - phase, δ - optical path difference (OPD), λ - wavenumber of incoming radiation

This leads to an amplitude at the detector ξ_D of:

$$\xi_D(t,\delta) = 2\ \xi_{max}\ cos\left(\frac{\pi\ \delta}{\lambda}\right) sin\left(\omega t + \varphi + \frac{2\pi\ \delta}{\lambda}\right) \tag{1.5}$$

The maximum amplitude at the detector ξ_0 is

$$\xi_0 = 2\ \xi_{max}\ cos\left(\frac{\pi\ \delta}{\lambda}\right) \tag{1.6}$$

The intensity for electromagnetic waves can be derived from

$$I = \frac{c\ \epsilon_0\ \xi_0^2}{2} \tag{1.7}$$

with c - speed of light, ϵ_0 - electric constant

The combination of Equations 1.6 and 1.7 leads to

$$I'(\delta) = c\ \epsilon_0\ \xi_{max}^2\ cos^2\left(\frac{\pi\ \delta}{\lambda}\right)\ =\ I_0(\lambda)\ cos^2\left(\frac{\pi\ \delta}{\lambda}\right) \tag{1.8}$$

This equation can be rewritten to

$$I'(\delta) =\ \frac{I_0(\lambda)}{2}\left(1\ +\ cos\frac{2\ \pi\ \delta}{\lambda}\right)\ =\ \frac{I_0(\tilde{\nu})}{2}\left(1\ +\ cos\ 2\ \pi\ \delta\ \tilde{\nu}\right) \tag{1.9}$$

with $\tilde{\nu} = \frac{1}{\lambda}$ - wave number

The resulting Equation 1.9 however is only valid for an theoretical instrument with an ideal beam splitter and perfect detector response. For a real instrument,

the equation has to be modified with a wavenumber-dependent correction factor $H(\tilde{\nu})$ (Griffiths and de Haseth, 1986).

$$I'(\delta) = \frac{I_0(\tilde{\nu})\ H(\tilde{\nu})}{2}\,(1\ +\ cos\ 2\ \pi\ \delta\ \tilde{\nu}) \tag{1.10}$$

Equation 1.10 illustrates that the intensity as a function of OPD (hence a function of time assuming a constant scanner mirror velocity) consists of a DC term, dependent on the intensity of the source, modulated by an AC term containing the periodical wavelength dependent information.

Setting $\frac{1}{2}\ I_0(\tilde{\nu})\ H(\tilde{\nu})$ equal to $B(\tilde{\nu})$ (effective source intensity), the AC term can be simplified to

$$I(\delta) = \ B(\tilde{\nu})\ cos\ 2\ \pi\ \delta\ \tilde{\nu} \tag{1.11}$$

Leaving the DC term aside, mathematically, $I(\delta)$ is the cosine Fourier transform of $B(\tilde{\nu})$. This allows to calculate a spectrum from the interferogram by computing the cosine Fourier transform of $I(\delta)$.

Fourier transform spectroscopy has the advantage to sample the entire spectrum simultaneously (multiplex advantage). This reduces sample time and helps to increase the signal-to-noise ratio (SNR).

The resolution of a Fourier Transform Spectrometer (FTS) is its ability to resolve spectral absorption lines separated by a wavenumber difference of $\Delta\nu\ \mathbf{cm^{-1}}$. The resolution is limited by the OPD and it holds: $\Delta\nu \sim OPD^{-1}$.

1.8 Thesis objectives

The goal of this thesis was to develop and build a fully automated FTIR system for total column measurements of atmospheric trace gases. As part of TCCON, it is planned to install the system in the tropics where such measurements are very sparse.

The designated site is Ascension Island, a British oversea territory in the South Atlantic. This unique location should provide excellent observation conditions for the FTIR instrument. Due to its small size and very scarce vegetation, the influence from local sources and sinks on the CO_2 and CH_4 measurements should be minimal.

This work describes the history of the system in three parts:

Development

Chapter 2 introduces the design of the system: chosen components and self-made parts like a custom solar tracker protection dome are explained and the automation concept of the system is illustrated. Besides that, first results of total column measurements in Jena are presented.

Calibration

In 2009, after the Jena FTIR system was completed, it took part in the IMECC aircraft calibration campaign. The integration of the FTIR measurements into the existing ground-based in-situ network requires a calibration. Earlier campaigns (Wunch et al., 2010) pointed out that it is highly likely that there is a species-specific uniform calibration factor for all TCCON FTIR systems. The goal of the IMECC aircraft campaign was to verify these findings and to calibrate six of the European TCCON stations. The results of the CH_4 calibration are presented in Chapter 3.

Testing

After successfully taking part in the calibration campaign, the FTIR system was shipped to Australia for a test campaign. The aim was to prove the systems functionality and to compare the measurements of the system to the ones performed by a similar instrument operated by the University of Wollongong (UoW), Australia. The results of this campaign are presented

in Chapter 4.

Bibliography

Bovensmann, H., Burrows, J. P., Buchwitz, M., Frerick, J., Noël, S., Rozanov, V. V., Chance, K. V., and Goede, A. P. H.: SCIAMACHY: Mission Objectives and Measurement Modes, Journal of the Atmospheric Sciences, 56, 127–150, doi:10.1175/1520-0469(1999)056⟨0127:SMOAMM⟩2.0.CO;2, URL http://journals.ametsoc.org/doi/abs/10.1175/1520-0469%281999%29056%3C0127%3ASMOAMM%3E2.0.CO%3B2, 1999.

Bréon, F.-M. and Ciais, P.: Spaceborne remote sensing of greenhouse gas concentrations, Comptes Rendus Geoscience, 342, 412 – 424, doi:DOI:10.1016/j.crte.2009.09.012, URL http://www.sciencedirect.com/science/article/B6X1D-4Y0TDTH-1/2/557d34da1cd49b4bb328a444bcc5dbe9, atmosphére vue de l'espace, 2010.

Brohan, P., Kennedy, J. J., Harris, I., Tett, S. F. B., and Jones, P. D.: Uncertainty estimates in regional and global observed temperature changes: A new data set from 1850, J. Geophys. Res., 111, doi:10.1029/2005JD006548, 2006.

Crisp, D., Atlas, R. M., Breon, F. M., Brown, L. R., Burrows, J. P., Ciais, P., Connor, B. J., Doney, S. C., Fung, I. Y., Jacob, D. J., Miller, C. E., O'Brien, D., Pawson, S., Randerson, J. T., Rayner, P., Salawitch, R. J., Sander, S. P., Sen, B.,

Stephens, G. L., Tans, P. P., Toon, G. C., Wennberg, P. O., Wofsy, S. C., Yung, Y. L., Kuang, Z., Chudasama, B., Sprague, G., Weiss, B., Pollock, R., Kenyon, D., and Schroll, S.: The Orbiting Carbon Observatory (OCO) mission, Advances in Space Research, 34, 700 – 709, doi:DOI:10.1016/j.asr.2003.08.062, URL http://www.sciencedirect.com/science/article/B6V3S-4C7DC5T-F/2/2cc8ffed09701a5cf111c2b339c28f59, trace Constituents in the Troposphere and Lower Stratosphere, 2004.

Gerbig, C., Körner, S., and Lin, J. C.: Vertical mixing in atmospheric tracer transport models: error characterization and propagation, Atmos. Chem. Phys., 8, 591–602, doi:10.5194/acp-8-591-2008, 2008.

GLOBALVIEW-CO2: Cooperative Atmospheric Data Integration Project - Carbon Dioxide. CD-ROM, NOAA ESRL, Boulder, Colorado, URL ftp://ftp.cmdl.noaa.gov/ccg/co2/GLOBALVIEW, 2010.

Gloor, M., Fan, S.-M., Pacala, S., and Sarmiento, J.: Optimal sampling of the atmosphere for purpose of inverse modeling: A model study, Global Biogeochem. Cycles, 14, 407–428, doi:10.1029/1999GB900052, 2000.

Griffiths, P. R. and de Haseth, J. A.: Fourier Transform Infrared Spectrometry, Wiley-Interschience, 1986.

Gurney, K. R., Rachel M. Law, A. S. D., Rayner, P. J., Baker, D., Bousquet, P., Bruhwiler, L., Chen, Y.-H., Ciais, P., Fan, S., Fung, I. Y., Gloor, M., Heimann, M., Higuchi, K., John, J., Maki, T., Maksyutov, S., Masarie, K., Peylin, P., Prather, M., Pak, B. C., Randerson, J., Sarmiento, J., Taguchi, S., Takahashi, T., and Yuen, C.-W.: Towards robust regional estimates of CO_2 sources and sinks using atmospheric transport models, Nature, 415, 626–630, doi:10.1038/415626a, 2002.

Janssen, M. A.: Atmospheric Remote Sensing by Microwave Radiometry, Wiley-Interschience, 1993.

Keeling, C. D. and Whorf, T. P.: A Compendium of Data on Global Change, chap. Atmospheric CO2 records from sites in the SIO air sampling network, U.S. Department of Energy, Oak Ridge, Tenn., U.S., 2005.

Keeling, C. D., Bacastow, R. B., Bainbridge, A. E., Ekdahl, C. A., Guenther, P. R., Waterman, L. S., and Chin, J. F. S.: Atmospheric carbon dioxide variations at Mauna Loa Observatory, Hawaii, Tellus, 28, 538–551, doi:10.1111/j.2153-3490.1976.tb00701.x, URL http://dx.doi.org/10.1111/j.2153-3490.1976.tb00701.x, 1976.

Kuze, A., Suto, H., Nakajima, M., and Hamazaki, T.: Thermal and near infrared sensor for carbon observation Fourier-transform spectrometer on the Greenhouse Gases Observing Satellite for greenhouse gases monitoring, Appl. Opt., 48, 6716–6733, doi:10.1364/AO.48.006716, URL http://ao.osa.org/abstract.cfm?URI=ao-48-35-6716, 2009.

Lean, J. L. and Rind, D. H.: How will Earth's surface temperature change in future decades?, Geophys. Res. Lett., 36, doi:10.1029/2009GL038932, l15708, 2009.

Masarie, K. A. and Tans, P. P.: Extension and integration of atmospheric carbon dioxide data into a globally consistent measurement record, J. Geophys. Res., 100, doi:10.1029/95JD00859, 1995.

Parry, M., Canziani, O.F. andPalutikof, J., van der Linden, P., and Hanson, C., eds.: IPCC Fourth Assessment Report: Climate Change 2007 (AR4), chap. Working Group II: Impacts, Adaptation and Vulnerability, Cambridge University Press, Cambridge, United Kingdom and New York, NY, USA., 2007.

Peters, W., Jacobson, A. R., Sweeney, C., Andrews, A. E., Conway, T. J., Masarie, K., Miller, J. B., Bruhwiler, L. M. P., Pétron, G., Hirsch, A. I., Worthy, D. E. J., van der Werf, G. R., Randerson, J. T., Wennberg, P. O., Krol, M. C., and Tans, P. P.: An atmospheric perspective on North American carbon dioxide exchange: CarbonTracker, PNAS, 104, 18 925–18 930, 2007.

Popa, M. E., Gloor, M., Manning, A. C., Jordan, A., Schultz, U., Haensel, F., Seifert, T., and Heimann, M.: Measurements of greenhouse gases and related tracers at Bialystok tall tower station in Poland, Atmospheric Measurement Techniques, 3, 407–427, doi:10.5194/amt-3-407-2010, URL `http://www.atmos-meas-tech.net/3/407/2010/`, 2010.

Rayner, P. J., Enting, I. G., Francey, R. J., and Langenfelds, R.: Reconstructing the recent carbon cycle from atmospheric CO_2, $\delta^{13}C$ and O_2/N_2 observations, Tellus, 51B, 213–232, doi:10.1034/j.1600-0889.1999.t01-1-00008.x, 1999.

Rosenzweig, C., Karoly, D., Vicarelli, M., Neofotis, P., Wu, Q., Casassa, G., Menzel, A., Root, T. L., Estrella, N., Seguin, B., Tryjanowski, P., Liu, C., Rawlins, S., and Imeson, A.: Attributing physical and biological impacts to anthropogenic climate change, Nature, 453, 353 – 357, doi:10.1038/nature06937, 2008.

Solomon, S., Qin, D., Manning, M., Chen, Z., Marquis, M., Averyt, K., Tignor, M., and Miller, H., eds.: IPCC Fourth Assessment Report: Climate Change 2007 (AR4), chap. Working Group I: The Physical Science Basis, Cambridge University Press, Cambridge, United Kingdom and New York, NY, USA., 2007.

Tans, P.: NOAA/ESRL: Trends in Atmospheric Carbon Dioxide, URL `http://www.esrl.noaa.gov/gmd/ccgg/trends`, 2011.

Tans, P. P., Fung, I. Y., and Takahashi, T.: Observational constraints on the global atmospheric CO_2 budget, Science, 247, 1431–1438, doi:10.1126/science.247.4949.1431, 1990.

Thompson, R. L., Manning, A. C., Gloor, E., Schultz, U., Seifert, T., Hänsel, F., Jordan, A., and Heimann, M.: In-situ measurements of oxygen, carbon monoxide and greenhouse gases from Ochsenkopf tall tower in Germany, Atmospheric Measurement Techniques, 2, 573–591, doi:10.5194/amt-2-573-2009, URL `http://www.atmos-meas-tech.net/2/573/2009/`, 2009.

Winderlich, J., Chen, H., Höfer, A., Gerbig, C., Seifert, T., Kolle, O., Kaiser, C., Lavrič, J. V., and Heimann, M.: Continuous low-maintenance $CO_2/CH_4/H_2O$ measurements at the Zotino Tall Tower Observatory (ZOTTO) in Central Siberia, Atmospheric Measurement Techniques Discussions, 3, 1399–1437, doi:10.5194/amtd-3-1399-2010, URL `http://www.atmos-meas-tech-discuss.net/3/1399/2010/`, 2010.

Wunch, D., Toon, G. C., Wennberg, P. O., Wofsy, S. C., Stephens, B. B., Fischer, M. L., Uchino, O., Abshire, J. B., Bernath, P., Biraud, S. C., Blavier, J.-F. L., Boone, C., Bowman, K. P., Browell, E. V., Campos, T., Connor, B. J., Daube, B. C., Deutscher, N. M., Diao, M., Elkins, J. W., Gerbig, C., Gottlieb, E., Griffith, D. W. T., Hurst, D. F., Jiménez, R., Keppel-Aleks, G., Kort, E. A., Macatangay, R., Machida, T., Matsueda, H., Moore, F., Morino, I., Park, S., Robinson, J., Roehl, C. M., Sawa, Y., Sherlock, V., Sweeney, C., Tanaka, T., and Zondlo, M. A.: Calibration of the Total Carbon Column Observing Network using aircraft profile data, Atmospheric Measurement Techniques, 3, 1351–1362, doi:10.5194/amt-3-1351-2010, URL `http://www.atmos-meas-tech.net/3/1351/2010/`, 2010.

Wunch, D., Toon, G. C., Blavier, J.-F. L., Washenfelder, R., Notholt, J., Con-

nor, B. J., Griffith, D. W. T., Sherlock, V., and Wennberg, P. O.: The Total Carbon Column Observing Network (TCCON), 369, 2087–2112, doi: 10.1098/rsta.2010.0240, 2011.

Yokota, T., Yoshida, Y., Eguchi, N., Ota, Y., Tanaka, T., Watanabe, H., and Maksyutov, S.: Global concentrations of CO_2 and CH_4 retrieved from GOSAT: first preliminary results, 5, 160–163, doi:10.2151/sola.2009-041, 2009.

Chapter 2

A new fully automated FTIR system for total column measurements of greenhouse gases

This Chapter has been published in a shortened form as:

Geibel, M. C., Gerbig, C., and Feist, D. G.

"A new fully automated FTIR system for total column measurements of greenhouse gases", Atmospheric Measurement Techniques, 3, 1363-1375, 2010, www.atmos-meas-tech.net/3/1363/2010/

doi:10.5194/amt-3-1363-2010

2.1 Abstract

This chapter introduces a new fully automated FTIR system that is part of the Total Carbon Column Observing Network. It will provide continuous ground-based measurements of column-averaged volume mixing ratio for CO_2, CH_4 and

several other greenhouse gases in the tropics.

Housed in a 20-foot shipping container it was developed as a transportable system that could be deployed almost anywhere in the world. I describe the automation concept which relies on three autonomous subsystems and their interaction. Crucial components like a sturdy and reliable solar tracker dome are described in detail. The automation software employs a new approach relying on multiple processes, database logging and web-based remote control.

First results of total column measurements at Jena, Germany show that the instrument works well and can provide parts of diurnal as well as seasonal cycle for CO_2. Instrument line shape measurements with an HCl cell suggest that the instrument stays well-aligned over several months.

2.2 Introduction

Surface flux estimations of CO_2 on regional to global scales have so far been derived by a combination of data from a global network of surface sites (GLOBALVIEW-CO2) and the results of global transport models (Gurney et al., 2002; Rayner et al., 1999; Tans et al., 1990). The main advantages of the surface measurements are that they are highly accurate and that they can be obtained with moderate effort even in remote locations. The main disadvantages are that they are strongly influenced by local sources and sinks and that they can only provide measurements from within the atmospheric boundary layer. Despite the high accuracy of the measurements themselves, imperfect representation of vertical mixing near the surface in atmospheric transport models still leads to large uncertainties in modeled tracer mixing ratios (Gerbig et al., 2008).

The existing in situ network can be complemented by precise and accurate total-column-averaged CO_2 volume mixing ratio (VMR) measurements – com-

monly referred to as X_{CO_2}. The column integral of the CO_2 VMR profile is less sensitive to diurnal variations in atmospheric boundary layer height and details of vertical transport in general (Gerbig et al., 2008). It exhibits less spatial and temporal variability than near-surface in situ data, while retaining information about surface fluxes (Gloor et al., 2000). Rayner and O'Brien (2001) have shown that globally distributed X_{CO_2} measurements with an accuracy in the range of $\pm$1.5–2.5 ppmv would be effective in constraining global-scale carbon budgets. However, such X_{CO_2} measurements are still very sparse.

Recent analyses of solar spectra obtained by near-infrared Fourier Transform Spectrometers (FTIR) demonstrate that X_{CO_2} can be retrieved with high precision (Messerschmidt et al., 2010; Washenfelder et al., 2006; Warneke et al., 2005; Dufour et al., 2004; Yang et al., 2002). These measurements make use of characteristic absorption lines that many atmospheric trace gases exhibit in the infrared region of the electromagnetic spectrum. From the difference of the known solar spectrum from space and the measured solar spectrum after passing through the atmosphere, the total column of gases like CO_2, CH_4 and many others can be calculated. To obtain the column-averaged volume mixing ratio, these values have to be divided by the total dry air column. The total dry air column can be derived either from surface pressure or from the measured O_2 total column (for details see Eqns. 2.1–2.3). Unlike surface measurements, the total column measurements provided by ground-based FTIR instruments can also be used directly for the validation of satellite instruments like GOSAT (Yokota et al., 2009).

The Atmospheric Remote Sensing group (ARS) of the Max Planck Institute for Biogeochemistry (MPI-BGC) in Jena, Germany, is currently making the final preparations for installing such an FTIR instrument in the tropics, where such measurements are very sparse. So far the only tropical TCCON site is Darwin, Australia (Deutscher et al., 2010). Other measurements have only been taken dur-

ing short campaigns (Petersen et al., 2010; Warneke et al., 2010). The instrument will be part of the Total Carbon Column Observation Network (TCCON) (Wunch et al., 2011; Toon et al., 2009) that provides ground-truth data for satellite validation. It will be installed on Ascension Island, a British oversea territory in the South Atlantic. This unique location should provide excellent observation conditions for the FTIR instrument. Due to its small size and very scarce vegetation, the influence from local sources and sinks on the CO_2 and CH_4 measurements should be minimal.

The instrument has been set up and tested at the MPI-BGC in Jena, Germany. This article provides a technical overview of the system and shows first results obtained during this initial phase.

2.3 The MPI-BGC FTIR system

Most existing FTIR systems were usually built for one special location and designed to cope with that location's typical special environmental conditions. Several of those systems are automated or can at least be controlled remotely through a data connection. Exceeding these capabilities, the main goal of the MPI-BGC's FTIR project was to build an instrument that could be deployed nearly anywhere in the world (Fig. 2.1). It should be easily transportable by truck, train or ship. In addition to that, two persons should be able to set it up at a new location within one week. After setup, no manpower should be required during regular operation for at least six months.

However, building such a system is challenging. In a remote region with little infrastructure to rely on such an instrument has to be able to run fully automatic without operator intervention for months or even years. This challenge added several problems that had to be solved in addition to setting up the instrument itself.

All components had to be designed or modified to minimize the risk of technical failures or software errors. Wherever possible, key devices were simplified to avoid problems arising from unnecessary complexity. Essential devices were set up redundantly to provide essential functions even in the case of a failure.

The components have been chosen on the basis of reliability, stability and maintainability. All of them are grouped into three autonomous modules - each of them designed to perform special tasks in the system as reliably as possible in the most simple way. These modules are the weather station, the Programmable Logic Controller (PLC) and the Master PC. A star-shaped automation concept where all components are controlled by a single master system would also have created a potential single point of failure. Therefore the three autonomous modules were set up so that they are able to check each other's performance or even reset each other in the case of a failure. Detailed information can be found in sections 2.3.4 and 2.3.5.

Figure 2.1: Picture of the MPI-BGC FTIR container at its preliminary location close to the MPI-BGC in Jena.

The components have been chosen on the basis of reliability, stability and

maintainability. All of them are grouped into three autonomous modules - each of them designed to perform special tasks in the system as reliably as possible in the most simple way. These modules are the weather station, the Programmable Logic Controller (PLC) and the Master PC. A star-shaped automation concept where all components are controlled by a single master system would also have created a potential single point of failure. Therefore the three autonomous modules were set up so that they are able to check each other's performance or even reset each other in the case of a failure. Detailed information can be found in sections 2.3.4 and 2.3.5.

2.3.1 The container

One of the main targets was to create a system that is relatively easy to transport. Therefore, the system is housed in a custom-made 20-foot shipping container made by CHS CONTAINER GmbH Bremen, Germany (see Fig. 2.1 & 2.2). It is equipped with enhanced insulation and has a fully integrated air conditioning system consisting of a Stulz CCU 81A (STULZ GmbH, Germany), a Guentner S-GVV047C/CW heat exchanger (Guenther Kaelte-Klima GmbH, Germany) and in addition a Remko EFT 240 dehumidifier (REMKO GmbH & Co. KG; Germany). This provides stable indoor operating conditions at outdoor temperatures from -40 °C to +40 °C.

The container is fully certified for land as well as ship transport and can be transported like any standard freight container. This offers high flexibility at reasonable shipping prizes. Besides stable inside environmental conditions, stable electric power is essential for operation. The system requires 3-phase AC with 400 V / 32 A / 50 Hz and has an average power consumption of 1-3 kW (site-dependent, max. peak 10 kW). An uninterruptible power supply (UPS, MGE UPS Comet EX RT, 7 kVA) is integrated to bridge power failures of up to two

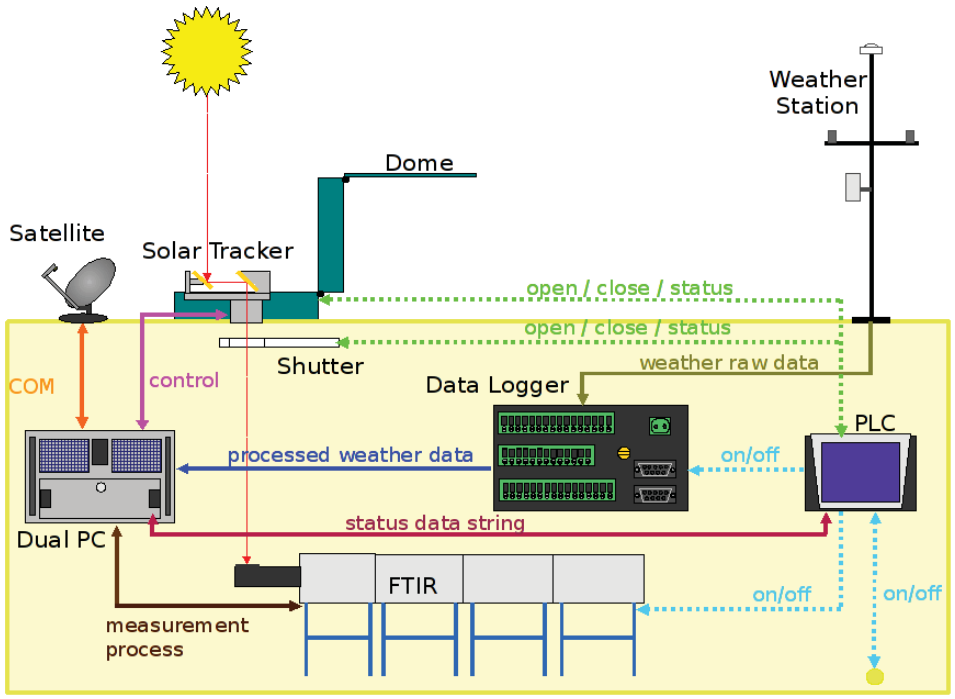

Figure 2.2: Schematic overview of the MPI-BGC FTIR system. It illustrates all major parts of the system. The communication flow between the individual components is indicated by arrows.

hours. The focus transportability continues with the components: Nearly all items inside of the container are integrated in transport-ready state. All items mounted on the roof have their defined transport location inside the container. All of the roof-mounted items are constructed in a way that they can be lifted just with the help of a pulley (see Fig. 2.1). No additional utilities like cranes are needed.

2.3.2 Fourier Transform Infrared Spectrometer (FTIR)

The atmospheric measurements are performed by a Bruker 125HR FTIR instrument. The instrument provides high resolution solar absorption spectra over a large spectral range. The resolution of the instrument is 0.0035 $\mathbf{cm^{-1}}$ and it covers a bandwidth from 3800 $\mathbf{cm^{-1}}$ to 15800 $\mathbf{cm^{-1}}$ with the current detectors. Similar to the Park Falls instrument (Washenfelder et al., 2006) it is equipped with two detectors measuring simultaneously in different spectral ranges. A silicon diode detector covers the spectral range from 9000 $\mathbf{cm^{-1}}$ to 15800 $\mathbf{cm^{-1}}$. An Indium-Gallium-Arsenide (InGaAs) detector. covers the spectral range from 3800 $\mathbf{cm^{-1}}$ to 12000 $\mathbf{cm^{-1}}$. The components of the spectrometer can be seen in Fig. 2.3.

To enhance the stability of the system and avoid spectral contamination by water vapor, all measurements are performed under vacuum. Therefore the system is equipped with a multi-stage oil-free scroll pump (Varian TriSrcoll300). To avoid vibrations of the pump influencing the measurements, the pump only runs during night time.

For accurate measurements the monitoring of the instrumental line shape is necessary. This is realized as described by Hase et al. (1999) by integrating an HCl gas cell (length 10 $\mathbf{cm}$, diameter 4 $\mathbf{cm}$, filling pressure 5.013 $\mathbf{mbar}$) in the beam path inside the FTIR instrument. It is located directly in front of the 1st aperture. First results of this procedure are described section 2.4.1.

The atmospheric measurements are performed with the same settings that were

used by Messerschmidt et al. (2010): a 0.014 $\mathbf{cm^{-1}}$ resolution (corresponds to an optical path difference of 65 $\mathbf{cm}$) with an aperture of 1 $\mathbf{mm}$ diameter and a scanner velocity of 10 $\mathbf{kHz}$. The electronic low pass filter is set to 10 $\mathbf{kHz}$ (corresponds to 15798 $\mathbf{cm^{-1}}$). The high folding limit for the Fourier transformation to 15798 $\mathbf{cm^{-1}}$. Two individual scans, one forward and one backward, are made per measurement.

2.3.3 Solar Tracker and protective devices

Remote sensing of greenhouse gases via FTIR uses the sun as a light source. The container has an open flange in the roof. Mounted on top of this is a Bruker Solar Tracker type A547 (see Fig. 2.4). It is controlled by its own PC (see 2.3.4) and follows the sun and guides the sunlight into the container. The flange and the tracker have to be protected from bad weather such as rain, snow and high wind speed. Therefore a special dome was developed.

The Solar Tracker dome

The dome for the solar tracker is a crucial part of the system. It has to meet several demands. In the closed state it should be small but still allow the tracker to move into every position. It has to protect the tracker and the flange beneath from rain, snow and hail as well as strong winds and flying debris. In the open state it should allow the tracker an unobstructed 360° view. The mechanism has to be simple and reliable.

The are already several solutions for several types of solar tracker. For the Bruker A547, the most common solution is the ROBODOME (Washenfelder et al., 2006). This however has several disadvantages. It is relatively big and heavy and also proved to be not very reliable. Based on the experiences of other members of TCCON with that dome, the decision was made to develop a new

Figure 2.3: Illustration of the Bruker IFS125HR spectrometer and its components. The HCl cell was removed when the pictures where taken.

Figure 2.4: The Bruker Solar Tracker type A547 mounted in the custom made dome (shown in open state).

dome.

This solution to the given demands consists of a frame of aluminum x-profile beams that are covered with aluminum plates. Its z-shaped movement (see Fig. 2.5) is realized by two arrays of hinges and a moving lever. This lever is powered by a gear motor via a tooth-belt drive.

The middle part (Part B in Fig. 2.5) was constructed as an open frame. Therefore the area exposed to the wind does not increase during the opening or closing process. This way, even high wind speeds do not inhibit the movement of the dome. This ensures that it can be closed under all conditions. Also note that the upper part of the lid always faces upwards. This way the tracker cannot be harmed by water, dirt or other objects (leafs etc.) that may have collected in the open lid when the dome is closed. More detailed information (such as pictures, part list, dimensional drawings, etc.) can be found in Appendix A.

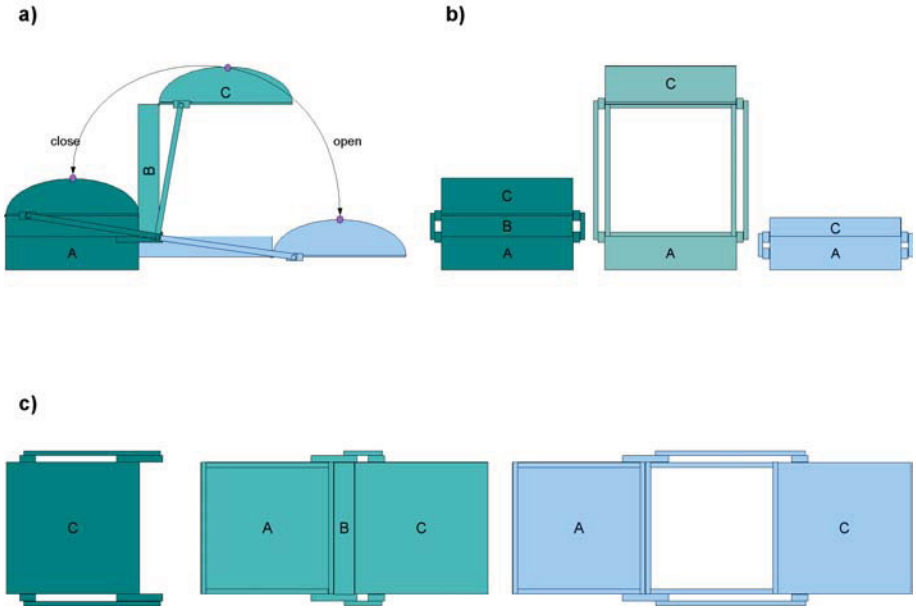

Figure 2.5: Schematic overview of the BGC-FTIR Solar Tracker Dome in side (a), front (b) and top view (c). It consists of a frame of aluminum x-profile beams that are covered with aluminum plates. Its z-shaped movement is realized by two arrays of hinges and a moving lever. The middle part (Part B) is an open frame. The upper part (Part C) of the lid always faces upwards.

The Shutter

A failure of the dome mechanism cannot be ruled out completely. Therefore, an additional shutter was constructed as a backup mechanism to close the container even in case the dome should fail. The shutter also provides additional thermal insulation between the container and the dome. This saves energy and avoids condensation problems when the dome is closed.

The shutter basically works like a drawer and is mounted on the ceiling directly underneath the flange (Fig. 2.2). Usually it is opened and closed simultaneously with the dome but can be operated independently if necessary. The main part is a polyamide block with a hole on one and a drain on the other side. It slides via four ball bearings on two polished steel rails. The shutter is moved by a spindle-motor and the accurate positioning is realized with two limit switches. In the open position, the hole in the shutter is congruent with the hole in the flange. This way the sun light can travel from the tracker down into the spectrometer.

When the shutter is closed, the drain slides under the hole in the flange and seals the container. In case of a dome failure, rain is collected by the drain and guided into a reservoir. More detailed information can be found in Appendix B.

2.3.4 Hardware components for automation

For the automation the system was divided in three autonomous modules. Each of these modules is designed to be as reliable as possible. In case of a malfunction or a complete failure of a component, the modules bring the system to a defined standby or sleeping state. The design goal was that any failure of a single component would not leave the system in an undefined state.

Table 2.1: Weather station equipment

Sensor	Position	Type
Temperature/Humidity	2 outdoor	Galltec+Mela C2.4
Temperature /Humidity	2 indoor	Campbell CS215
Temperature	2 in the FTIR	Campbell T107
Global radiation	1 outdoor	Kipp&Zonen Pyranometer CMP3
Precipitation	2 outdoor	Lambrecht Electronic 15153 & 15152
Wind speed	2 outdoor	Lambrecht Wind Sensor Industrial 14557
Ambient pressure	2 outdoor	Vaisala PTB210

Weather station

The weather station (Fig. 2.6) is equipped with a number of different sensors to monitor outdoor and indoor conditions (Table 2.1). Most of the sensors are redundant since their data are either crucial for the measurement process or for the protection of the system against bad weather.

Indoor as well as outdoor temperature and humidity are measured by redundant pairs of sensors. A pyranometer measures global radiation which is useful to determine appropriate measurement conditions without opening the dome. Wind speed is measured by two cup anemometers that were chosen for their reliability. Precipitation is detected by two different approaches: The first sensor works with a light barrier that can detect rain, hail and also other flying objects like insects. The second precipitation sensor detects changes in conductivity when it is hit by rain or snow. This one is also able to detect fine spray.

Highly accurate and stable pressure measurements are essential for the quality of the retrieved mixing ratio profiles (see Eq. 2.2). However, long-term drift of these sensors is a problem that cannot be avoided easily. To be able to detect and

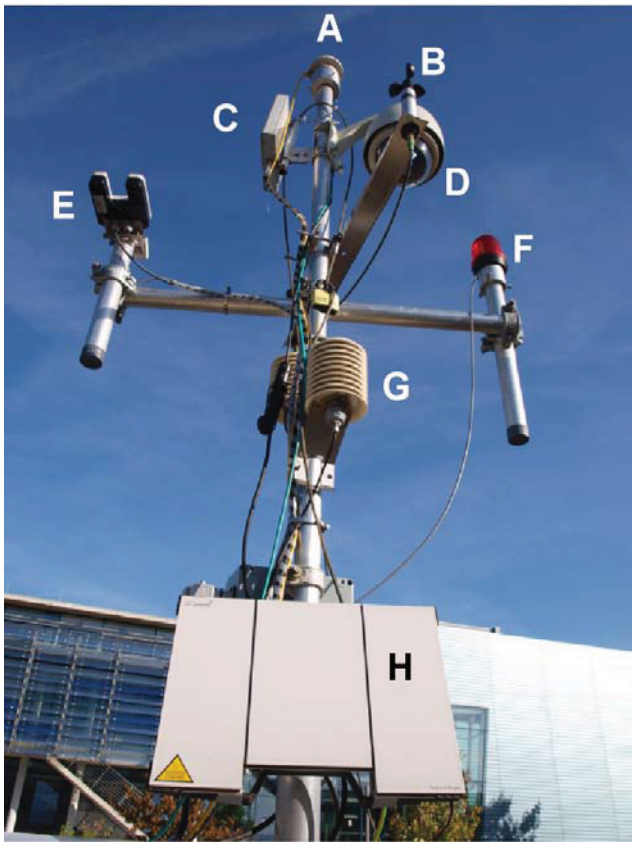

Figure 2.6: The weather station mounted on top of the FTIR container. It measures temperature and humidity with two sensors (G). Wind speed is measured by two cup anemometers (B). It is also equipped with two different precipitation detectors (E). On the very top, global radiation is measured by a pyranometer (A). The pole of the weather station also hosts two antennas for communication: a wireless LAN link (B) and a BGAN satellite receiver (H). Also an outdoor camera (D) and a signal LED (F) are mounted on the pole.

correct such a drift three highly accurate digital Vaisala PTB210 pressure sensors and a special recalibration scheme where chosen.

Figure 2.7 explains how this recalibration scheme works: Sensors 1 and 2 are used for redundant measurements while sensor number 3 is a calibrated spare. At a regular maintenance visit sensor 3 will replace one of the two used sensors (sensor 1 in this example). Sensor 1 will then be re-calibrated and later replace the other sensor – in this example sensor 2 – during the next maintenance visit. This leap-frog calibration scheme allows to detect and compensate any drift of the sensors. One sensor always stays in the system as a reference. This way, a detected drift in one of the sensors can be corrected and discontinuities in the pressure measurements can be avoided. With this scheme, one should be able to maintain the original ± 0.1 **hPa** accuracy of the sensors over a period of many years.

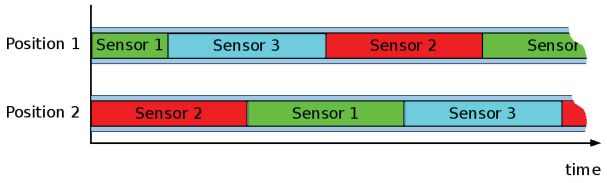

Figure 2.7: Pressure sensor recalibration scheme. Sensors 1 and 2 are used for redundant measurements while sensor number 3 is a calibrated spare that replaces one of the two used sensors (e.g. sensor 1) at the next maintenance after approximately 6 months. Sensor 1 will then be re-calibrated and later replace sensor 2.

The precipitation sensors are directly connected to the PLC (see section 2.3.4) to ensure that dome and shutter can be closed as quickly as possible when it starts to rain. All other sensors are connected to a Campbell Scientific CR 1000 data

logger. This data logger processes the raw data and makes them available to the Master PC via an Ethernet connection (Fig. 2.8). Details of the weather station can be found in (Zöphel, 2008).

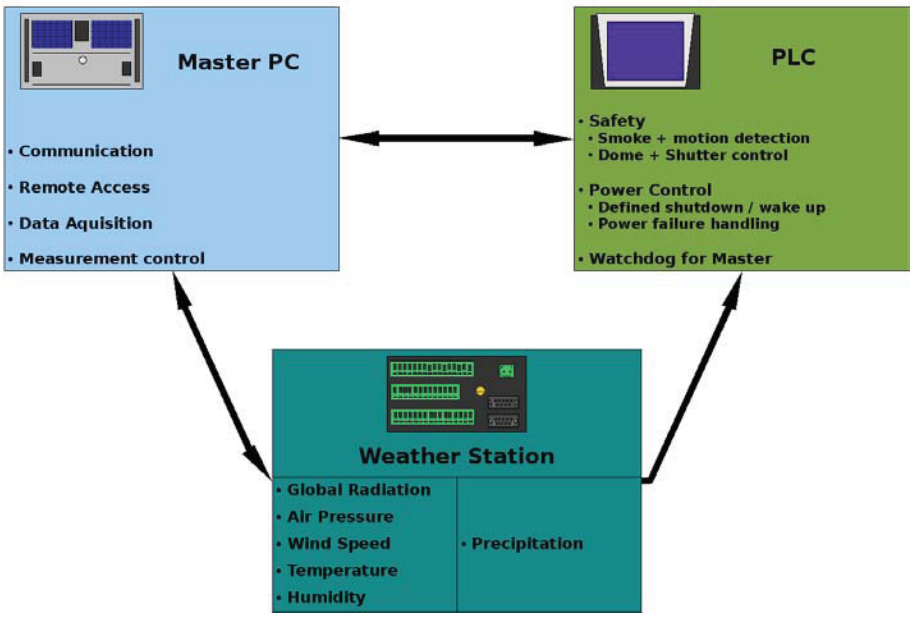

Figure 2.8: Schematic overview of the communication. The three major parts of the FTIR system are autonomous systems. They communicate over a serial and an Ethernet connection, respectively.

Programmable Logic Controller (PLC)

The Programmable Logic Controller (PLC, Unitronics Vision570-57-T40B) is the backbone of the container and one of the most crucial components. Its main target is to bring the container into one of several predefined states depending on external circumstances. It also indicates this status to the Master PC and executes its requests to change this status (Fig. 2.8). The PLC has full control of the dome and the shutter and controls the power lines of most other components (including the Master PC). The PLC is also connected to different sensors and switches

to determinate the status of many components. The communication to the Master PC is established via an RS232 connection. If the Master PC should fail to communicate with the PLC for too long, the PLC will try to restart the Master PC.

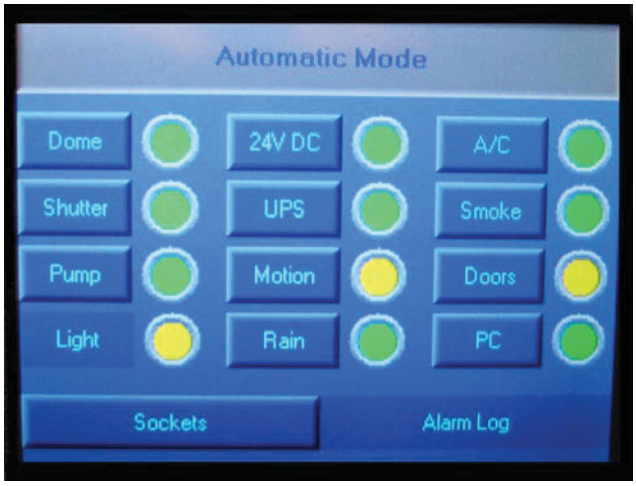

Figure 2.9: PLC control panel showing the PLC operating in automatic mode. It shows the actual container status, the colored bullets indicate status of each component - whereas green stands for “OK“, yellow for “in progress“ and red indicates ”alert“. Detailed information can be accessed via the sub menus

The PLC has two operational modes that can be chosen via a selector switch. The automatic mode shows the actual container status on the PLC’s main screen (Fig. 2.9). Colored bullets indicate the status of each component: green stands for “OK“, yellow for “in progress“ and red indicates ”alert“. More detailed information can be accessed via sub menus. In this mode the PLC accepts commands only via RS232 communication.

Every input command is answered by the PLC with a detailed list of the actual status of every input and output channel. Invalid commands are ignored. The status of the PLC is logged in the database on the Master PC and can so also be monitored by a remote user. In case of an emergency a direct command input

with via Ethernet is possible. That way also commands of the Master PC can be overruled.

The other operation mode - the manual mode - is for manual operation during maintenance. In this mode all parts of the PLC system can be accessed and operated manually through their sub menus. External commands from the Master PC are ignored in this mode.

In case of a power failure the PLC ensures that all components are properly shut down and the dome is closed before the UPS battery runs out. It is also the first system that automatically restarts after such a shutdown. All the other components are afterwards restarted in a defined cascade until the whole system is fully operational again. More detailed information can be found in Appendix C.2.

Dual PC

For high availability, the container is equipped with an industrial 19-inch rack-mount computer system (ARBOR Technology Corp. IEC-620). The chassis includes two redundant power supplies, temperature monitoring, and a temperature controlled fan cascade. It hosts two independent Slot-CPUs in the same case (Table 2.2): one for the measurement process, communication and data storage (Master PC) and one for the control of the solar tracker (Tracker PC). Passively cooled low-energy CPUs were chosen to avoid a system malfunction due to a fan failure.

Master PC The Master PC is responsible for the communication, data storage and the automation of the whole system (see Section 2.3.5). It runs a Debian Linux system that can be fully controlled remotely, even over low bandwidth links. For the other components, the Master PC also provides network-related services like routing, name service or email handling. Through the network time

Table 2.2: Dual PC components

Component	Master PC	Tracker PC
Mainboard	PCA-6004H-00A2E Advantec	PCA-6002VE-00B1E Advantec
CPU	VIA C3 800MHz	Intel Celeron Tualatin 400MHz
RAM	1024MB	128MB
Additional Cards	SCSI, Serial	Bruker Solar Tracker Controller Card
Diskspace	Infotrend EonStor SCSI RAID ES U12U-G4020M2 12x72GB	1GB SSD Compact Flash
Storage	HP StorageWorks DAT 72x10 10x auto loader	

protocol (NTP), it also provides accurate time information from a GPS receiver to the internal network.

To the PLC and the Tracker PC, the Master PC is connected via an RS-232 serial line. All other components like the spectrometer, the UPS, the weather station data logger, internal and external cameras are accessed over the internal network (Fig. 2.8).

Data is stored on a high-availability RAID system with redundant power supplies. In the current configuration it hosts twelve SCSI hard disks of 72 GB each. The total usable disk space in the current configuration is 280 GB with four redundant disks and four spare disks. The maximum configurable redundant disk space would be 792 GB with no spares. Disk configurations can be changed –

even remotely – while the system is operating.

In addition to the disk, data can also be stored on a tape drive (HP StorageWorks DAT 72x10 auto loader). It has a maximum capacity of ten DDS-5 tapes with an uncompressed capacity of 36 GB each. The tapes were chosen for their small form factor which makes it easy to send them by post.

Tracker PC For improved reliability, the Tracker PC is a fan-less and diskless system that needs only low performance. Data is stored on a flash memory card. The operating system is a minimal Debian Linux which emulates a FreeDOS environment for the original solar tracker software. This way, the solar tracker software can be controlled over the network and the clock can be synchronized through NTP.

2.3.5 Automation concept

Communication, data storage and transfer

The container can be accessed remotely in two ways. First, it has a wireless link that can cover up to 2 km to the next available internet access. It also is equipped with an Inmarsat BGAN satellite receiver (Thrane & Thrane Explorer 700) that provides a high-speed internet connection almost anywhere in the world. However, the transfer of large amounts of data over the satellite link is very expensive, so this link is intended mostly for remote control.

If there is no alternative internet connection, data can also be saved to DDS-5 (DAT) tapes with an uncompressed capacity of 36-GB. The tape drive can hold up to ten tapes. Due to their small form factor and weight, these tapes can be mailed easily.

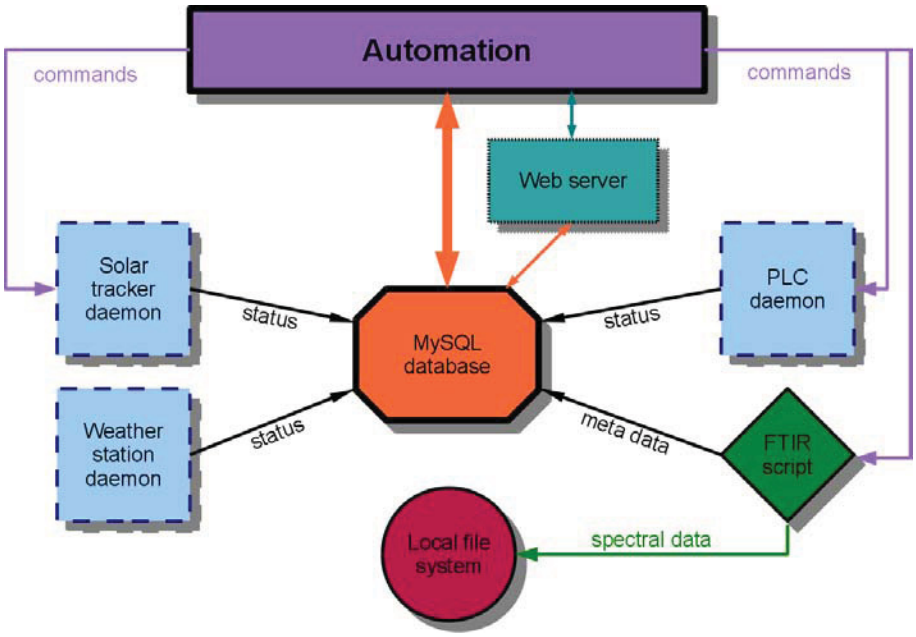

Figure 2.10: Schematic overview of the automation software components.

Software

The concept for the automation software, which is displayed in Fig. 2.10, reflects the modular design of the hardware components. Each main hardware module (PLC, solar tracker, weather station) has an independent background process – a so-called daemon – that handles communication with the respective module. The daemons are started at system boot and are restarted automatically if they should exit prematurely.

Each daemon communicates continuously with its hardware module. The daemons log status information or data from the weather station at regular intervals. The PLC and the solar tracker daemon can also receive commands through a TCP/IP socket. These commands are then forwarded to the PLC or solar tracker, for example to open or close the solar tracker dome or change the solar tracker operation mode.

All status information is logged in a central MySQL database. A database approach was chosen over file-based logging because it is safer and offers much more flexibility. For example, the MySQL server makes sure that data can be read and written simultaneously by several processes. It is also easy to search for data or retrieve it in a different format then the one it was written. Mirroring the whole database to another MySQL server over the internet is also straightforward.

The automation module is also a daemon. It uses a list of rules to translate the detailed log information from the database into more abstract system states. For example, one system state is that the system is sleeping during the night or that it is ready to start a measurement. Important: the rules themselves are not part of the program. Instead, they are also defined in the database and can be changed any time. There is no need to change the software if the automation rules have to be adapted.

Measurements are started by the automation daemon whenever all necessary pre-conditions have been met. The FTIR measurement script runs once and exits after the measurement. While it runs, it logs its actions to the database. The spectral data is saved in files on the local file system.

The whole system is controlled by daemon processes that do not provide a user interface. To monitor the activity of the FTIR container remotely, a web server displays the information from the database in a user-friendly way. Through the web interface, it is also possible to change the automation rules or control other parts of the FTIR container.

2.4 First results

2.4.1 Alignment

For the accurate retrieval of total column values, a good alignment of the FTIR is crucial. The instrument line shape (ILS) and the modulation efficiency are retrieved from HCl cell measurements is a useful indicator of the FTIR's alignment (Hase et al., 1999). The ILS is the response function of the instrument to a single spectral peak of negligible width ($\tilde{\nu}_0$). The modulation efficiency is the ratio of modulated radiation to total radiation and illustrates the quality of the interference of the wavefronts in the spectrometer. The performed measurements were analyzed with the Linefit spectrum fitting algorithm (Hase, 2010).

Figures 2.11 and 2.12 show the results of an ILS retrieval from HCl cell measurements from August 2009 and February 2010. The modulation efficiency decreased slightly during these six months (see Fig. 2.12). Nevertheless, the maximum loss in modulation efficiency is 3%. For comparison other well aligned TCCON instruments reach values for modulation efficiency of better then 95%. The phase error for both measurements is well below 0.01 rad which Hase et al. (1999) considered as a good value.

Figure 2.11 illustrates the symmetry of the ILS. The top plot shows both ILS measurements plotted over the difference of the wavenumber $\tilde{\nu}$ and the center peak wavenumber $\tilde{\nu}_0$ (Griffiths and de Haseth, 1986). The lower plot shows the difference of the positive part ($\tilde{\nu} > \tilde{\nu}_0$) and the negative part ($\tilde{\nu} < \tilde{\nu}_0$) as a measure of symmetry. The observed deviations from symmetry are very small as one should expect from a well-aligned FTIR.

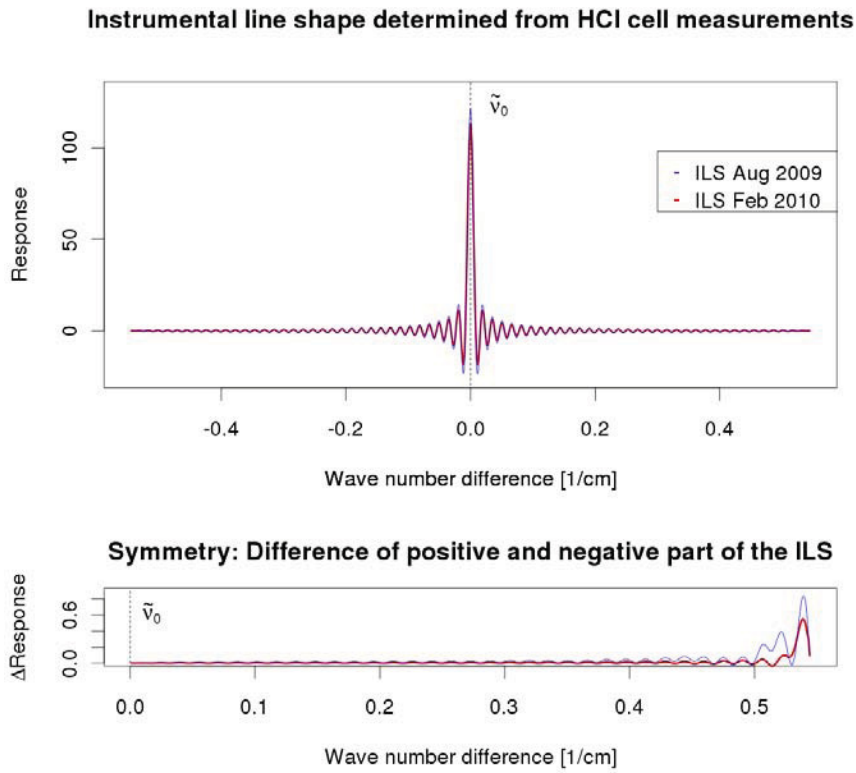

Figure 2.11: Comparison of the instrument line shape of the Jena BRUKER IFS125HR in August 2009 and February 2010. The x-axis represents the wavenumber difference relative to $\tilde{\nu}_0$. Both measurements show a symmetric ILS. For better visualization of the symmetry the lower part of this Figure shows the difference of the positive and negative part of the ILS.

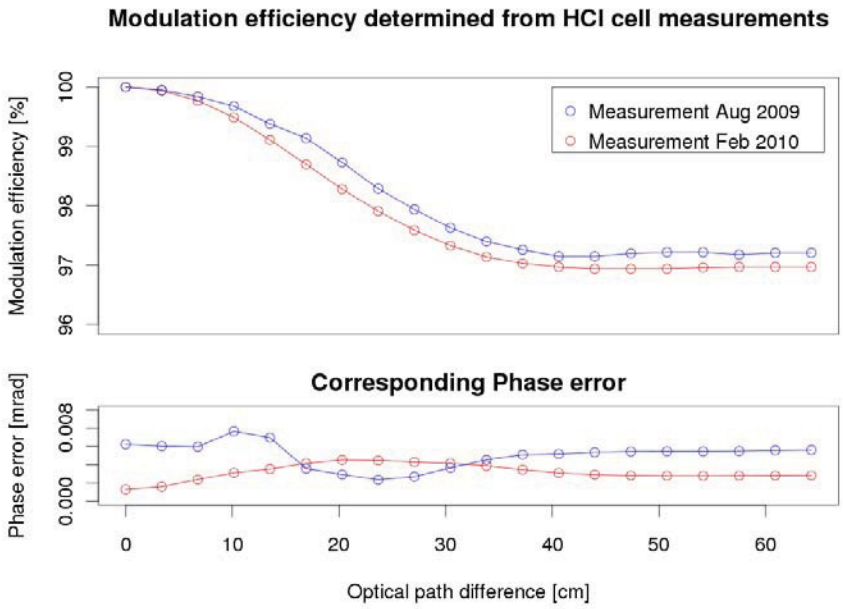

Figure 2.12: Changes in the modulation efficiency and phase error of the Jena BRUKER IFS125HR from August 2009 to February 2010.

2.4.2 Column measurements at Jena

In 2009 measurements were taken during the setup of the instrument and the automation of the system. Due to the ongoing construction, the time series is relatively sparse. The site is located at the outskirts of Jena, Germany, at 50.910°N, 11.569°E, 211 $\mathbf{m}$ above sea level.

The acquired data was processed with TCCON standard analysis software GGG (Wunch et al., 2011). GGG is a suite of software tools developed at Jet Propulsion Laboratory (JPL) to determine the abundances of atmospheric trace gases from infrared solar absorption spectra. This software evolved from the ODS software (Norton and Rinsland, 1991) used for the Version 2 analysis of ATMOS data, but has incorporated many improvements since then. The most complex program in the GGG suite is GFIT, the spectral fitting code. GFIT has been used for the analysis of MkIV spectra (balloon, aircraft, and ground-based), plus the Version 3 analysis of ATMOS shuttle spectra (Irion et al., 2002). Also GFIT has been used for the analysis of spectra from several ground-based FTIR spectrometers (Notholt et al., 1997). In recent years GFIT and has become the standard data analysis tool for TCCON. The number of species retrieved from GFIT and the associated number of analyzed micro windows after TCCON specifications can be found in Table 2.3. An overview of the retrieved species from the measurements in Jena can be found in Figure 2.13.

As described in Wunch et al. (2011), CO_2 is retrieved in the 6220 $\mathbf{cm^{-1}}$ and 6339 $\mathbf{cm^{-1}}$ micro windows, O_2 in the 7885 $\mathbf{cm^{-1}}$ micro window, CH_4 in the 5938 $\mathbf{cm^{-1}}$, 6002 $\mathbf{cm^{-1}}$ and 6076 $\mathbf{cm^{-1}}$ micro windows and CO in the 4233 $\mathbf{cm^{-1}}$ and 4290 $\mathbf{cm^{-1}}$ micro windows. The dry air column-averaged mole fractions are calculated from the gas columns (Γ), according to

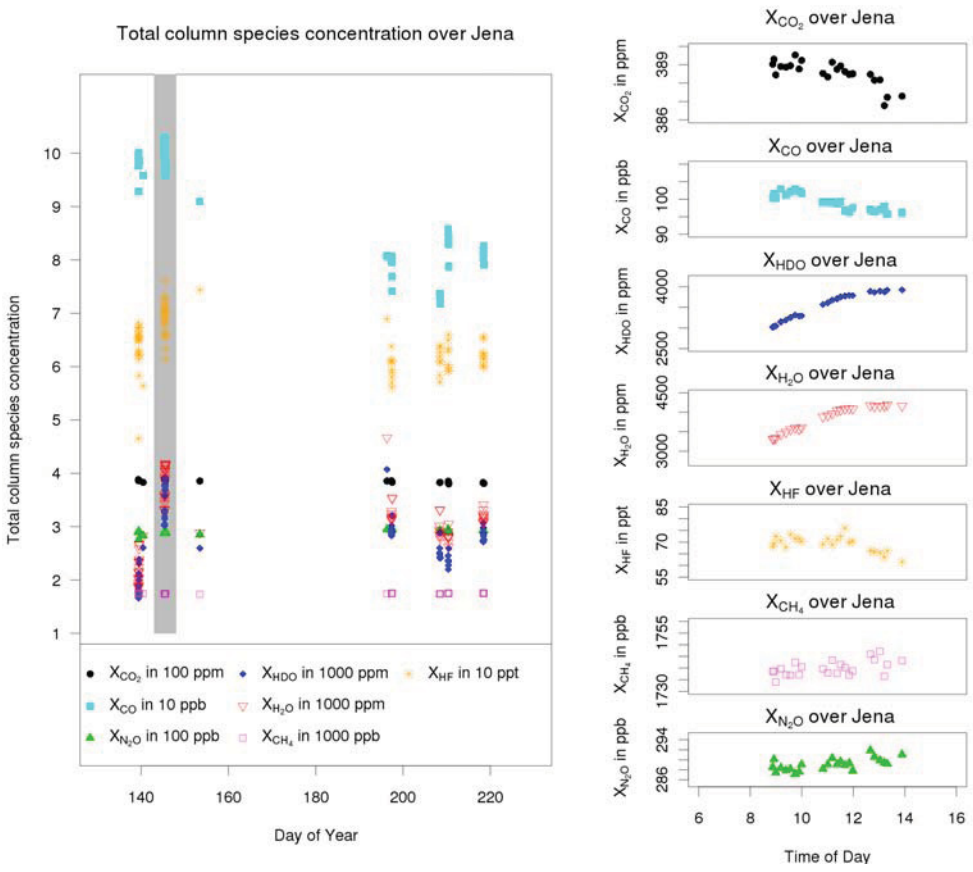

Figure 2.13: Standard TCCON analysis of measurements taken with Jena FTS 2009. The right column of plots show the diurnal variation of the species for the marked day in the left plot.

Table 2.3: Table of species retrieved from GFIT and the associated number of analyzed micro windows according to TCCON specifications

Species	Micro Windows	Standard output
CH_4	3	yes
CO	2	yes
CO_2	2	yes
HF	1	yes
HCl	16	no
HDO	4	yes
H_2O	9	yes
N_2O	2	yes
O_2	1	no

$$f_{\mathrm{CO_2,\,avg}} = \frac{\Gamma_{\mathrm{CO_2}}}{\Gamma_{\mathrm{dry\ air}}} \tag{2.1}$$

As shown by Washenfelder et al. (2006), there are two methods for calculating the total dry column $\Gamma_{\mathrm{dry\ air}}$. Both methods have specific advantages and disadvantages:

$$\Gamma_{\mathrm{dry\ air,\,P}} = \frac{P_S}{m_{\mathrm{air}} g} - \Gamma_{\mathrm{H_2O}} \tag{2.2}$$

with m_{air} - air mass, P_S - surface pressure, g - gravity constant

$$\Gamma_{\mathrm{dry\ air,O_2}} = \frac{\Gamma_{\mathrm{O_2}}}{0.2095} \tag{2.3}$$

In general the approach of calculating the total dry column via surface pressure with Eq. (2.2) is more precise since P_S can be measured very accurately (see Section 2.3.4). Using the more noisy retrievals of the O_2 column for the calculation

in Eq. (2.3) will increase the random scatter. However, non-perfect measurement conditions (like pointing errors and variation of intensity during the measurement) and systematic errors will affect the O_2 and CO_2 retrievals in a similar way. Those are reduced to a minimum when $\Gamma_{\text{dry air},O_2}$ is used in Eq. (2.1) .

Due to ongoing construction and limited field of view, I were not able to cover full diurnal cycles. Nevertheless, the measured diurnal variation of total column X_{CO_2} over Jena (Fig. 2.14) illustrates the decrease in atmospheric X_{CO_2} over the covered period in more detail. It shows also that the decrease of X_{CO_2} over the day is relatively constant.

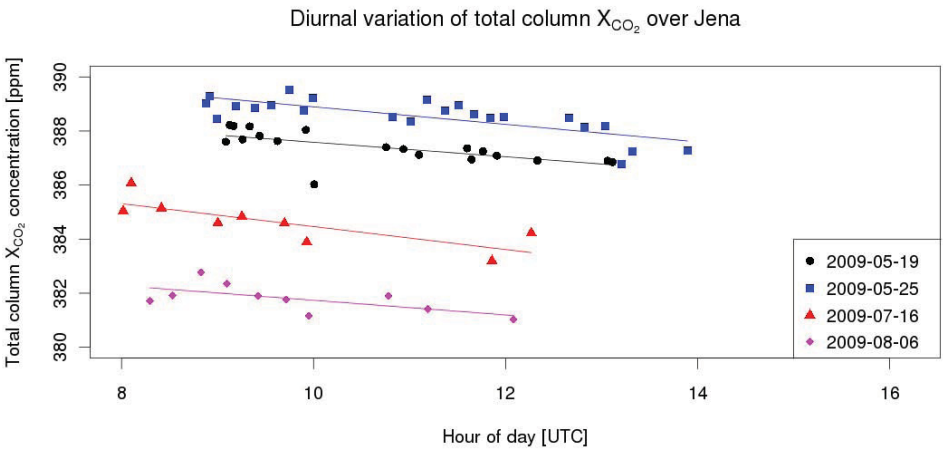

Figure 2.14: Diurnal variation of total column X_{CO_2} over Jena shown on selected days. The decrease of X_{CO_2} over the day was relatively constant

An important feature of total column measurements is that – compared to surface measurements – they are less affected by variability induced by vertical transport and local sources and sinks. That is in fact one of the main reasons why total column measurements can complement the existing in-situ network (Rayner and O'Brien, 2001).

This insensitivity of the total column can be found in high-resolution model

simulations. I analyzed WRF-VPRM model data (Pillai et al., 2010) from 2006 for the Jena area. Figure 2.15 shows a nocturnal build-up of CO_2 in the lower levels that decreases with height. As the vertical mixing starts in the morning this build-up quickly dissolves. The figure also shows that the sensitivity of the calculated total column X_{CO_2} to the boundary layer effects are very small.

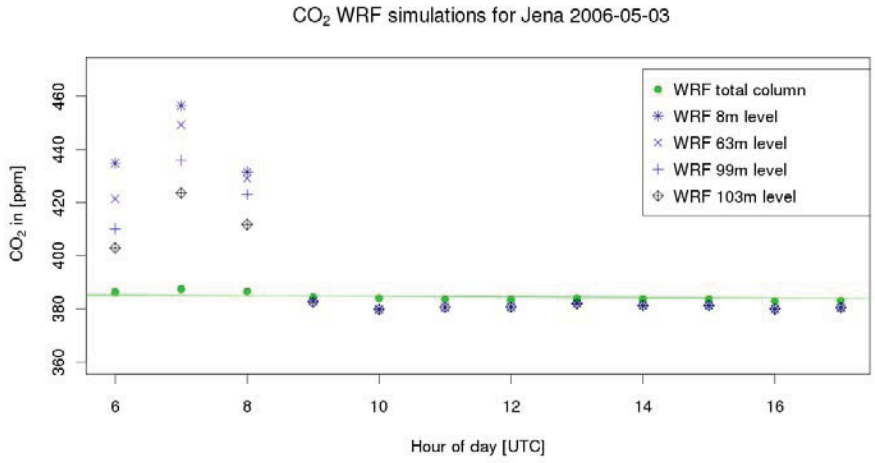

Figure 2.15: Diurnal variation of CO_2 from WRF-VPRM for total column and lower levels over Jena. The model resolution is 2 $\mathbf{km}$.

Expecting similar results from measurements, I compared the total column X_{CO_2} data measured with the Jena FTIR to ground-based in-situ CO_2 measured on the roof the MPI for Biogeochemistry. The in-situ measurements are performed with non-dispersive infrared (NDIR) gas analyzer type LI-COR LI-6262. As expected from the model analysis, the diurnal variation of X_{CO_2} next to the ground seems not to effect the column measurements (Fig. 2.16). The large drop of more than 80 ppm in boundary layer CO_2 was not represented in the total column measurements. This illustrates the small contribution of the boundary layer to the total column and confirms the expectations from the model data. The FTIR measurements after 10am show a relative constant offset compared to the in-situ measure-

ments.

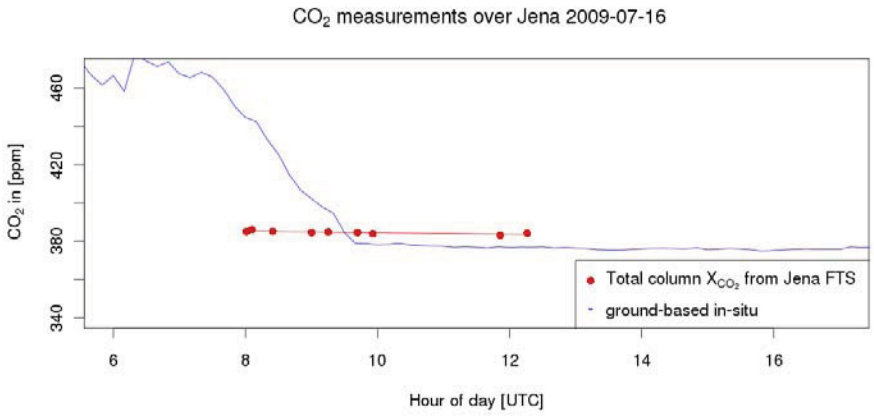

Figure 2.16: Diurnal variation of ground-based in-situ CO_2 and total column X_{CO_2} over Jena. The gaps in the time series are due to clouds.

Fig. 2.17 shows the comparison total column X_{CO_2} daily averages vs. total column values calculated from TM3 inversions (Rödenbeck, 2005). Unfortunately, TM3 result were only available until the end of 2007. To compare them with the FTIR results, the TM3 results were extrapolated to 2009. For this extrapolation, the yearly cycles of 1996 till 2007 were averaged and scaled to the 2007 mean. This reduced the synoptic variability. The mean yearly cycle was then shifted for the annual mean CO_2 growth rate for the years 2008 (1.80 ppm) and 2009 (1.64 ppm) (Tans, 2011) by adding an offset of +3.44 $\mathbf{ppm}$. The red empty boxes represent X_{CO_2} measured by the FTIR. respectively the daily mean (for day where more then one measurement could be performed). The vertical red lines represent the standard error of the mean value. The FTIR total column X_{CO_2} values represent the prognosed yearly cycle of 2009 well and are within respectively close to the 1σ threshold.

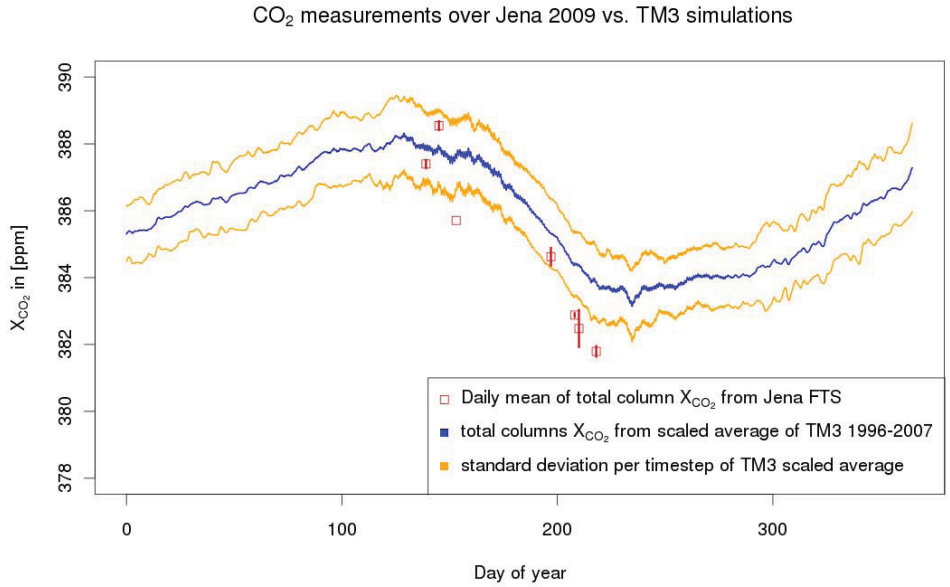

Figure 2.17: Total column X_{CO_2} measurements over Jena vs. extrapolated TM3 results for 2009. Empty red boxes represent individual X_{CO_2} measurements from the FTIR. Red boxes with vertical lines represent daily mean values of X_{CO_2} with error bars (vertical lines).

2.5 Conclusions and outlook

This article describes the principal components and the design concept of the MPI-BGC FTIR system. The main design goals were reliability and low maintenance effort for operation at remote sites. This was realized through the interaction of independent subsystems that were kept as simple as possible. Critical components are redundant as much as possible.

The instrumental line shape of the FTIR was determined from HCl cell measurements. During a period of six months this ILS changed only slightly. From these results one can expect that – once aligned – the instrument will be very stable over long time periods.

During the installation phase at Jena, Germany, the instrument measured column-averaged X_{CO_2}, X_{CO} and X_{CH_4}. Compared to ground-based in-situ CO_2 VMR measurements, the FTIR total column X_{CO_2} showed an expected offset in the morning which mostly disappeared with the breakup of the nighttime planetary boundary layer. This effect demonstrated the reduced sensitivity of X_{CO_2} measurements to mixing processes in the planetary boundary layer and confirms results of model simulations. Otherwise, the X_{CO_2} measurements show a distinct diurnal cycle. A part of seasonal cycle measured over Jena during the installation phase corresponded to TM3 simulation results that were extrapolated to 2009 values.

In September/October 2009 the MPI-BGC FTIR system and five other European FTIR stations took part in the IMECC aircraft campaign. The goal of this campaign was to determine a calibration factor between total column values calculated from in-situ aircraft profiles of CO_2, CH_4, and CO and corresponding total column values retrieved from ground-based FTIR. The results from this campaign will be published separately in the near future.

The FTIR will first take part in a test campaign to Wollongong, Australia, from June to October 2010. This campaign will provide a rare opportunity of a side-

by-side intercomparison of two TCCON-type FTIR instruments on the southern hemisphere.

After the campaign, the instrument will be shipped to Ascension Island (7.93° S, 14.37° W) to commence long-term measurements. From this unique location it will provide the first long time series of X_{CO_2}, X_{CH_4} and other column-averaged greenhouse gases in the tropical western hemisphere.

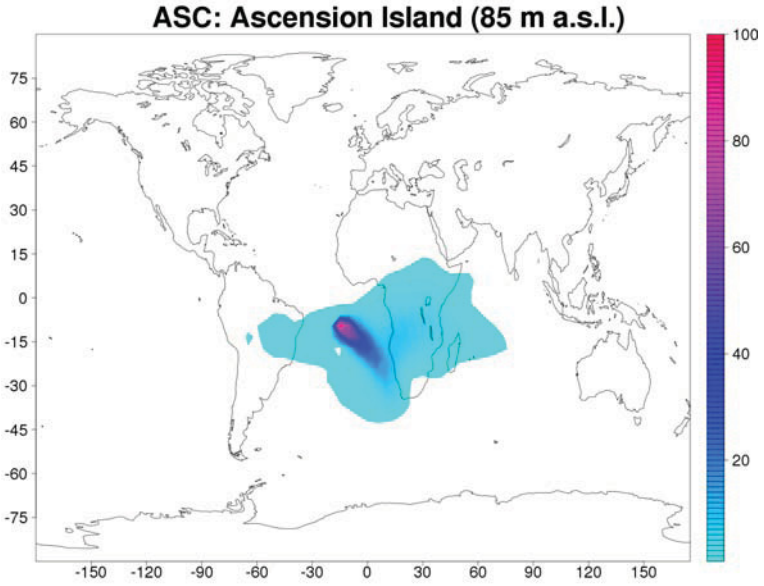

Figure 2.18: Footprint analysis for a total-column instrument on Ascension Island. The colored values represent the relative contribution to the total column for different surface regions in arbitrary units that have been normalized to 100 at the peak value. The footprint was produced using the TM3 adjoint by Rödenbeck (2005) at a horizontal resolution of $5° \times 3.75°$ (fine grid). Individual runs for each month of 2006 were integrated to provide this full-year footprint.

Ascension Island was selected because it frequently receives air masses from the rain forest regions of Africa and occasionally also from South America. Figure 2.18 shows a one-year footprint for the total column measurements expected

from Ascension Island. Due to the small size of the island, it would also provide a rare opportunity to validate sun-glint measurements by satellites. A long-term time series of flask measurements from Ascension Island already exists and other groups will provide valuable continuous in-situ surface measurements of CO_2 and CH_4 in the near future.

Bibliography

Deutscher, N. M., Griffith, D. W. T., Bryant, G. W., Wennberg, P. O., Toon, G. C., Washenfelder, R. A., Keppel-Aleks, G., Wunch, D., Yavin, Y., Allen, N. T., Blavier, J.-F., Jiménez, R., Daube, B. C., Bright, A. V., Matross, D. M., Wofsy, S. C., and Park, S.: Total column CO_2 measurements at Darwin, Australia - site description and calibration against in situ aircraft profiles, 3, 947–958, doi: 10.5194/amt-3-947-2010, URL http://www.atmos-meas-tech.net/3/947/2010/, 2010.

Dufour, E., Bréon, F.-M., and Peylin, P.: CO_2 column averaged mixing ratio from inversion of ground-based solar spectra, J. Geophys. Res., 109, D09 304, doi: 10.1029/2003JD004469, 2004.

Gerbig, C., Körner, S., and Lin, J. C.: Vertical mixing in atmospheric tracer transport models: error characterization and propagation, Atmos. Chem. Phys., 8, 591–602, doi:10.5194/acp-8-591-2008, 2008.

GLOBALVIEW-CO2: Cooperative Atmospheric Data Integration Project - Carbon Dioxide. CD-ROM, NOAA ESRL, Boulder, Colorado, URL ftp://ftp.cmdl.noaa.gov/ccg/co2/GLOBALVIEW, 2009.

Gloor, M., Fan, S.-M., Pacala, S., and Sarmiento, J.: Optimal sampling of the

atmosphere for purpose of inverse modeling: A model study, Global Biogeochem. Cycles, 14, 407–428, doi:10.1029/1999GB900052, 2000.

Griffiths, P. R. and de Haseth, J. A.: Fourier Transform Infrared Spectrometry, Wiley-Interschience, 1986.

Gurney, K. R., Rachel M. Law, A. S. D., Rayner, P. J., Baker, D., Bousquet, P., Bruhwiler, L., Chen, Y.-H., Ciais, P., Fan, S., Fung, I. Y., Gloor, M., Heimann, M., Higuchi, K., John, J., Maki, T., Maksyutov, S., Masarie, K., Peylin, P., Prather, M., Pak, B. C., Randerson, J., Sarmiento, J., Taguchi, S., Takahashi, T., and Yuen, C.-W.: Towards robust regional estimates of CO_2 sources and sinks using atmospheric transport models, Nature, 415, 626–630, doi:10.1038/415626a, 2002.

Hase, F.: Linefit spectrum fitting algorithm, URL `http://www-imk.fzk.de/asf/ftir/linefit.htm`, 2010.

Hase, F., Blumenstock, T., and Paton-Walsh, C.: Analysis of the instrumental line shape of high-resolution Fourier Transform IR spectrometers with gas cell measurements and new retrieval software, Appl. Opt., 38, 3417–3422, doi:10.1364/AO.38.003417, 1999.

Irion, F. W., Gunson, M. R., Toon, G. C., Chang, A. Y., Eldering, A., Mahieu, E., Manney, G. L., Michelsen, H. A., Moyer, E. J., Newchurch, M. J., Osterman, G. B., Rinsland, C. P., Salawitch, R. J., Sen, B., Yung, Y. L., and Zander, R.: Atmospheric Trace Molecule Spectroscopy (ATMOS) Experiment Version 3 data retrievals, Appl. Opt., 41, 6968–6979, doi:10.1364/AO.41.006968, 2002.

Messerschmidt, J., Macatangay, R., Notholt, J., Petri, C., Warneke, T., and Weinzierl, C.: Side by side measurements of CO2 by ground-based Fourier transform spectrometry (FTS), doi:10.1111/j.1600-0889.2010.00491.x, 2010.

Norton, R. H. and Rinsland, C. P.: ATMOS data processing and science analysis methods, Appl. Opt., 30, 389–400, doi:10.1364/AO.30.000389, 1991.

Notholt, J., Toon, G., Stordal, F., Solberg, S., Schmidbauer, N., Becker, E., Meier, A., and Sen, B.: Seasonal variations of atmospheric trace gases in the high Arctic at 79°N, J. Geophys. Res., 102, 12,855–12,861, doi:10.1029/97JD00337, 1997.

Petersen, A. K., Warneke, T., Frankenberg, C., Bergamaschi, P., Gerbig, C., Notholt, J., Buchwitz, M., Schneising, O., and Schrems, O.: First ground-based FTIR-observations of methane in the tropics, Atmos. Chem. Phys., 10, 2303–2320, doi:10.5194/acpd-10-2303-2010, URL http://www.atmos-chem-phys-discuss.net/10/2303/2010/, 2010.

Pillai, D., Gerbig, C., Marshall, J., Ahmadov, R., Kretschmer, R., Koch, T., and Karstens, U.: High resolution modeling of CO_2 over Europe: implications for representation errors of satellite retrievals, Atmos. Chem. Phys., 10, 83–94, doi:10.5194/acp-10-83-2010, URL http://www.atmos-chem-phys.net/10/83/2010/, 2010.

Rayner, P. J. and O'Brien, D. M.: The utility of remotely sensed CO_2 concentration data in surface source inversions, Geophys. Res. Lett., 28, 175–178, doi:10.1029/2000GL011912, 2001.

Rayner, P. J., Enting, I. G., Francey, R. J., and Langenfelds, R.: Reconstructing the recent carbon cycle from atmospheric CO_2, $\delta^{13}C$ and O_2/N_2 observations, Tellus, 51B, 213–232, doi:10.1034/j.1600-0889.1999.t01-1-00008.x, 1999.

Rödenbeck, C.: Estimating CO_2 sources and sinks from atmospheric mixing ratio measurements using a global inversion of atmospheric transport, Tech. Rep. 6, Max Planck Institute for Biogeochemistry, Jena, Germany, URL

http://www.bgc-jena.mpg.de/mpg/websiteBiogeochemie/Publikationen/Technical_Reports/tech_report6.pdf, 2005.

Tans, P.: NOAA/ESRL: Trends in Atmospheric Carbon Dioxide, URL http://www.esrl.noaa.gov/gmd/ccgg/trends, 2011.

Tans, P. P., Fung, I. Y., and Takahashi, T.: Observational constraints on the global atmospheric CO_2 budget, Science, 247, 1431–1438, doi:10.1126/science.247.4949.1431, 1990.

Toon, G., Blavier, J.-F., Washenfelder, R., Wunch, D., Keppel-Aleks, G., Wennberg, P., Connor, B., Sherlock, V., Griffith, D., Deutscher, N., and Notholt, J.: Total Column Carbon Observing Network (TCCON), in: Fourier Transform Spectroscopy, OSA Technical Digest (CD), p. paper JMA3, Optical Society of America, Vancouver, Canada, URL http://www.opticsinfobase.org/abstract.cfm?uri=FTS-2009-JMA3, 2009.

Warneke, T., Yang, Z., Olsen, S., Körner, S., Notholt, J., Toon, G. C., Velazco, V., Schulz, A., and Schrems, O.: Seasonal and latitudinal variations of column averaged volume-mixing ratios of atmospheric CO_2, Geophys. Res. Lett., 32, L03 808, doi:10.1029/2004GL021597, 2005.

Warneke, T., Petersen, A. K., Gerbig, C., Jordan, A., Rödenbeck, C., Rothe, M., Macatangay, R., Notholt, J., and Schrems, O.: Co-located column and in situ measurements of CO_2 in the tropics compared with model simulations, Atmos. Chem. Phys., 10, 5593–5599, doi:10.5194/acp-10-5593-2010, URL http://www.atmos-chem-phys.net/10/5593/2010/, 2010.

Washenfelder, R. A., Toon, G. C., Blavier, J.-F., Yang, Z., Allen, N. T., Wennberg, P. O., Vay, S. A., Matross, D. M., and Daube, B. C.: Carbon dioxide column

abundances at the Wisconsin Tall Tower site, J. Geophys. Res., 111, D22 305, doi:10.1029/2006JD007154, 2006.

Wunch, D., Toon, G. C., Blavier, J.-F. L., Washenfelder, R., Notholt, J., Connor, B. J., Griffith, D. W. T., Sherlock, V., and Wennberg, P. O.: The Total Carbon Column Observing Network (TCCON), 369, 2087–2112, doi: 10.1098/rsta.2010.0240, 2011.

Yang, Z., Toon, G. C., Margolis, J. S., and Wennberg, P. O.: Atmospheric CO_2 retrieved from ground-based IR solar spectra, Geophys. Res. Lett., 29, 1339, doi:10.1029/2001GL014537, 2002.

Yokota, T., Yoshida, Y., Eguchi, N., Ota, Y., Tanaka, T., Watanabe, H., and Maksyutov, S.: Global concentrations of CO_2 and CH_4 retrieved from GOSAT: first preliminary results, 5, 160–163, doi:10.2151/sola.2009-041, 2009.

Zöphel, H.: Test and installation of an automatic weather station to provide ground-based FTIR measurements for TCCON, Master's thesis, University of Applied Sciences, Jena, Germany, URL `http://www.bgc-jena.mpg.de/bgc-systems/pmwiki2/uploads/PhdAmpDiplomaThesis/zoephel.pdf`, 2008.

Chapter 3

The IMECC Aircraft Calibration Campaign

3.1 Abstract

This section presents the results for CH_4 of the first European aircraft campaign for the calibration of six TCCON stations. During this campaign aircraft in-situ profiles of CO_2, CH_4, H_2O, CO, N_2O, H_2, SF_6 were taken in form of spirals close to the FTS stations. The aircraft data have a vertical coverage ranging from approx. 300 to 13000 $\mathbf{m}$, or 80 $\%$ of the total atmospheric column seen by the FTS. For the calibration of total column FTS measurements the aircraft profiles were extended with GFIT a-priori profiles and surface in-situ data to aircraft columns. The FTS data were pre-processed with the IPP software to correct for solar intensity variations (SIV). The pre-processed data were analyzed with GFIT using three versions of spectral line lists.

The resulting calibration factor for CH_4 of the IMECC campaign agree with the prior results of Wunch et al. (2010), however the uncertainty could be reduced by 50$\%$. A sensitivity study shows, that the calibration factor is sensitive to the

vertical coverage of the aircraft profile used for calibration.

3.2 Introduction

The Jena FTIR system will be part of the Total Carbon Column Observation Network (TCCON) (Wunch et al., 2011). TCCON is a worldwide network of ground-based FTS systems of currently 18 stations that provides a source for calibration and validation of satellite measurements. It is also a supplement to the existing worldwide in-situ network by creating a link between the in-situ and satellite measurements like those performed with SCIAMACHY or GOSAT. However, different measurement techniques do not necessarily produce equal measurement values - even when they are measuring exactly the same physical quantity. So the integration of the FTIR measurements into the existing ground-based in-situ network requires a calibration. Wunch et al. (2010) pointed out that it is highly likely that there is a species-specific uniform calibration factor for all FTIR systems of TCCON.

The goal of the IMECC aircraft campaign was to verify these results and to calibrate six of the European TCCON stations.

3.3 The IMECC campaign

Within the European infrastructure project IMECC the first airborne campaign to calibrate FTS sites in Europe was organized. The Max Planck Institute for Biogeochemistry (MPI-BGC) was responsible for the organization of the flight tracks, the equipment of the aircraft and the post-flight analysis of the aircraft in-situ data. The main purpose of the campaign was the calibration of TCCON-Europe sites. TCCON-Europe comprises currently six FTS sites, whereof two

sites are equipped with on-site tall tower measurements. Figure 3.1 shows the six TCCON-Europe, the airbase in Hohn and the flight tracks of the IMECC campaign.

Figure 3.1: FTS locations and aircraft flight tracks of the IMECC campaign

The campaign took place between the 28^{th} of September and 9^{th} October 2009. The aircraft used was a Learjet 35A, operated by Enviscope/GfD, with a maximum flight altitude of 13 $\mathbf{km}$. High altitude in-situ profiles were taken near the TCCON-Europe stations from 300 $\mathbf{m}$ up to 13000 $\mathbf{m}$ in spirals (see Fig. 3.2). During the transfer flights from the airbase additional dips were made. Overall eight flights in four days were realized. In about 20 flight hours 16 vertical profiles over the TCCON-Europe sites were sampled at different solar zenith angles (SZA). The details of the overflights are listed in Table 3.1 and the acquired aircraft data are presented in Section 3.3.3. A more detailed overview of the aircraft profiles for all overflights can be found in Appendix D.

The FTS sites were operated at the time of the campaign by the individual working groups who are responsible for each site. Three stations are operated by

Table 3.1: The stations of the IMECC campaign and their overflight dates.

ID	Location	Latitude	Longitude	Overflights [UTC]	Code
BI	Bialystok,	53.23°N	23.03°E	**2009-30-09**	
	Poland			09:39	Bialystok OF1a
				10:04	Bialystok OF1b
				13:48	Bialystok OF2a
				14:10	Bialystok OF2b
OR	Orleans,	47.97°N	2.13°E	**2009-10-02**	
	France			06:36	Orleans OF1a
				07:02	Orleans OF1b
				10:35	Orleans OF2a
				10:57	Orleans OF2b
KA	Karlsruhe	49.08°N	8.43°E	**2009-10-02**	
	Germany			09:31	Karlsruhe OF1a
GM	Garmisch-	47.48°N	11.06°E	**2009-10-05**	
	Partenkirchen,			08:47	Garmisch OF1a
	Germany				
JE	Jena,	50.91°N	11.57°E	**2009-10-05**	
	Germany			07:56	Jena OF1a
				08:08	Jena OF1b
				2009-10-09	
				10:12	Jena OF2a
				10:35	Jena OF2b
BR	Bremen,	53.10°N	8.85°E	**2009-10-05**	
	Germany			08:47	Bremen OF1a
				2009-10-09	
				11:05	Bremen OF2a

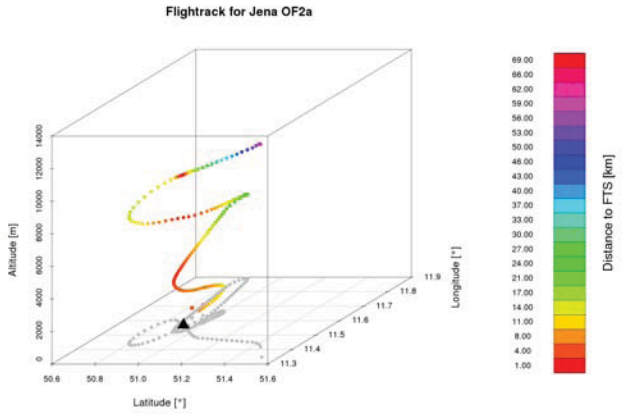

Figure 3.2: A aircraft typical profile with spiral close to the FTS location. This figure shows overflight Jena OF2a. The black triangle symbols the location of the FTS. The colors of the dots symbolize the distance of the aircraft to the FTS, the grey dots are a projection of the flight path on the ground.

the Institute of Environmental Physics (IUP), Bremen, Germany, one station by IMK-ASF, Karlsruhe Institute of Technology (KIT), Karlsruhe, Germany, one by IMK-IFU (KIT), Garmisch-Partenkirchen, Germany and one by the Max Planck Institute for Biogeochemistry (MPI-BGC), Jena, Germany. All TCCON-Europe FTS instruments are FTS 125HR spectrometers from Bruker and are equipped according to TCCON standards. Only the Karlsruhe FTS has a limited bandwidth for the Indium Gallium Arsenide (InGaAS) detector. The settings used during the campaign are listed in Table 3.2. In the following section the different stations are described in detail.

3.3.1 Calibrated TCCON-Europe sites

This paragraph (Sec. 3.3.1) is published in a similar form in Messerschmidt, Geibel et al. (2011).

Table 3.2: Settings for the FTS measurements during the IMECC-campaign.

Parameter	**JE**	**BR, BI & OR**	**GM**	**KA**^{D}
resolution [$\mathbf{cm^{-1}}$]*	0.014	0.014	0.02	0.014
aperture	1.0**	1.0***	1.0***	0.8
scanner vel. [$\mathbf{kHz}$]	10	10	7.5	20
high pass filter [$\mathbf{cm^{-1}}$]	open	open	open	open
low pass filter [$\mathbf{cm^{-1}}$]	15798	15798	15798	15798
optical filter [$\mathbf{mm}$] Si diode	none	dichroite	dichroite	none
scans [$\mathbf{No.}$]	1**** (FW/BW)	1 (FW/BW)	1 (FW/BW)	6-8
HCl cell	yes	yes	yes	no

With *: $resolution = \frac{0.9}{OPDmax}$, **: reduced beam diameter for InGaAs detector via additional aperture, ***: intensity reductor at the InGaAs detector, ****: Due to technical difficulties only forward scan on the first overflight day, ^{D}: Karlsruhe InGaAs lower limit of 5490 $\mathbf{cm^{-1}}$ (TCCON standard 3800 $\mathbf{cm^{-1}}$).

The FTS facility in Bialystok, Poland

The FTS facility in Bialystok (53°N, 23°E) is operated by the IUP, Bremen, Germany in close cooperation with AeroMeteoService, Bialystok, Poland. Bialystok lies in the far east of Europe and represents the easternmost measurement station within Europe. An on-site tall tower (300 $\mathbf{m}$) allows to compare the FTS measurements with in-situ measurements. Bialystok is one of the two sites in Europe (besides the site in Orleans, France), which have on-site tall tower measurements. Additional regular low aircraft profiling are operated on a weekly basis, covering the lowest 3 $\mathbf{km}$. The FTS instrument is in operation since March 2009 and since then part of the TCCON. The FTS in Bialystok is fully automated, measurement tasks can be filed via remote access. For the time of the campaign a scientist from the IUP, Germany and a colleague of the partner company AeroMeteoService were on site to ensure the functionality of the FTS system and the on-site in-situ instruments.

The FTS facility in Bremen, Germany

At Bremen (53°N, 9°E) FTS measurements have been started in 2000. Since 2004 the site is part of the networks NDACC and TCCON. While some European FTS observatories are located on high mountains, the FTS system at Bremen is located on flat terrain. The low altitude location is advantageous for studying tropospheric gases. In addition, the flat surroundings at the site in Bremen makes this site well suited for the validation of satellites. Due to its location, measurements are possibly affected by emissions from nearfield sources. During the campaign the FTS in Bremen was operated through scientists of the remote sensing working group at the IUP.

The FTS facility in Garmisch-Partenkirchen, Germany

The FTS site Garmisch (47°N, 11°E) is operated by IMK-IFU/KIT (Garmisch-Partenkirchen, Germany). Measurements started in 2004 and are part of TCCON since 2007. The site is located at 734 m a.s.l. within the so-called "flash plain" extending to the north toward Munich. The Garmisch TCCON-FTS is operated coincident to the NDACC mountain-site FTS at Zugspitze (2964 m a.s.l.). The Garmisch site is also close to the Hohenpeissenberg site of the German weather service (about 30 $\mathbf{km}$ to the north) performing in-situ measurements of CO_2 and CH_4. Around this location IMK-IFU/KIT runs also the "TERENO preAlpine" regional station network, which is the largest ecosystem observation center in Europe.

The FTS facility in Jena, Germany

The FTS instrument in Jena (51°N, 11°E) was set up and operated by the Atmospheric Remote Sensing group at the Max Planck Institute for Biogeochemistry, Jena, Germany (Geibel et al., 2010). The long-term destination within the TCCON network is Ascension Island in the South Atlantic Ocean. Presumably from 2011 on it will start providing tropical measurements for TCCON. Details of this system can be found in Section 2.

During the time of the IMECC campaign the instrument was still being set up at Jena. Since the automation software was not yet completed, the instrument had to be operated manually during the overflights. After the campaign the FTS system was shipped to Australia, for an intercomparison campaign with the FTS at the University of Wollongong (see Section 4).

The FTS facility in Karlsruhe, Germany

The FTS instrument in Karlsruhe (49°N, 8°E) is operational since September 2009, just before the IMECC campaign. Like Bremen, measurements are possibly affected by emissions from nearfield sources due to the FTS location. During the IMECC campaign the FTS in Karlsruhe was operated by the ground-based FTS group at IMK-ASF/KIT, Karlsruhe.

The FTS facility in Orleans, France

The FTS facility in Orleans (47°N, 2°E) is operated by the IUP, Bremen, Germany in close cooperation with the LSCE, Paris, France. The measurement site has the advantage of an on-site tall-tower (180 $\mathbf{m}$) like the site in Bialystok, Poland. Low altitude profiles are sampled with a rental aircraft on a regular basis. The measurements within the TCCON started directly after installation in August 2009. The FTS in Orleans is fully automated, measurement tasks can be filed via remote access. At the campaign a scientist from the IUP, Germany and a colleague of LSCE were on site to ensure that the FTS and the on-site in-situ instruments were working properly.

3.3.2 Aircraft instrumentation

For continuous measurements of CO_2, CH_4 and H_2O, the aircraft was equipped with a Wavelength-Scanned Cavity Ring Down Spectrometer (CRDS) (model G1301-m, Piccaro Inc., Sunnyvale, CA), providing mixing ratio data at a frequency of 0.5 $\mathbf{Hz}$. The analyzer was calibrated against WMO reference gases in the laboratory before and after the airborne campaign, providing an accuracy of 0.1 $\mathbf{ppm}$ and 2 $\mathbf{ppb}$ for CO_2 and CH_4, respectively. Measurements were made without drying of the air, and dry air mixing ratios were derived following Chen

et al. (2010).

CO data were measured with an Aerolaser AL5002, which was calibrated during flight using WMO traceable standards. The instrument provides dry air mixing ratios at 1 $\mathbf{Hz}$ with an accuracy of 2 $\mathbf{ppb}$ (Gerbig et al., 1999). In addition to the in-situ data, up to eight flasks were taken at different altitude levels per profile. These flasks were analyzed for CO_2 and its isotopes, CH_4, N_2O, CO, H_2 and SF_6. The results were used to assure the quality of the continuous measurements. The flasks were analyzed post-flight at the gas analysis lab of the Max Planck Institute for Biogeochemistry, Jena. Supplemental meteorological data were recorded. Air temperature was recorded with a Rosemount 102AH2AF Total Temperature Sensor, for pressure measurements a Setra 270 (static pressure) and a Setra 239 (dynamic pressure) were used. Relative humidity was measured by a HUMICAP H Sensor.

3.3.3 Aircraft data

During the whole campaign in-situ data of CO_2, CH_4, H_2O, CO, N_2O, H_2, SF_6 were taken on board the aircraft. Figures 3.3 and 3.4 present an overview of the aircrafts location, in-situ data for CO_2, CH_4, CO and H_2O as well as temperature and relative humidity. The the overall distance flown during the IMECC campaign is approximately 12000 $\mathbf{km}$.

These figures show lower values for CO around Bialystok and Orleans (see left part of Figures 3.3 and 3.4) than the values measured at the other stations. The FTS stations at Bialystok and Orleans are located in rural environments. The mixing ratios should be less affected by local CO emission sources. The other FTS stations are all situated in densely populated areas. This should result in generally higher CO values.

The aircraft data were obtained at different times of the day and under dif-

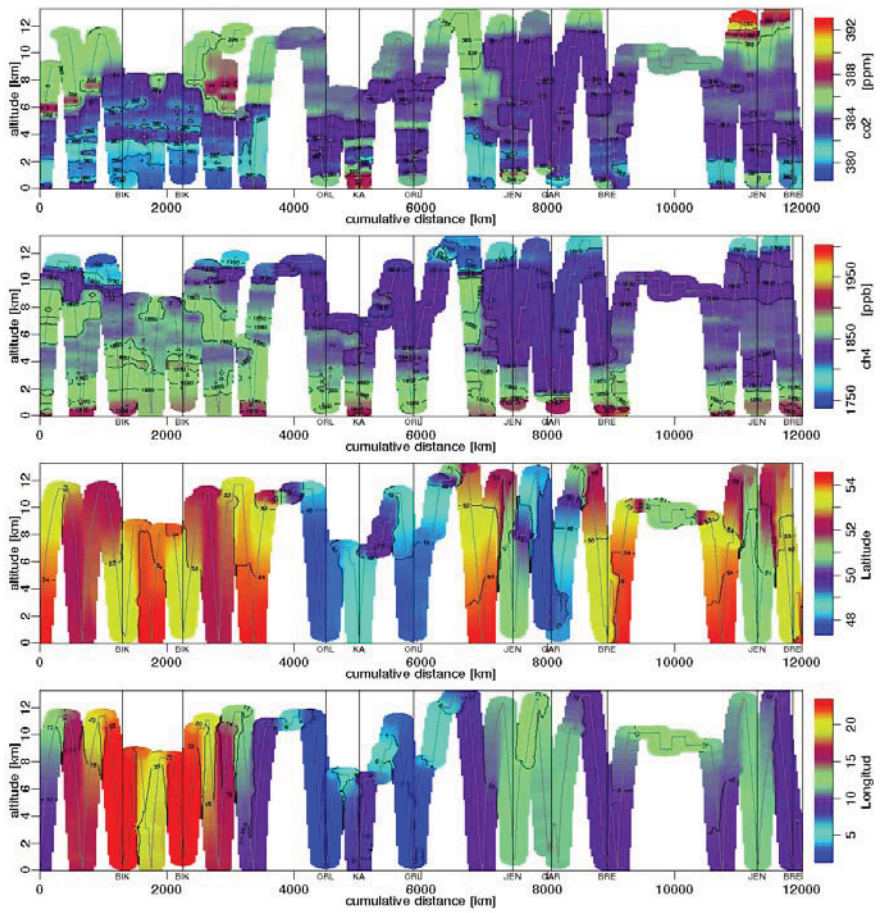

Figure 3.3: Cross sections of aircraft in-situ data over total flight track for CO_2, CH_4 and location (Latitude / Longitude).

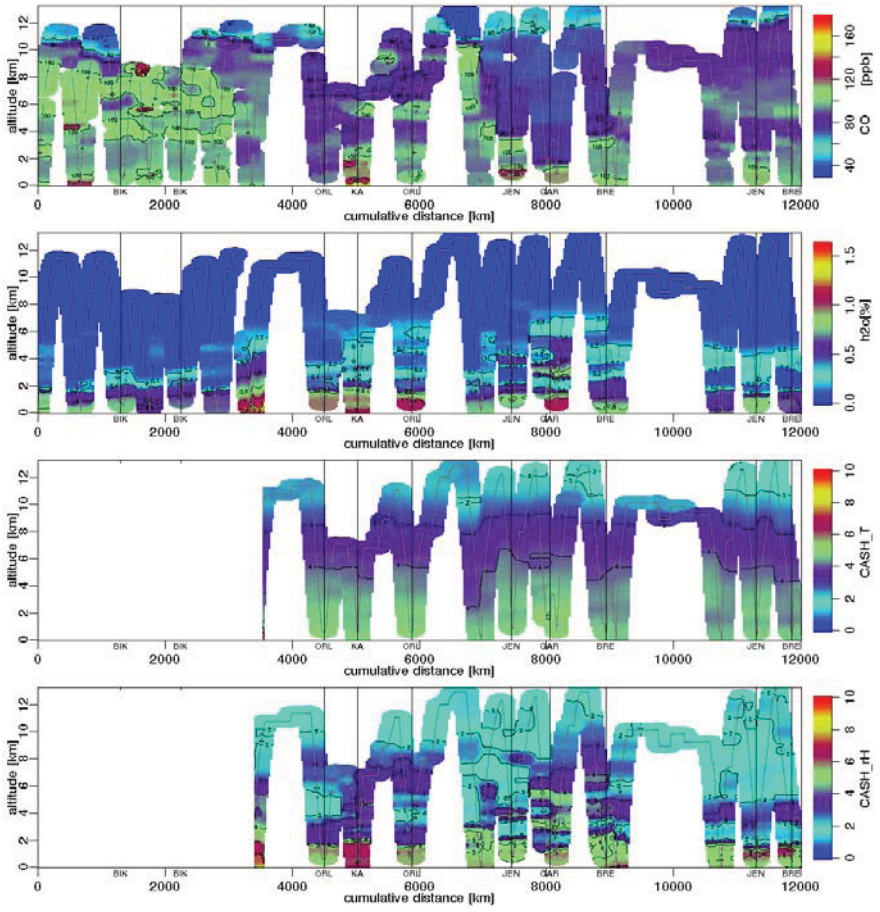

Figure 3.4: Cross sections of aircraft data over total flight track for CO, H_2O, temperature and relative humidity.

ferent meteorological situations at the stations. The structure of vertical tracer profiles are related to horizontal transport and vertical mixing. A mixed layer in the lowest part of the profile is often exhibited to signatures from nearby surface fluxes. In this context the atmospheric stability is an important factor, which can be determined by using the potential temperature Θ.

The potential temperature Θ was calculated from temperature T measured by the aircraft as

$$\Theta = T\left(\frac{p_0}{p}\right)^{\frac{R}{c_p}} \tag{3.1}$$

with p the ambient and p_0 the surface pressure, $R = 8.31 Jmol^{-1}K^{-1}$ the gas constant and $c_p = 29.07 mol^{-1}K^{-1}$ the specific heat capacity at constant pressure.

The planetary boundary layer (PBL) height is determined as the height where the potential temperature Θ equals the mean potential temperature of the mixed layer $\bar{T}_{ML}$ plus an excess temperature T:

$$\Theta = \bar{T}_{ML} + T_e \tag{3.2}$$

For the data of the IMECC campaign, the mean potential temperature T_{ML} was taken over the altitude range with an ambient pressure between 930 and 950 $\mathbf{mbar}$, and an excess temperature T_e of 5 $\mathbf{K}$ was chosen. The resulting planetary boundary layer heights for the profiles of the IMECC campaign vary between 1400 $\mathbf{m}$ and 3000 $\mathbf{m}$ (see Appendix E).

Overflights Jena OF1a/b were performed during nearly overcast sky conditions. The calculated PBL height is approximately 2100 $\mathbf{m}$ (see Fig. 3.6).

The profile data show a clear defined maximum around 1000 $\mathbf{m}$ of humidity and the CH_4 in the PBL. This illustrates a clear defined PBL that is well separated from the free troposphere through a strong temperature inversion. A second moisture layer can be identified around 4000 $\mathbf{m}$.

Overflights Bialystok OF1a/b and OF2a/b were performed during clear sky conditions. The calculated PBL height is approximately 3000 $\mathbf{m}$ (see Fig. 3.6).

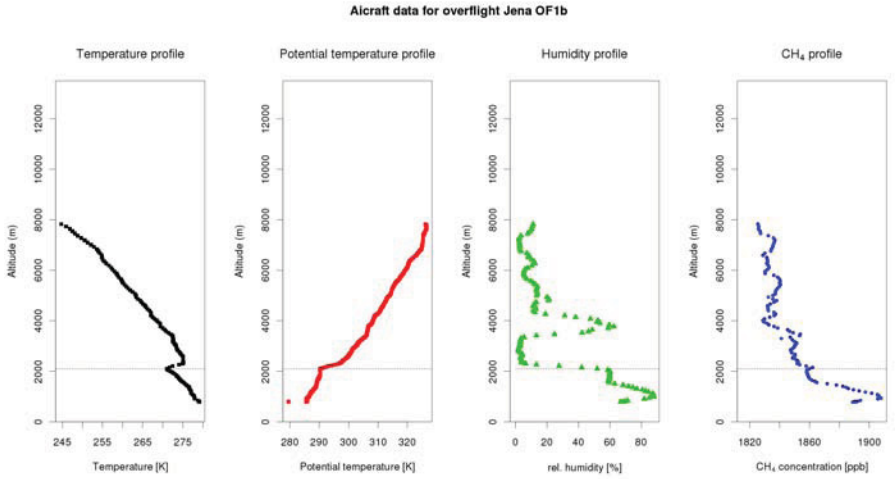

Figure 3.5: CH_4, H_2O and temperature data from aircraft in-situ measurements obtained during overflight Jena OF1b. The potential temperature was calculated from the temperature and pressure profile. The dashed line illustrates the calculated boundary layer height. At the time of the overflight the boundary layer height at Jena was roughly 2100 $\mathbf{m}$.

The humidity is linearly decreasing with altitude. The CH_4 profile shows no in-

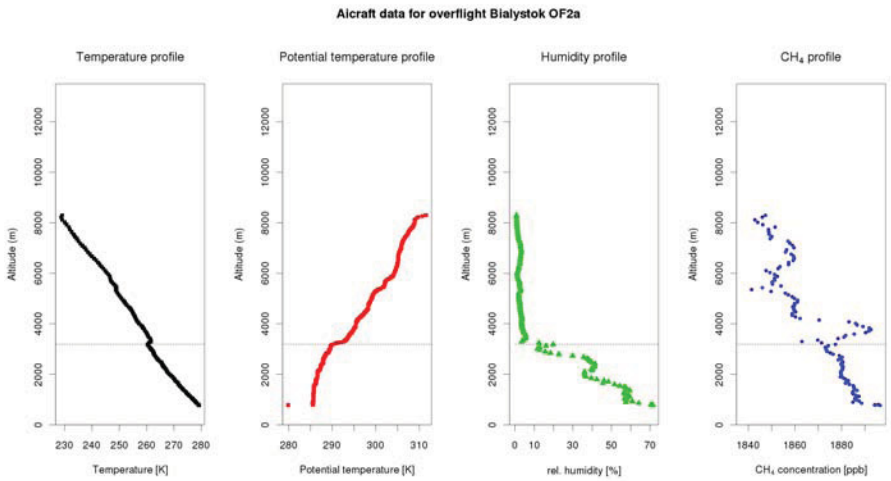

Figure 3.6: CH_4, H_2O and temperature data from aircraft in-situ measurements obtained during overflight Bialystok OF1b. The potential temperature was calculated from the temperature and pressure profile. The dashed line illustrates the calculated boundary layer height. At the time of the overflight the boundary layer height at Bialystok was roughly 3000 $\mathbf{m}$.

crease of CH_4 in the boundary layer. The temperature inversion is much smaller and the variation of CH_4 in the PBL is very weak.

All aircraft data obtained within the IMECC campaign with the calculated boundary layer height can be found in Appendix E. The next step of aircraft data processing is the extension of the aircraft profile to a total column. This can be found in Section 3.5.4, as it involves some details of the FTS data processing described in the following section.

3.4 FTS data processing

To ensure a uniform data processing of the FTIR data obtained within the IMECC campaign all spectra of the participating stations was processed in Jena using identical software and settings for all stations. For the analysis of the spectral data the TCCON standard retrieval software GFIT (Release 20090308 and Release 20091107) was used with different setting. The different settings included test with three different spectral line lists and the data pre-processing with IPP to apply a correction of solar intensity variations (SIVs). In these steps of FTS data processing all data were used unfiltered. For the calculation of calibration factor a quality criterion was introduced later on (see Section 3.6.1).

The uncertainties of the GFIT retrieval are a combination of statistical errors (residuals from the spectral fits) and systematic artifacts (e.g., errors/omissions in the spectroscopy, the modeling of the instrument response, and pointing-induced solar line shifts). The uncertainty estimation - the GFIT error - is a standard product of the GFIT software.

3.4.1 FTS data pre-processing with IPP

The weather situation during the IMECC campaign was sub-optimal for FTS measurements. Although the flights were scheduled using forecast products and satellite imagery, many stations suffered from cloudy sky conditions during the overflights. This introduces solar intensity variations to the measured interferograms. To enhance the quality of the spectra for further analysis, all FTS spectra of all participating stations were pre-processed with the Interferogram Processing Program (IPP).

This program is available in two versions:

- slice_ipp - for instruments that acquire the spectroscopic data directly from

the FTS instrument. The data is delivered in so called interferogram "slices", whereat one slice equals $\sim$10 $\mathbf{cm}$ optical path difference (OPD). This software is used for the spectral data of Bialystok, Bremen and Orleans.

- opus_ipp - for instruments that acquire the spectroscopic data via the OPUS software. This procedure saves the whole interferogram in one file. This software was used for the spectral data of Garmisch, Jena and Karlsruhe.

The IPP software does the following:

1. Read the interferogram (complete or all slices) into the memory
2. Correction of solar intensity variations (SIV) and finding the exact location of zero path difference (ZPD).
3. Applying of a phase correction to the corrected interferogram.
4. Performing of a Fast Fourier Transformation (FFT) to convert the interferogram into a spectrum.
5. Save user-specified spectral range (TCCON standard 3800 $\mathbf{cm^{-1}}$ to 15800 $\mathbf{cm^{-1}}$) of calculated spectrum to an output file.

The method of correction of SIVs was developed by Keppel-Aleks et al. (2007) and bases on the idea that division of the interferogram by the unmodulated DC detector signal restores the interferogram fringes to their correct amplitudes. An example of this effects on the spectrum can be seen in Fig. 3.7. The signal to noise (S/N) ratio increases significantly, the absorption lines are sharper and can so be better retrieved.

In the case of TCCON data, the unmodulated DC detector signal comes from smoothing the DC interferogram itself. Keppel-Aleks et al. (2007) implemented

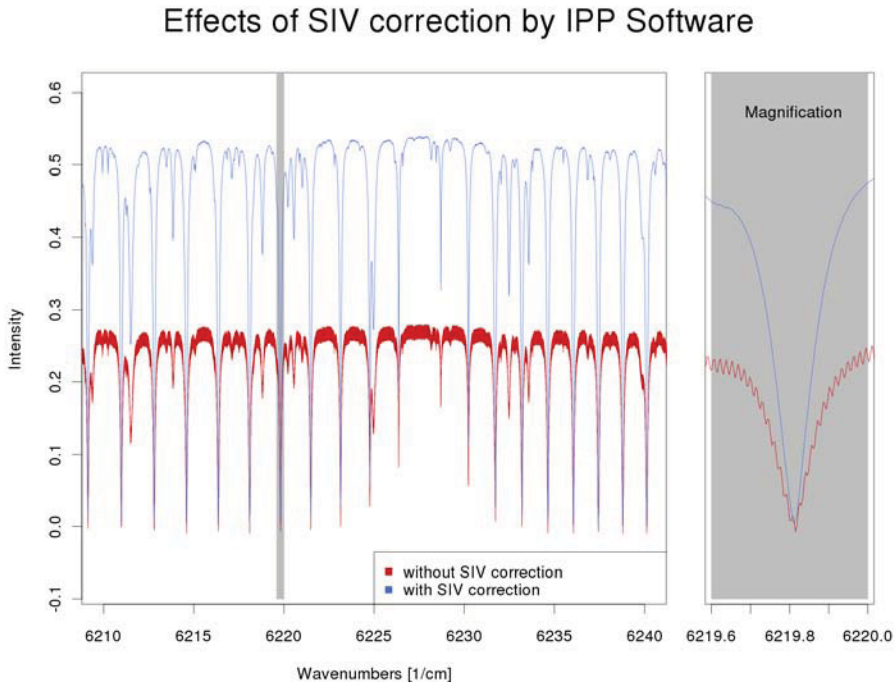

Figure 3.7: Influence of the correction of the solar intensity variations (SIV) performed with opus-ipp software on the noise level of the spectrum. In the magnification the resulting spectrum shows a significantly increased signal to noise ratio.

this scheme into the IPP software and applied this method to Park Falls and Darwin TCCON data. They showed that on partly cloudy days the pre-processing of the spectral data with the IPP software substantially reduces the scatter of the results of the GFIT retrieval. The same effect could be reproduced with the data of the IMECC campaign and is shown here for the example of Bialystok (see Fig. 3.8).

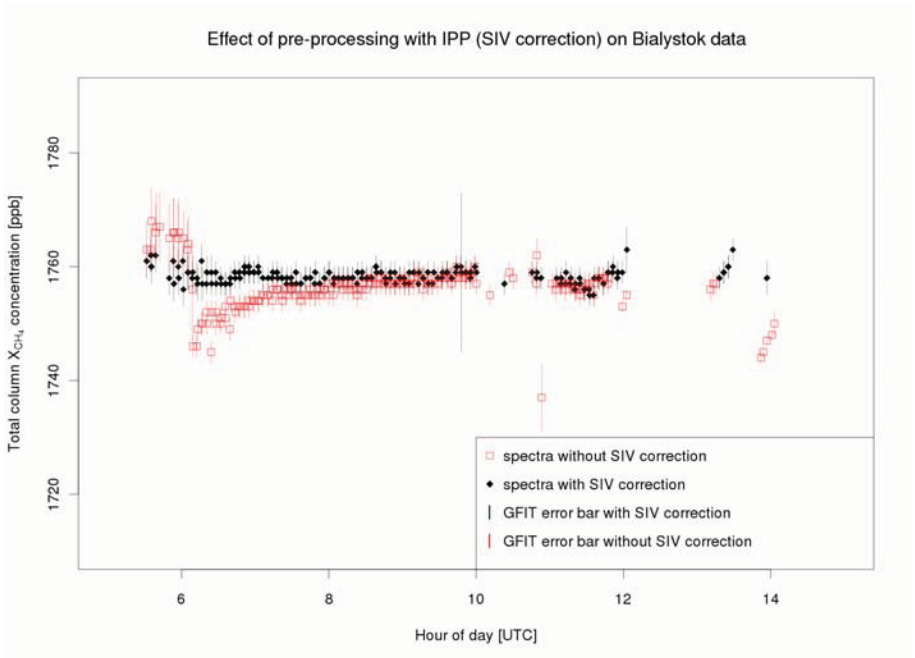

Figure 3.8: Influence of the SIV correction performed with the IPP software (in this case slice_ipp) on the GFIT retrieval on the IMECC flight campaign FTS data of Bialystok.

The scatter was reduced significantly and also the ”early morning feature“, probably cloud affected spectra, around 6 am could be corrected. The error bars of the early morning spectra are reduced and some outlier that were out of the plotting scales could be better retrieved (some obviously with large error bars).

For the Karlsruhe data of the IMECC campaign the influence of the IPP pre-

processing on the GFIT retrieval was versatile (see Fig. 3.9). On the one hand, the pre-processing lead to an overall increase in X_{CH_4} of $\sim$30 **ppb**. On the other hand, the amount of usable (meaning: processable) spectra could be increased from 4 to 44.

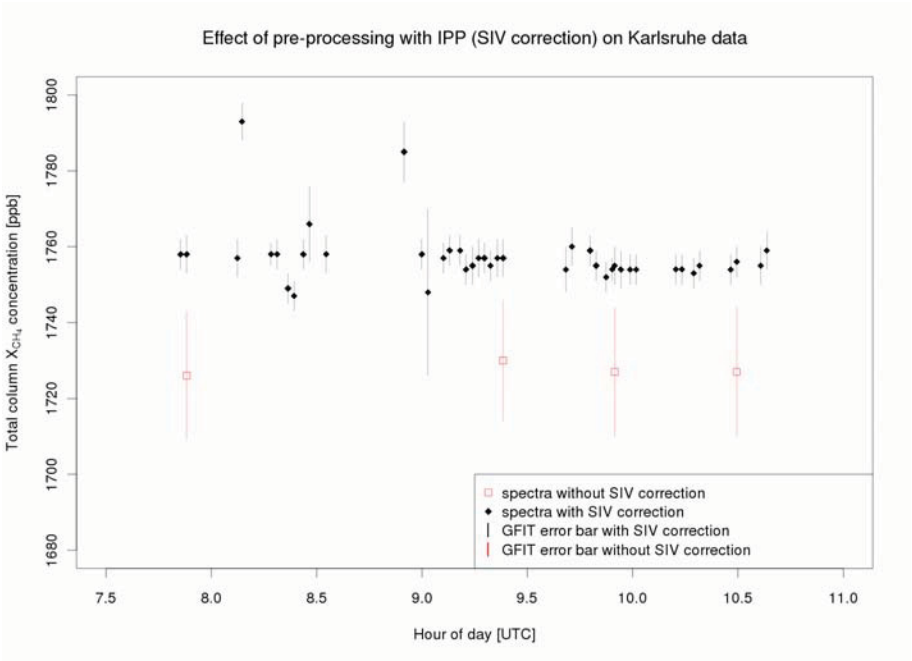

Figure 3.9: Influence of the SIV correction performed with opus-ipp on the GFIT retrieval on the IMECC flight campaign FTS data of Karlsruhe.

These effects can be explained with the peculiar meteorological situation during the campaign and some instrumental characteristics of the Karlsruhe FTS. During the overflight it was nearly completely overcast, only few gaps between the clouds could be used for measurements. The solar intensity variations within the measurements were high. Nevertheless the IPP software was able to correct most of the acquired spectra for the SIVs. This shows that the IPP software can not only cope with SIVs on partly cloudy day (Keppel-Aleks et al., 2007) but also with stronger variations of nearly overcast days.

The effect of the increase in X_{CH_4} can most likely be explained with detector settings of the Karlsruhe FTS. The Karlsruhe InGaAS detector has a limited bandwidth with a lower limit of 5490 $\mathbf{cm^{-1}}$ (TCCON standard 3800 $\mathbf{cm^{-1}}$), which is close to the absorption lines of CH_4 (see Section 2.4.2).

It is possible that this in a combination with strong SIVs lead to an underestimation of X_{CH_4} in the GFIT retrieval. The higher values X_{CH_4} retrieved when correcting for SIVs are more realistic and agree well with results of retrievals with other spectra analyzing software (Pscheidt, 2009).

In general, the data pre-processing with the IPP software was able to increase the quality of the spectral data used for the calibration process.

3.4.2 Intercomparison of IMECC results derived with different spectroscopic line lists

The spectroscopic line lists used for the GFIT retrieval are based on the HITRAN data base (Rothman et al., 2009) and contain updates for CO_2 (based on Toth et al. (2008)), CH_4 (based on Frankenberg et al. (2008)), O_2 (based on Newman et al. (1999), Yang et al. (2005) and Gordon et al. (2010)) and H_2O (based on Toth (2005) and Jenouvrier et al. (2007)).

Within the analysis of the IMECC data, three spectroscopic line lists were used: $atm\_20091001.101$, $atm\_20091201.101$ (which was used by Wunch et al. (2010).) and $atm\_20100908.101$. The difference between $atm\_20091001.101$ and $atm\_20091201.101$ is an update in the O_2 spectroscopy. This affects the retrieval of all species since the O_2 is used as reference to calculate the dry air mole fraction (DMF) (see Section 2.4.2, Eq. 2.1 and Eq. 2.3). Between $atm\_20100908.101$ and $atm\_20091201.101$ there are only minor changes and the results are expected to be very similar (Wunch, 2010).

Figures 3.10 and 3.11 show the difference of the GFIT retrieval with the dif-

ferent line list for Orleans and Bialystok.

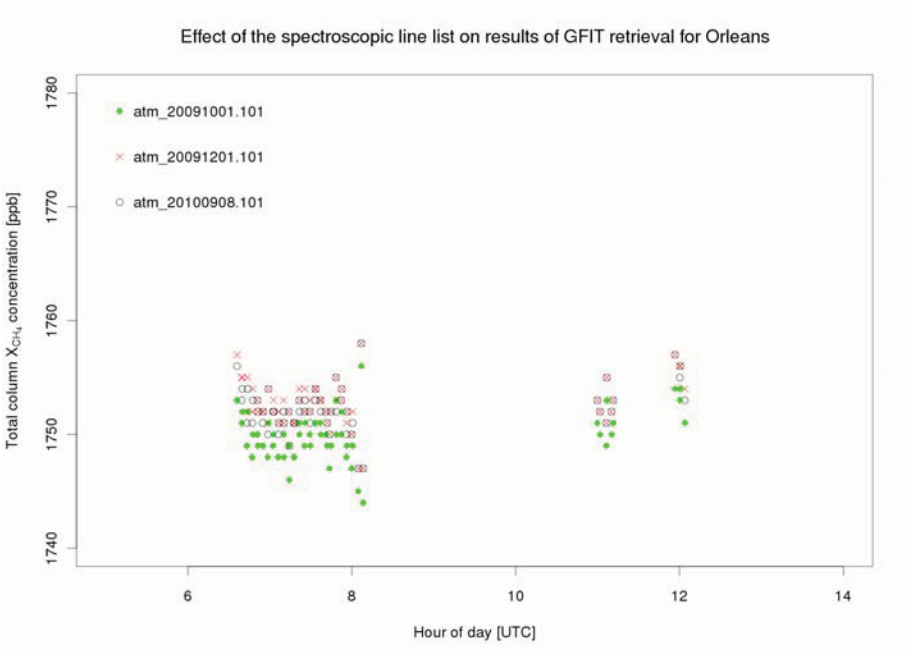

Figure 3.10: Influence of different HITRAN line list used in GFIT retrieval on the IMECC flight campaign FTS data of Orleans

As expected, the difference of the results of the $atm\_20091201.101$ and the $atm\_20100908.101$ line lists is very small. The minor updates of the spectroscopy do not have a big influence on the GFIT retrieval.

The difference between $atm\_20091001.101$ and $atm\_20091201.101$, however, is much larger. The results differ about 2.8 $\mathbf{ppb}$ (median) which agrees well with the expectations – based on the enhanced spectroscopy – of an increase of about 2 $\mathbf{ppb}$ for CH_4 and 0.5 $\mathbf{ppm}$ for CO_2 (Wunch, 2010).

In terms of comparability of the results of the IMECC campaign and the results of Wunch et al. (2010), further investigations were performed with the results of the GFIT retrieval using the $atm\_20091201.101$ line list.

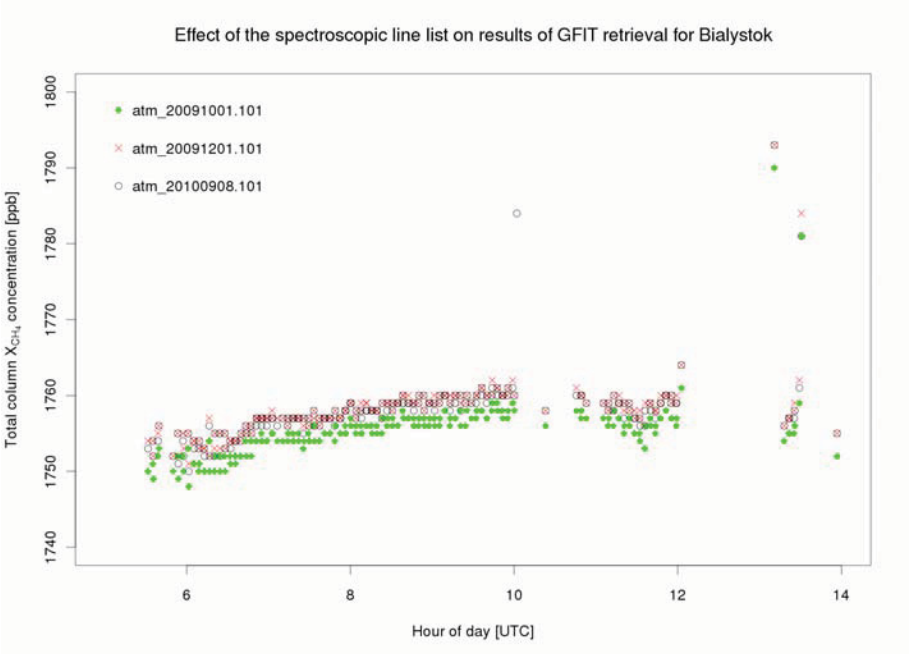

Figure 3.11: Influence of different HITRAN line list used in GFIT retrieval on the IMECC flight campaign FTS data of Bialystok

3.5 Data analysis

Data analysis was performed separately for CO_2 and CH_4. This Section describes the results of the CH_4 calibration. The results of the CO_2 calibration can be found in Messerschmidt, Geibel et al. (2011).

3.5.1 Method of intercomparison of two different measurement principles

As pointed out in Section 3.2, in-situ and FTS data can not be compared directly. Airborne in-situ data deliver information of abundances of one or more species in form of a profile (see Section 3.3.3). This profile has a high vertical resolution, the vertical coverage, however, is limited to a coverage of $<80\%$ of the total column. The aircraft data can only deliver a "partial column". For the calibration, the aircraft profile has to be extended to an artificial aircraft total column (see Section 3.5.4).

FTS spectral data deliver total column dry air mole fractions (DMF) for the individual species. The vertical coverage of this type of measurement can be seen as unlimited, since it covers all parts of the atmosphere from the radiation source (sun) to the spectrometer (surface). The results of the GFIT retrieval deliver no information of the vertical distribution of the species. Rodgers and Connor (2003) developed a method that allows the intercomparison of aircraft and FTS data (see Eq. 3.3).

$$\widehat{c_s} = \gamma c_a + a^T(x_h - \gamma x_a) \tag{3.3}$$

with $\widehat{c_s}$: retrieved DMF based on airborne measurements, γ: FTS retrieval scaling factor, c_a: FTS a priori DMF, a^T: FTS column averaging kernel, x_h: aircraft profile (extended), x_a: FTS a priori profile.

As pointed out by Wunch et al. (2010), for a GFIT scaling retrieval the aver-

aging kernels are calculated for the scaled solution mole fraction profile. So the point of linearization of the "Taylor expension" producing Eq. 3.3 is γx_a and not x_a.

The presented method uses the aircraft profile extended to a total column, the FTS dry air mole fractions, the GFIT a-priori profiles, the retrieval scaling factor and the GFIT averaging kernels (AK) to retrieve the DMF of the extended aircraft column. This result is then used to calculate the calibration factor for the FTS measurements.

The a-priori profiles are based on MkIV balloon profiles and profiles obtained from the Atmospheric Chemistry Experiment (ACE-FTS) onboard SCISAT-1 - both measured in the 30-40N latitude range from 2003 to 2007. They are converted with the help of auxiliary data (air temperature (AT), geopotential height (GH), specific humidity (SH), and tropopause pressure (TP) from the NCEP database (Kalnay et al., 1996)) specific for the location and time of the FTS measurement to a local a-priori profile for each day. Within the GFIT analysis this local a-priori profile is weighted with a time-dependent averaging kernel and scaled with an retrieval scaling factor to perform a spectral fit of the measured spectral data.

Wunch et al. (2010) used the method of Rodgers and Connor (2003) for the analysis of earlier calibration campaigns.

The derivation of the equation of the column-averaged aircraft CH_4 DMF can be found in Wunch et al. (2010) and is analog to Section 2.4.2:

$$\widehat{c_s} = \gamma \frac{\Gamma^{apriori}_{CH_4}}{\Gamma_{dryair}} + \left(\frac{\Gamma^{aircraft}_{CH_4,ak} - \gamma \Gamma^{apriori}_{CH_4,ak}}{\Gamma_{dryair}} \right) \tag{3.4}$$

with γ: FTS retrieval scaling factor, Γ_{dryair}: total column of dry air, $\Gamma^{apriori}_{CH_4}$: total vertical column of CH_4, $\Gamma^{aircraft}_{CH_4,ak}$: column averaging kernel-weighted vertical column of the aircraft, $\Gamma^{apriori}_{CH_4,ak}$: column averaging kernel-weighted vertical a priori.

3.5.2 Correction of GFIT a-priori CH_4 profiles via HF correlation

As indicated by Wunch et al. (2010) for an more precise retrieval of X_{CH_4} the estimated tropopause heights of the GFIT a-priori CH_4 profiles have to be corrected. This is done by using the CH_4-HF-correlation that was observed by Luo et al. (1995) and Washenfelder et al. (2003). The CH_4-HF-correlation bases on the complete absence of HF in the troposphere. To apply this correction the results of a GFIT X_{HF} retrieval for the individual station are used to calculate an altitude shift for the CH_4 a-priori profiles (see Fig. 3.12).

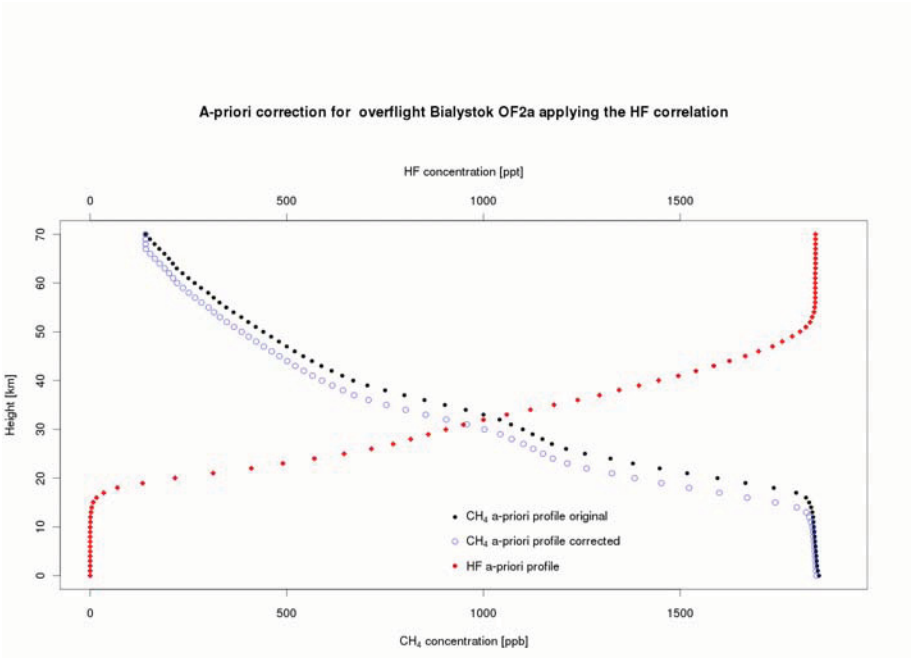

Figure 3.12: Applying of the CH_4-HF-correlation to the CH_4 GFIT a-priori profile shown on the example of overflight Bialystok OF2a.

The modified GFIT a-priori profiles were used for a re-analysis of all IMECC spectral data. The results of the re-analysis were used for the determination of the correlation factor (see Section 3.6.1).

3.5.3 Averaging kernels

For the method of Rodgers and Connor (2003) described in 3.5.1 the GFIT averaging kernels (AK) are needed. The AKs are used to weigh the GFIT a-priori profile for the spectral fit. They strongly depend on the solar zenith angle (SZA) and change over the day. However, for the temporally close overflights (like Bialystok OF1a and OF1b) the AKs are nearly identical. Figure 3.13 shows the AKs that were used for the calculation of the calibration factor.

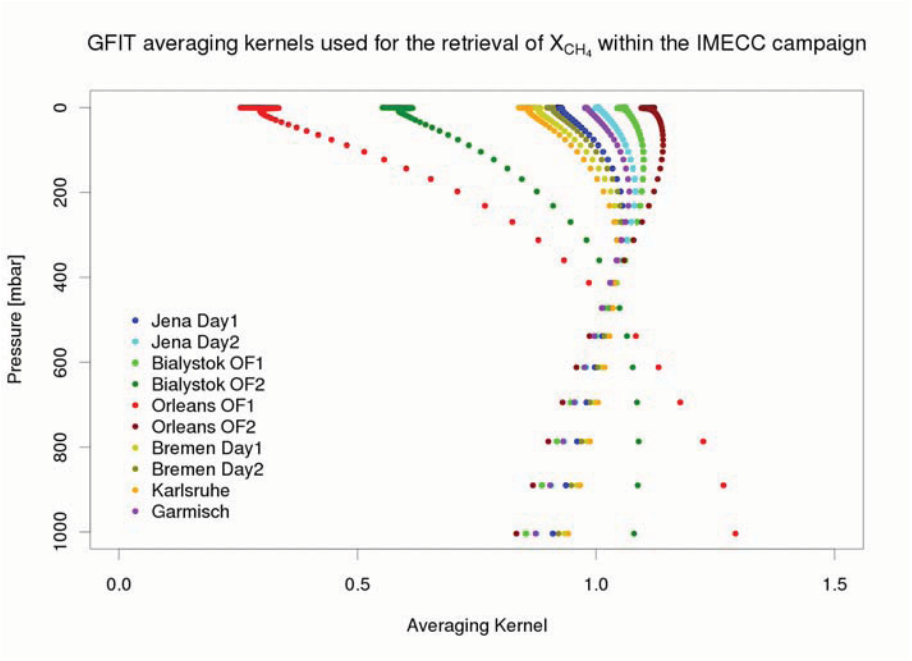

Figure 3.13: GFIT averaging kernels (AK) used for the retrieval of X_{CH_4} for the individual overflights that were used for the calculation of the calibration factor.

3.5.4 Aircraft total column extension

The FTS measurements cover the whole atmosphere, from the surface to the top of the stratosphere. Airborne in-situ measurements, like those performed during

the IMECC campaign, have limited vertical coverage. Neither is it possible to measure at the surface due to the lack of an airport close to the FTIR stations, nor is it possible to go altitudes higher than 13 $\mathbf{km}$ to cover the upper part of the atmosphere. In most cases the aircraft data are limited to an altitude range from approximately 300$\mathbf{m}$-13000$\mathbf{m}$ (see Fig. 3.3). So the aircraft can only deliver a ”partial column”. To compare the aircraft data with the FTS data, this partial column has to be extended to a total column.

For the FTS stations Orleans and Bialystok ground-based in-situ data from the nearby tall-towers were used to extend the aircraft data to the ground. For the other stations the values measured at the lower most altitude by the aircraft were extrapolated to the surface. The uncertainty was estimated conservatively using the variance of the lowest aircraft data. For the stratospheric part of the column the GFIT a-priori weighted with the retrieval scaling factor was used (see Fig. 3.14). The a-priori was weighted with the GFIT averaging kernel and scaled by the relation factor between weighted a-priori and retrieved column for the individual overflight (see section 3.5.1). The error of the stratospheric mixing ratio was estimated conservatively as 1% of the scaled and weighted a-priori. This corresponds to the shifting of the profile by 1 $\mathbf{km}$ up and down performed by Wunch et al. (2010). An overview of the individual uncertainties of the extrapolation to the ground, the stratospheric extension by using the GFIT a-priori and the aircraft data can be found in Table 3.3. The extended aircraft columns were then used to calculate the aircraft DMF needed for Equation 3.3.

Figure F.1 to Figure F.4 in Appendix F show the extended aircraft columns for all stations and overflights.

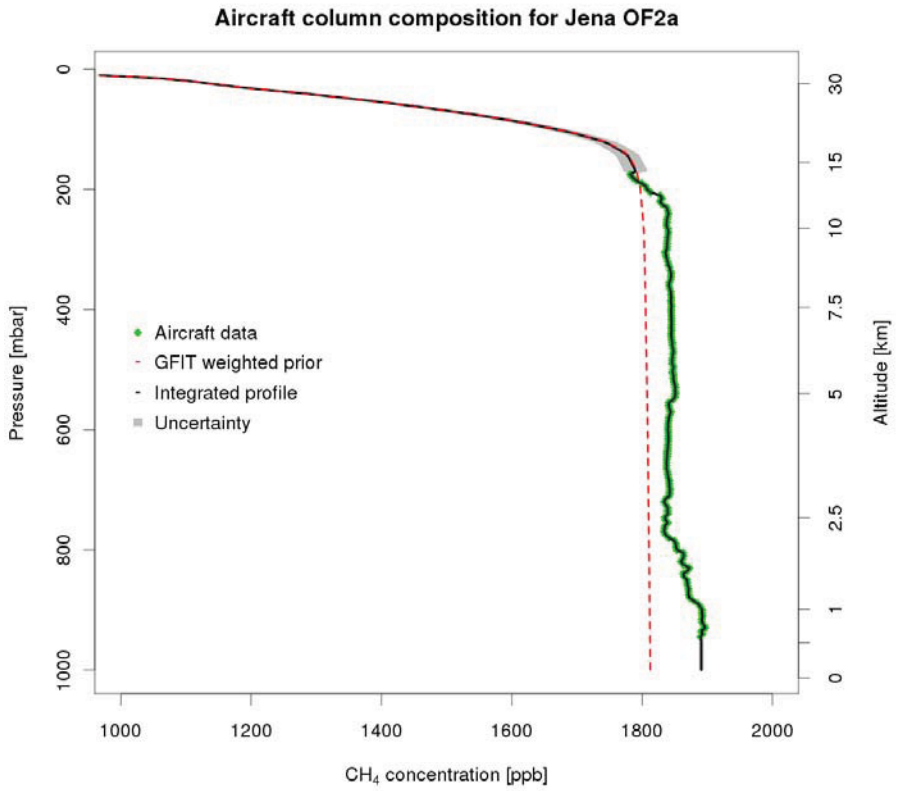

Figure 3.14: Example for the extension of aircraft data to a total column (Jena OF2a). The green partial column represent the aircraft in-situ data. This column was extended by the weighted GFIT a-priori in the stratosphere. The lower part was extended to the ground by adding ground-based in-situ data where available. Otherwise the profile was extrapolated to the surface. The gray area represent the uncertainty of the extended parts. The red line represents the weighted GFIT a-priori profile.

Table 3.3: List of the individual uncertainties and their contribution in % to the total aircraft DMF error: extrapolation to the ground, the aircraft data and the stratospheric extension by using the GFIT a-priori.

Overflight	Mean uncertainties for						**Total [ppb]**
	Ground		Aircraft		Stratosphere		
	[ppb]	[%]	[ppb]	[%]	[ppb]	[%]	
BI OF1a	4.39	5.35	0.38	7.51	15.69	87.14	4.02
BI OF1b	3.34	1.81	0.37	4.32	16.53	93.87	6.08
BI OF2a	5.63	6.16	0.26	2.63	16.42	91.21	5.30
BI OF2b	4.06	6.29	0.32	5.15	15.84	88.56	3.56
BR OF1a	22.74	30.62	0.31	6.72	15.01	62.65	3.55
BR OF2a	3.49	7.67	0.34	10.02	14.98	82.32	2.64
GM OF1a	8.61	20.46	0.24	4.93	15.22	74.61	3.66
JE OF1a	9.38	19.32	0.32	6.52	15.43	74.16	3.64
JE OF1b	7.35	7.74	0.36	3.03	16.72	89.23	6.87
JE OF2a	3.32	6.18	0.30	7.86	15.37	85.96	3.10
JE OF2b	5.34	6.30	0.31	8.31	15.37	85.40	3.11
KA OF1a	7.51	0.51	0.46	3.59	17.14	95.91	7.49
OR OF1a	7.06	11.70	0.41	7.69	15.42	80.61	2.69
OR OF1b	1.08	1.19	0.40	3.10	16.50	95.70	5.09
OR OF2a	3.08	4.72	0.44	8.07	15.88	87.21	4.32
OR OF2b	3.86	3.99	0.48	4.55	16.67	91.46	6.88
average	6.26	8.75	0.36	5.88	15.89	85.38	4.50

3.6 Results of the CH_4 calibration

3.6.1 Calibration factor between aircraft and FTIR instruments

For the derivation of the calibration factor obviously a data point consisting of an aircraft value and a FTS value for each overflight is needed. The aircraft value was calculated by integrating the extended aircraft column (see Section 3.5.4). To eliminate the risk of single outliers affecting the FTS values of the calibration, all spectral data within a time window of +/- 30 min around the spectrum closest to the aircraft overflight was chosen. As a data quality criterion all spectra with a GFIT error (see Sec. 3.4) $> 10\mathbf{ppb}$ were excluded. For spectra fulfilling both criteria the median value of the DMF was calculated (see Fig. 3.15). This figure illustrates, that the GFIT error is a good but not a perfect quality criterion. There are still single outliers (e.g. due to imperfect SIV correction) remaining, This shows, that the spectral fit and error estimation are not allways accurate. By calculating the median value, those outliers do not affect the calibration factor. This value represents the FTS data point for calibration.

In a first step, the results of the GFIT retrieval with standard a-priori profiles were investigated. Like in Wunch et al. (2010) the data points were fitted with an error-weighted least-squares fit as published in York et al. (2004) to derive the calibration factor $\psi_{standard\ ap}$. The mathematical details of the fit procedure can be found in Appendix G. In agreement with the previous investigation, an artificial calibration point in the origin was added (Wunch, 2010).

The fit of the IMECC campaign data illustrates, that the calibration factor $\psi_{standard\ ap}$ = 0.978 +/- 0.002 of the earlier campaign (Wunch et al., 2010) can be reproduced even with the GFIT standard a-priori profiles (see Fig. 3.16). To be able to compare the results of the IMECC campaign data with the data of Wunch et al. (2010), however, the GFIT retrieval had to be repeated using the extended

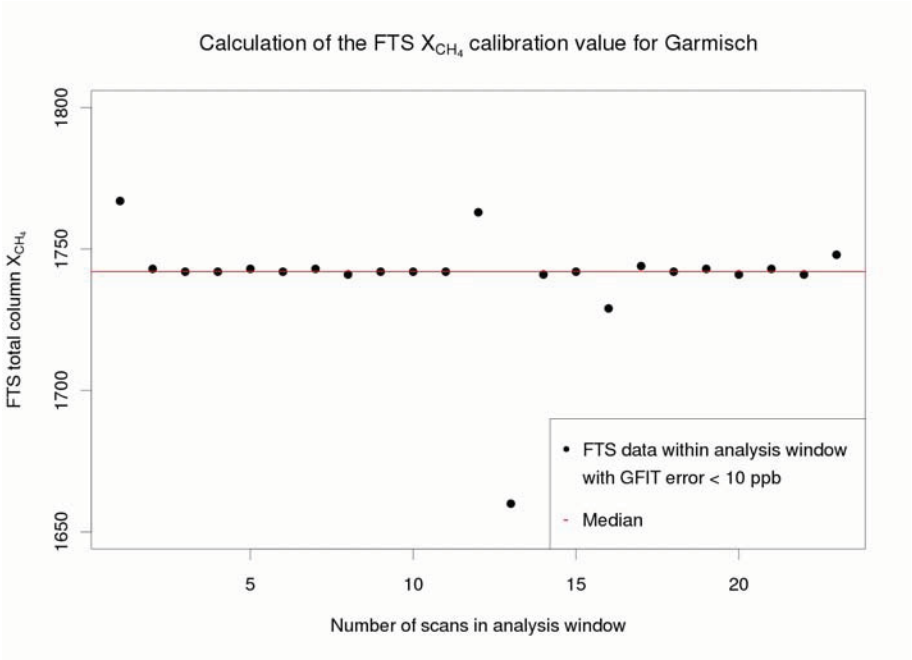

Figure 3.15: Calculation of the FTS data point for the derivation of the calibration factor on the example of Garmisch. A time window of +/- 30 min around the spectrum closest to the aircraft overflight was chosen. An a data quality criterion was a GFIT error $< 10\mathbf{ppb}$. For spectra fulfilling both criteria the median value of the DMF (red line) was calculated. This value represents the FTS data point for calibration.

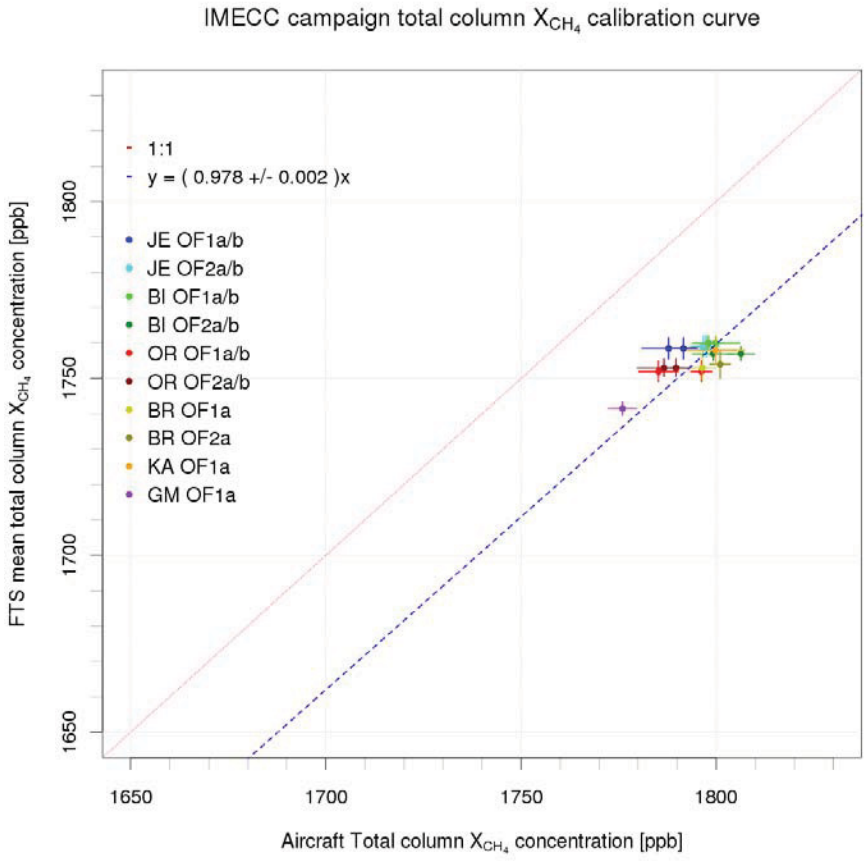

Figure 3.16: Calibration factor of CH_4 for the IMECC stations derived from GFIT retrieval with standard a-priori.

aircraft profile from Section 3.5.4 as a-priori profile for the GFIT retrieval. The different a-priori has minor effects of +/-2$\mathbf{ppb}$ on the retrieval for the individual stations (see Fig. 3.17). This is in the same order of magnitude as the typical GFIT error for CH_4.

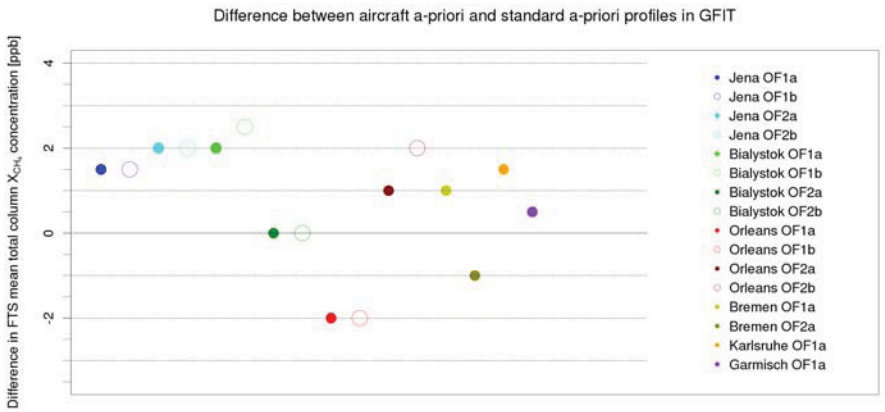

Figure 3.17: Difference in the GFIT retrieval between aircraft profile and standard a-priori for the individual stations.

Figure 3.18 shows the results of the fit for this procedure. The resulting calibration factor $\psi_{aircraft\ ap}$ = 0.978 +/- 0.002 is exactly the same as $\psi_{standard\ ap}$ and the one derived by Wunch et al. (2010).

In the next step, the Wunch et al. (2010) data was added to the dataset and the fitting procedure was repeated (see Fig. 3.19) to derive a calibration factor ψ_0 for all stations (IMECC + Wunch et al.). As a result, the calibration factor does not change, but the uncertainty is reduced by $\sim$68$\%$ (from +/-0.00205 to +/-0.00066).

To illustrate the quality of the fit, the residuals ($DMF_{FTS} - \psi_0 * DMF_{aircraft}$) for all calibration points are shown in Figure 3.20. The residuals indicate a tendency to a slightly higher calibration factor than the one derived by Wunch et al. (2010). However, most of the calibration points include the calibration factor with

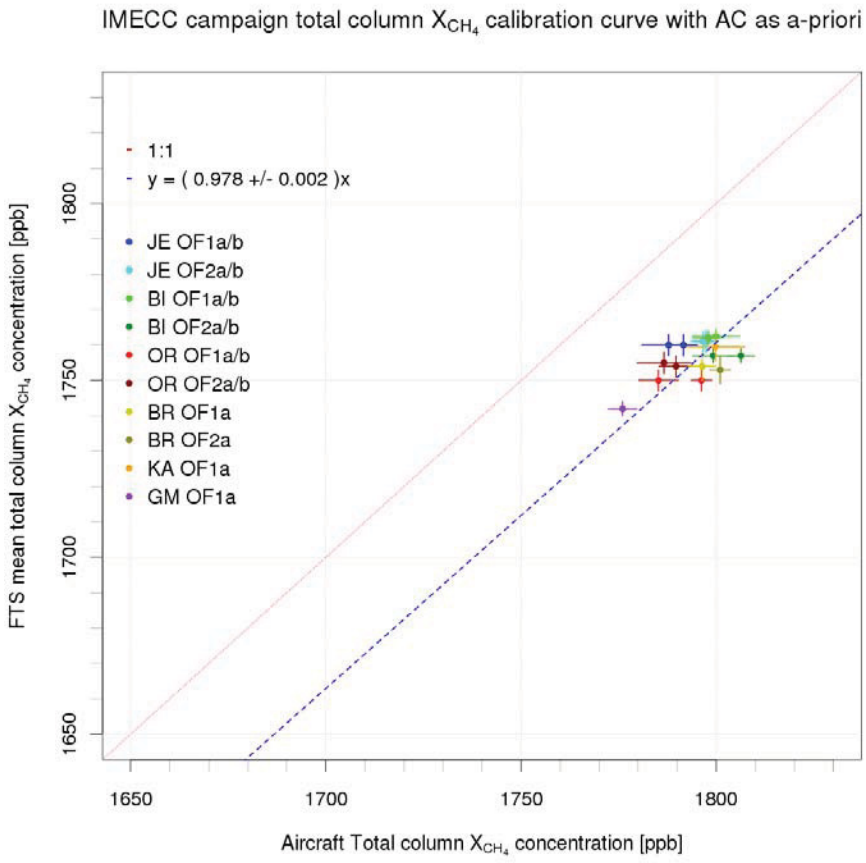

Figure 3.18: Calibration factor of CH_4 for the IMECC stations derived from GFIT retrieval with aircraft profiles as a-priori.

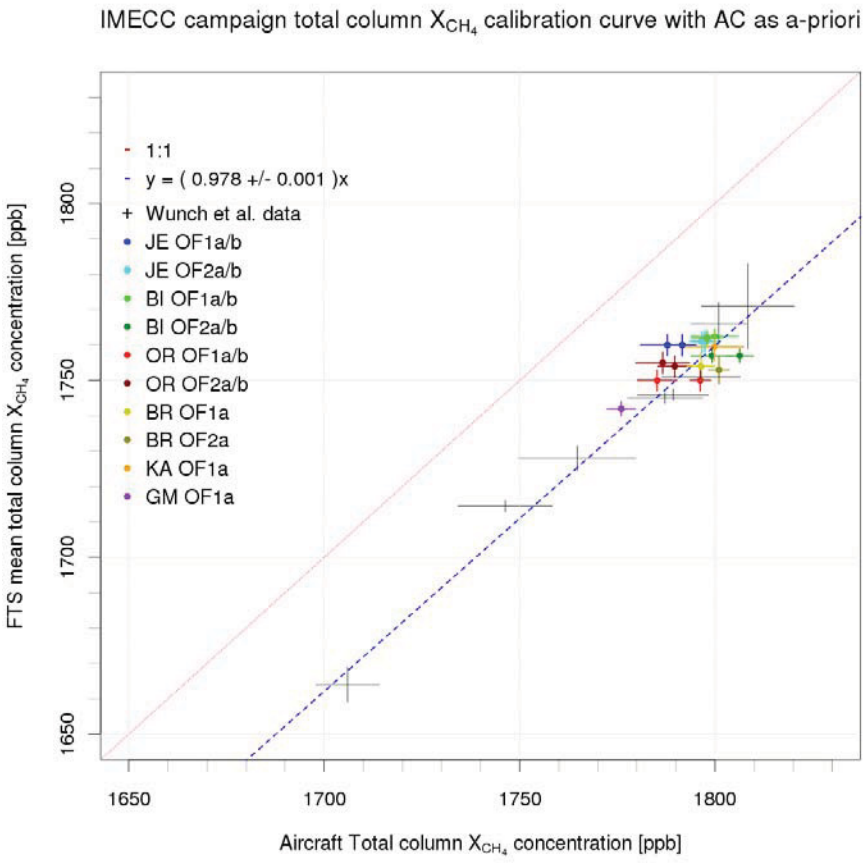

Figure 3.19: Calibration factor of CH_4 for all data including Wunch et al. (2010) data derived from GFIT retrieval with aircraft profiles as a-priori.

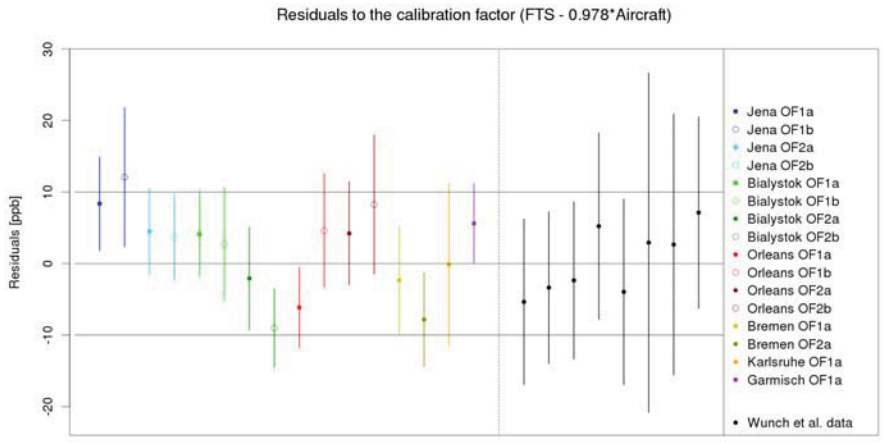

Figure 3.20: Residuals ($DMF_{FTS} - \psi_0 * DMF_{aircraft}$) calculated for all calibration points using aircraft profiles as a-priori for the GFIT retrieval. The error bars are the squared sum of the FTIR and the aircraft errors.

their error bars and have their median well within the same range as the data by Wunch et al. (2010) (+/- 10 $\mathbf{ppb}$).

3.6.2 Influence of the individual overflights of the IMECC stations on the calibration factor

To test the hypothesis that an independent calibration factor is needed for each FTS station, each overflight was analyzed separately. The York et al. (2004) fitting procedure was used to derive a separate calibration factor for the individual overflight and on for the associated remaining other calibration points (see Fig. 3.21).

It is obvious, that the overflights Jena OF1a, Jena OF1b, Bialystok OF2b, Orleans OF1a and Bremen OF2a have no overlap of their error bars with the calibration factor of the associated remaining stations. However, for one-sigma error bars only 68 $\%$ of the data points are expected to overlap. To test their influence,

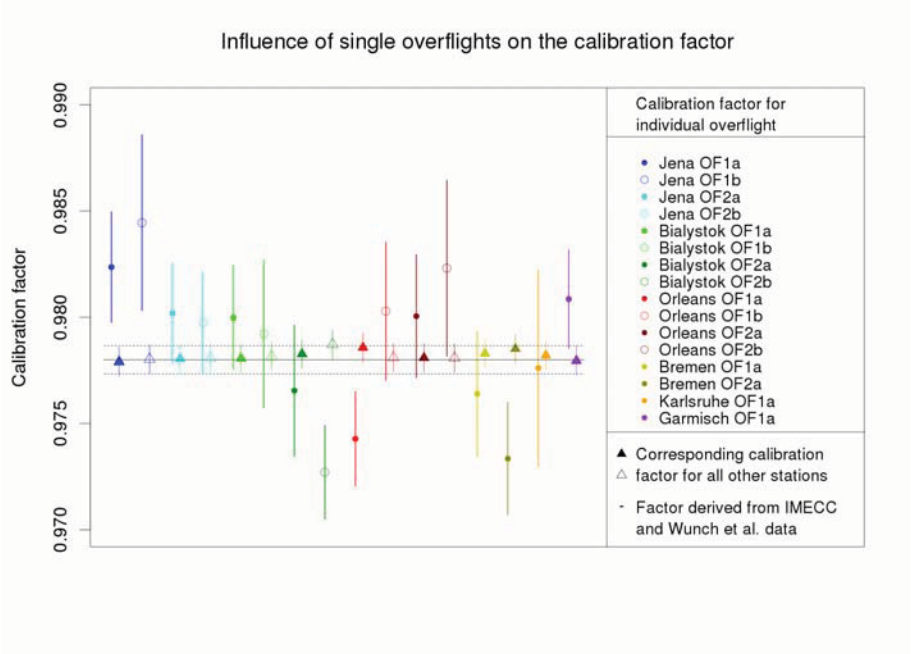

Figure 3.21: Influence of the individual overflights of the IMECC stations on the calibration factor. For this study, the calibration factors for individual overflight and the artificial calibration point in the origin were derived (full and empty dots). An additional calibration factor was calculated for the corresponding remaining overflights and the artificial calibration point in the origin (full and empty triangles). Overflights Jena OF1a, Jena OF1b, Bialystok OF2b, Orleans OF1a and Bremen OF2a have no overlap of their error bars with the calibration factor associated remaining stations.

the mentioned overflights are excluded from the dataset and the calibration factor ψ is re-calculated (see Fig. 3.22).

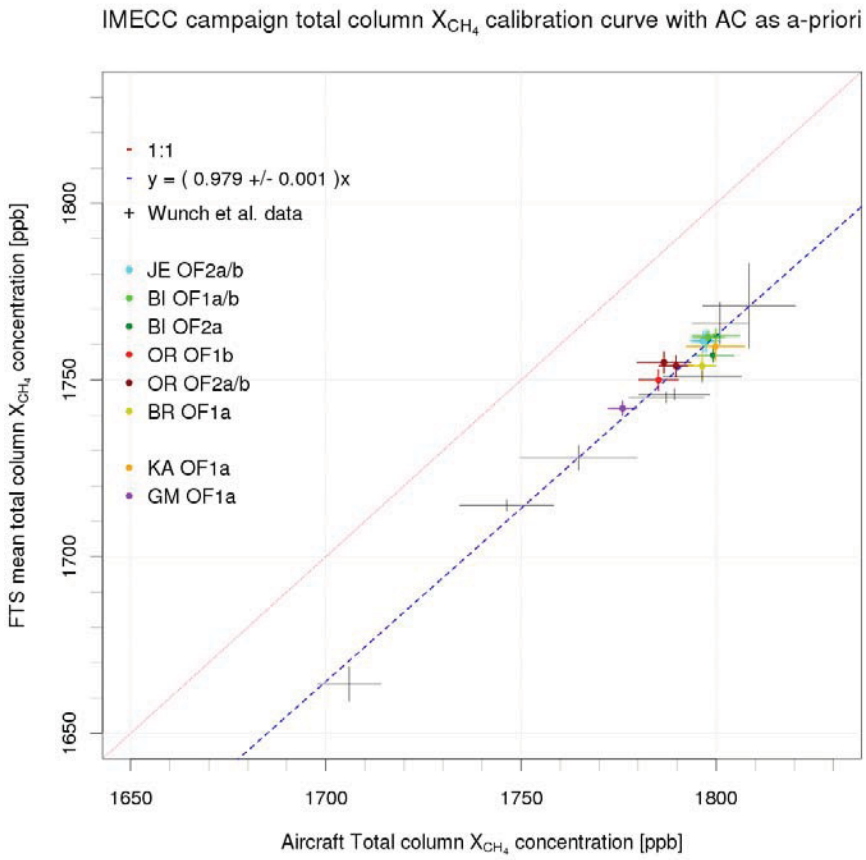

Figure 3.22: Calibration factor $\psi_{reduced}$ of CH_4 for all data including Wunch et al. (2010) data derived from the reduced dataset.

As already indicated in Section 3.6.1 the IMECC stations have a tendency to a slightly higher calibration factor. However, the resulting calibration factor for the reduced dataset $\psi_{reduced}$ = 0.979 +/- 0.001 is not significantly different from the one derived from the complete dataset, respectively from the one from Wunch et al. (2010). All calibration factors are statistically consistent within their uncertainties. This supports the hypothesis that a calibration factor is only needed

for the measurement principle, not for individual sites.

3.6.3 Influence of the amount of aircraft data on the calibration points

An important factor for the calculation is the vertical coverage of aircraft data in the artificial aircraft total column as shown in section 3.5.4. The fewer aircraft information is available the more a-priori has to be used to fill the profile.

To illustrate the effect of the vertical coverage of aircraft data in the aircraft total column, a sensitivity test was performed. The vertical coverage of aircraft data was manually reduced to data measured below a certain pressure value. The remaining part of the column was filled with the scaled and AK-weighted a-priori (see 3.5.4). Then the calibration point (FTS to aircraft ratio) was re-calculated. The results show the expected behavior of an increasing FTS to aircraft ratio with decrease of the vertical coverage of aircraft data (see Fig. 3.23).

In an extreme scenario of no aircraft data, the profile is identical with the scaled a-priori. For Equation 3.3 in Section 3.5.1 the consequences are that the calibration factor becomes 1. This may seem counter-intuitive at first glance. However, this does not mean that the FTS data become better with fewer aircraft data points. It rather indicates that with fewer aircraft measurements, one is left with only a priori knowledge about the calibration factor. In the case of no aircraft data this means no information about the calibration factor.

Having these results in mind when looking at the individual aircraft profiles in Section 3.5.4, it is obvious that one can expect different behavior of different overflights due to the vertical coverage of aircraft data.

A good example are the first two overflights of Jena (see Fig. F.1, upper part). Overflight *Jena OF1a* has a maximum flight altitude of 13 $\mathbf{km}$, overflight *Jena OF1b* of approximately 8 $\mathbf{km}$. Due to the time difference between overflight and

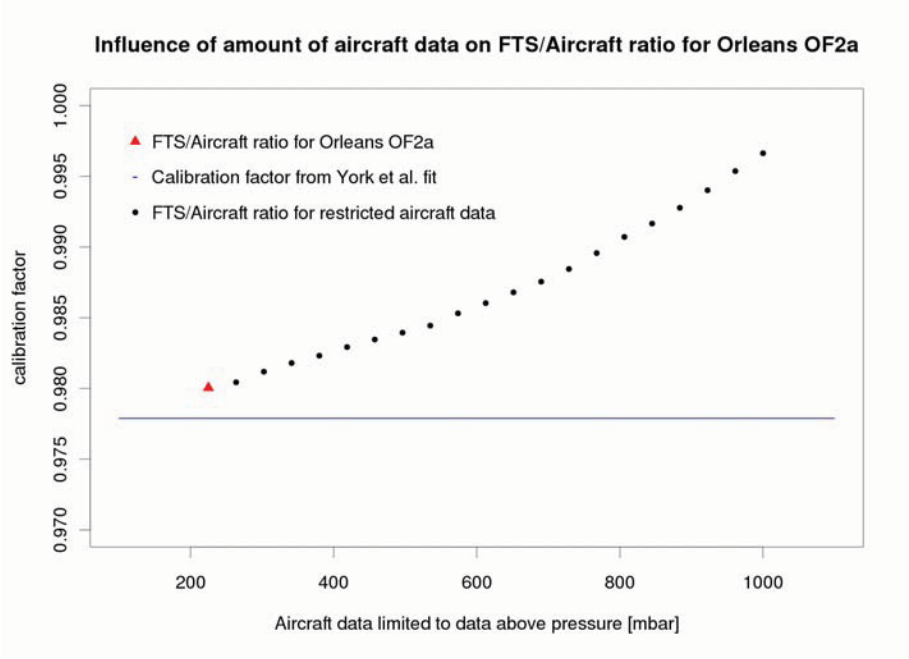

Figure 3.23: Influence of the vertical coverage of aircraft data in the aircraft column on the derived FTS to aircraft ratio illustrated on the example of Orleans OF2a. The red triangle symbolizes the FTS to aircraft ratio for this overflight. The blue line is the calibration factor determined for all stations (incl. Wunch et al. (2010) data). The black dots symbolize the FTS to aircraft ratio calculated with a restricted vertical coverage of aircraft data in the aircraft column. The fewer aircraft data are available the more the calibration factor converges to 1.

first spectrum, for these calibration points exactly the same FTS data are used. The aircraft data (green line in Fig. F.1) are similar as well. Hence, the difference in the residuals in Fig. 3.20 for these two calibration points is most likely due two the different amount of aircraft data. The residual of *Jena OF1a* is smaller and the calibration factor for this individual calibration point closer to 0.978. The residual of *Jena OF1b*, however, is larger and the calibration factor for this individual calibration point further away from 0.978 (see Fig. 3.21).

3.7 An improved approach to minimize the effect of maximum flight altitude

The previous results have shown that the calibration points with aircraft profiles with less vertical coverage are biased towards 1. This is caused by the extrapolation of the aircraft profiles with the GFIT a-priori. The less aircraft information contribute to the extended aircraft total column, the more the extended aircraft column equals the GFIT a-priori. A possible solution for this problem is to extrapolate the aircraft column with a calibration-factor-corrected GFIT a-priori profile (see Fig. 3.24). To be able to do this, the calibration factor has then to be derived in an iterative calculation. The approach of Rodgers and Connor (2003) is modified to:

$$\widehat{c_s} = \frac{\gamma c_a}{\psi_{iterative}} + a^T \left(x_h - \frac{\gamma x_a}{\psi_{iterative}} \right) \tag{3.5}$$

with $\widehat{c_s}$: retrieved DMF of the aircraft, γ: FTS retrieval scaling factor, c_a: FTS a priori DMF, a^T: FTS column averaging kernel, x_h: aircraft profile, x_a: FTS a priori profile, $\psi_{iterative}$: iteratively derived calibration factor.

Starting from a calibration factor $\psi_{iterative}$ = 1, the calibration points are calculated and the fitting procedure (see Section 3.6.1) is applied. This leads to a new $\psi_{iterative}$. The procedure is repeated until the resulting $\psi_{iterative}$ is equal with the previous $\psi_{iterative}$. Since the the a priori profile has only small influence on the GFIT retrieval (see Fig. 3.17 in Section 3.6.1), the GFIT retrieval with an $\psi_{iterative}$-corrected aircraft profile as a-priori for each iteration step was not performed for this study. The new extended aircraft profiles (see Fig. 3.24) show, that the aircraft profiles extrapolated with the iteratively scaled a-priori are no longer affected by bias towards 1. Profiles with less aircraft information are now more equal to the calibration-factor-scaled a-priori profile. As a consequence, profiles

that were biased toward 1 are now biased towards the iterative calibration factor $\psi_{iterative}$.

The resulting calibration factor for the IMECC campaign dataset $\psi_{iterative}$ = 0.974 +/- 0.002 (see Fig. 3.25) is significantly different from the one derived by the method of Wunch et al. (2010).

By using this iterative approach, the calibration points of the individual overflights show roughly the same scatter and residuals (see Fig 3.26) as before. The standard deviation for both residual calculations is the same (6 $\mathbf{ppb}$). Temporally close overflights (Bialystok OF2A/B, Orleans OF1A/B) with different maximum flight altitudes, however, are now more consistent. The influence of the vertical coverage of the aircraft data is reduced to a minimum. The difference of 0.004 between ψ_0 and $\psi_{iterative}$ corresponds to a $\sim$7$\mathbf{ppb}$ offset for the FTS DMFs.

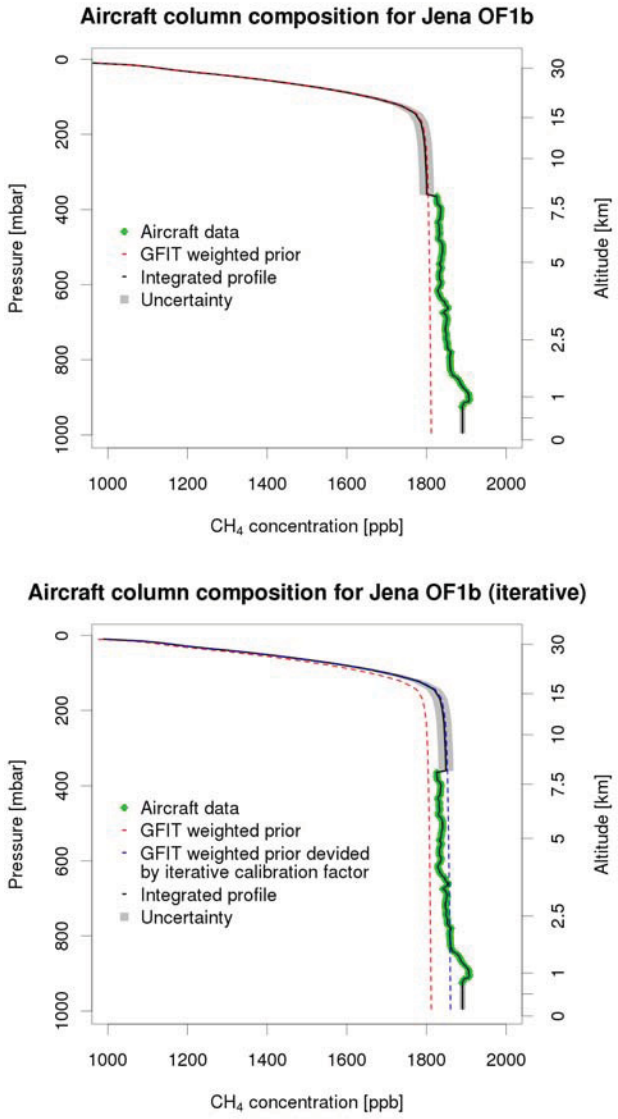

Figure 3.24: Difference between standard extrapolation of the aircraft profile (A) and extrapolation using an a-priori (B) for Jena OF1b scaled with an iteratively derived calibration factor.

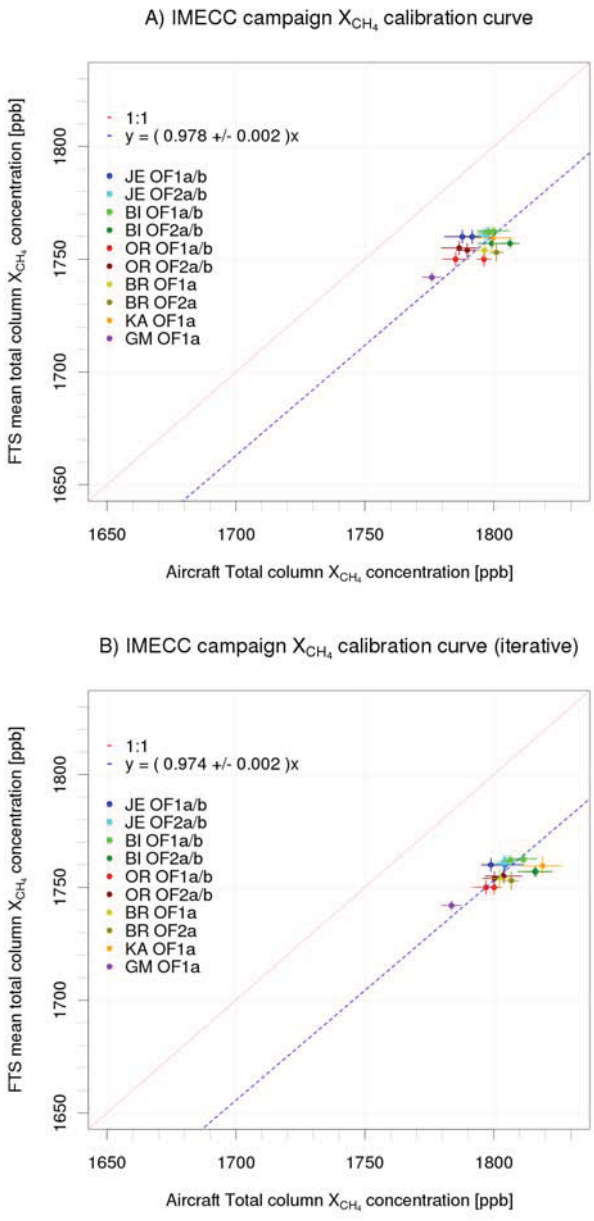

Figure 3.25: Calibration factor derived by the traditional method by Wunch et al. (2010) (A) and by an iterative calculation (B) for the IMECC campaign data.

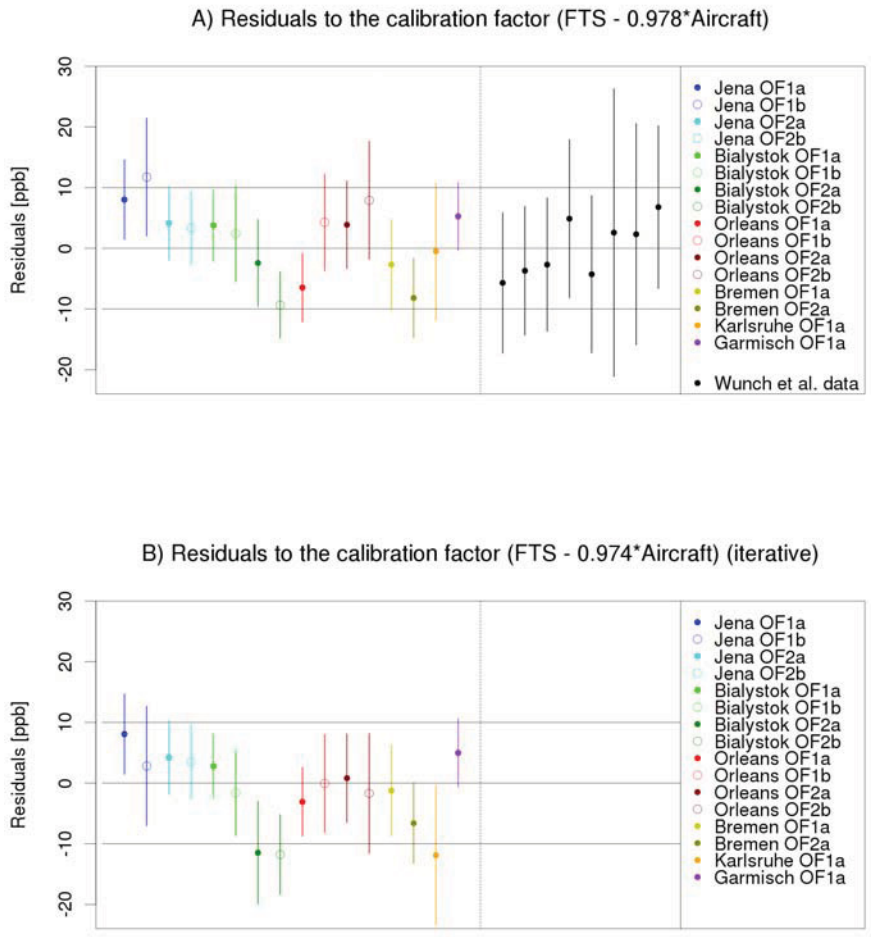

Figure 3.26: Residuals of the calibration factors derived by the traditional method by Wunch et al. (2010) for all data (A) and by an iterative calculation for IMECC data (B).

3.8 Conclusion

With the results of the IMECC aircraft campaign the earlier calibration factor from Wunch et al. (2010) can be confirmed. By adding the IMECC calibration points to the dataset, the uncertainty of the fit for the derivation of the calibration factor could be reduced by $\sim$68% (see Table 3.4). It seems to be most likely that this factor is a uniform calibration factor for the whole TCCON network. A sensitivity

Table 3.4: Results of the IMECC campaign

Calibration factor	**A-priori profile**	**Dataset**	**Value**	**Fit error (1σ)**	**Species uncertainty (2σ)**
$\psi_{standard\ ap}$	standard GFIT	IMECC	0.978	0.002	7ppb
$\psi_{aircraft\ ap}$	ext. aircraft	IMECC	0.978	0.002	7ppb
ψ_0	ext. aircraft	IMECC + Wunch et al.	0.978	0.001	3.5ppb
$\psi_{reduced}$	ext. aircraft	IMECC + Wunch et al.	0.979	0.001	3.5ppb
$\psi_{iterative}$	ext. aircraft	IMECC	0.974	0.002	7ppb
WMO recommendation					2ppb

study could show, that the vertical coverage of the aircraft data can affect the calibration factor. A uniform vertical coverage of the aircraft data, however, is not always possible. Besides that, the uncertainties of the stratospheric part lead to big error bars for the aircraft DMF and generate $\sim$85% of the total error budget. A better knowledge about the stratospheric distribution of CH_4 is needed to be able to reduce these errors and thus enhance the calibration procedure. The FTS

retrieval would also profit from this, since better a-priori profiles will definitely improve the GFIT results.

A possible solution could for the different vertical coverage of the aircraft data could be to use an iterative determination of a calibration factor. The results of a test of this approach show, that the calibration factor derived by the classical method was found to introduce a bias of $\sim 7\mathbf{ppb}$ for the FTS DMFs. This value corresponds to $\sim$200 $\%$ of the typical GFIT error for CH_4. Further investigations with more calibration points (e.g. IMECC + data from Wunch et al. (2010)) have to validate the results of this approach.

Appart from the iterative method, there are two options to eliminate this problem completely:

- The retrieval of a partial column from FTS spectral data, that has the same vertical coverage as the aircraft profile. This method is at the current state not possible since the GFIT software for the retrieval of FTS DMFs does not yet allow partial column retrieval. Besides that, partial column retrievals pose the risk of higher uncertainties than those for total column retrieval.

- Future calibration campaigns with balloon-based instruments like AirCore (Karion et al., 2010). This would allow to increase the vertical coverage drastically to an almost complete total column (0-30 $\mathbf{km}$) and thus solve the problem of stratospheric uncertainties.

Bibliography

Chen, H., Winderlich, J., Gerbig, C., Hoefer, A., Rella, C. W., Crosson, E. R., Van Pelt, A. D., Steinbach, J., Kolle, O., Beck, V., Daube, B. C., Gottlieb, E. W., Chow, V. Y., Santoni, G. W., and Wofsy, S. C.: High-accuracy continuous airborne measurements of greenhouse gases (CO_2 and CH_4) using the cavity ring-down spectroscopy (CRDS) technique, Atmospheric Measurement Techniques, 3, 375–386, doi:10.5194/amt-3-375-2010, 2010.

Frankenberg, C., Warneke, T., Butz, A., Aben, I., Hase, F., Spietz, P., and Brown, L. R.: Pressure broadening in the $2\nu3$ band of methane and its implication on atmospheric retrievals, Atmos. Chem. Phys, 8, 5061–5075, 2008.

Geibel, M. C., Gerbig, C., and Feist, D. G.: A new fully automated FTIR system for total column measurements of greenhouse gases, Atmospheric Measurement Techniques, 3, 1363–1375, doi:10.5194/amt-3-1363-2010, URL `http://www.atmos-meas-tech.net/3/1363/2010/`, 2010.

Gerbig, C., Schmitgen, S., Kley, D., Volz-Thomas, A., Dewey, K., and Haaks, D.: An improved fast-response vacuum-UV resonance fluorescence CO instrument, Journal Geophysical Research, 104, 1699–1704, 1999.

Gordon, I. E., Kassi, S., Campargue, A., and Toon, G. C.: First identification of

the electric quadrupole transitions of oxygen in the solar and laboratory spectra, Journal of Quantitative Spectroscopy and Radiative Transfer, 2010.

Jenouvrier, A., Daumont, L., Regalia-Jarlot, L., Tyuterev, V. G., Carleer, M., Vandaele, A. C., Mikhailenko, S., and Fally, S.: Fourier transform measurements of water vapor line parameters in the 4200-6600 cm-1 region, Journal of Quantitative Spectroscopy and Radiative Transfer, 105, 326 – 355, 2007.

Kalnay, E., Kanamitsu, M., Kistler, R., Collins, W., Deaven, D., Gandin, L., Iredell, M., Saha, S., White, G., Woollen, J., Zhu, Y., Leetmaa, A., Reynolds, R., Chelliah, M., Ebisuzaki, W., Higgins, W., Janowiak, J., Mo, K. C., Ropelewski, C., Wang, J., Jenne, R., and Joseph, D.: The NCEP/NCAR 40-Year Reanalysis Project, Bulletin of the American Meteorological Society, 77, 437–471, doi:10.1175/1520-0477(1996)077⟨0437:TNYRP⟩2.0.CO;2, URL http://journals.ametsoc.org/doi/abs/10.1175/1520-0477%281996%29077%3C0437%3ATNYRP%3E2.0.CO%3B2, 1996.

Karion, A., Sweeney, C., Tans, P., and Newberger, T.: AirCore: An Innovative Atmospheric Sampling System, Journal of Atmospheric and Oceanic Technology, 27, 1839–1853, doi:10.1175/2010JTECHA1448.1, URL http://journals.ametsoc.org/doi/abs/10.1175/2010JTECHA1448.1, 2010.

Keppel-Aleks, G., Toon, G. C., Wennberg, P. O., and Deutscher, N. M.: Reducing the impact of source brightness fluctuations on spectra obtained by Fourier-transform spectrometry, Appl. Opt., 46, 4774–4779, doi:10.1364/AO.46.004774, URL http://ao.osa.org/abstract.cfm?URI=ao-46-21-4774, 2007.

Luo, M., Cicerone, R. J., and Russell III, J. M.: Analysis of Halogen Occultation Experiment HF versus CH4 correlation plots: Chemistry and transport implications, J. Geophys. Res., 100, 13,927–13,937, doi:10.1029/95JD00621, 1995.

Messerschmidt, J., Geibel, M. C., Blumenstock, T., Chen, H., Deutscher, N. M., Engel, A., Feist, D. G., Gerbig, C., Gisi, M., Hase, F., Katrynski, K., Kolle, O., Lavrič, J. V., Notholt, J., Palm, M., Ramonet, M., Rettinger, M., Schmidt, M., Sussmann, R., Toon, G. C., Truong, F., Warneke, T., Wennberg, P. O., Wunch, D., and Xueref-Remy, I.: Calibration of TCCON column-averaged CO_2: the first aircraft campaign over European TCCON sites, Atmospheric Chemistry and Physics Discussions, 11, 14 541–14 582, doi:10.5194/acpd-11-14541-2011, URL `http://www.atmos-chem-phys-discuss.net/11/14541/2011/`, 2011.

Newman, S. M., Lane, I. C., Orr-Ewing, A., Newnham, D. A., and Ballard, J.: Integrated absorption intensity and Einstein coefficients for the O2 a 1 Delta g-X 3 Sigma g-(0, 0) transition: A comparison of cavity ringdown and high resolution Fourier transform spectroscopy with a long-path absorption cell, Journal of Chemical Physics, 110, 10 749–10 757, 1999.

Pscheidt, I.: Personal communication, information about results of the PROFFIT retival of Karlsuhe data, 2009.

Rodgers, C. D. and Connor, B. J.: Intercomparison of remote sounding instruments, J. Geophys. Res., 108, 4116–4229, doi:10.1029/2002JD002299, 2003.

Rothman, L., Gordon, I., Barbe, A., Benner, D., Bernath, P., Birk, M., Boudon, V., Brown, L., Campargue, A., Champion, J.-P., Chance, K., Coudert, L., Dana, V., Devi, V., Fally, S., Flaud, J.-M., Gamache, R., Goldman, A., Jacquemart, D., Kleiner, I., Lacome, N., Lafferty, W., Mandin, J.-Y.,

Massie, S., Mikhailenko, S., Miller, C., Moazzen-Ahmadi, N., Naumenko, O., Nikitin, A., Orphal, J., Perevalov, V., Perrin, A., Predoi-Cross, A., Rinsland, C., Rotger, M., Simeckova, M., Smith, M., Sung, K., Tashkun, S., Tennyson, J., Toth, R., Vandaele, A., and Auwera, J. V.: The HITRAN 2008 molecular spectroscopic database, Journal of Quantitative Spectroscopy and Radiative Transfer, 110, 533 – 572, doi:DOI:10.1016/j.jqsrt.2009.02.013, URL http://www.sciencedirect.com/science/article/B6TVR-4VPM5M4-2/2/464a427cb2670a9be660fe6e0e4d0272, 2009.

Toth, R.: Measurements of positions, strengths and self-broadened widths of H2O from 2900 to 8000cm-1:line strength analysis of the 2nd triad bands, Journal of Quantitative Spectroscopy and Radiative Transfer, 94, 51–107, 2005.

Toth, R. A., Brown, L. R., Miller, C. E., Malathy Devi, V., and Benner, D.: Spectroscopic database of CO2 line parameters: 4300–7000cm- 1, Journal of Quantitative Spectroscopy and Radiative Transfer, 109, 906–921, 2008.

Washenfelder, R. A., Wennberg, P. O., and Toon, G. C.: Tropospheric methane retrieved from ground-based near-IR solar absorption spectra, Geophys. Res. Lett., 30, 2226, doi:10.1029/2003GL017969, 2003.

Wunch, D.: Personal communication, information about different atm linelists and details about fitting procedure, 2010.

Wunch, D., Toon, G. C., Wennberg, P. O., Wofsy, S. C., Stephens, B. B., Fischer, M. L., Uchino, O., Abshire, J. B., Bernath, P., Biraud, S. C., Blavier, J.-F. L., Boone, C., Bowman, K. P., Browell, E. V., Campos, T., Connor, B. J., Daube, B. C., Deutscher, N. M., Diao, M., Elkins, J. W., Gerbig, C., Gottlieb, E., Griffith, D. W. T., Hurst, D. F., Jiménez, R., Keppel-Aleks, G.,

Kort, E. A., Macatangay, R., Machida, T., Matsueda, H., Moore, F., Morino, I., Park, S., Robinson, J., Roehl, C. M., Sawa, Y., Sherlock, V., Sweeney, C., Tanaka, T., and Zondlo, M. A.: Calibration of the Total Carbon Column Observing Network using aircraft profile data, Atmospheric Measurement Techniques, 3, 1351–1362, doi:10.5194/amt-3-1351-2010, URL `http://www.atmos-meas-tech.net/3/1351/2010/`, 2010.

Wunch, D., Toon, G. C., Blavier, J.-F. L., Washenfelder, R., Notholt, J., Connor, B. J., Griffith, D. W. T., Sherlock, V., and Wennberg, P. O.: The Total Carbon Column Observing Network (TCCON), 369, 2087–2112, doi:10.1098/rsta.2010.0240, 2011.

Yang, Z., Wennberg, P., Cageao, R., Pongetti, T., Toon, G., and Sander, S.: Ground-based photon path measurements from solar absorption spectra of the O2 A-band, Journal of Quantitative Spectroscopy and Radiative Transfer, 90, 309–321, 2005.

York, D., Evensen, N. M., Martínez, M. L., and Delgado, J. D. B.: Unified equations for the slope, intercept, and standard errors of the best straight line, American Journal of Physics, 72, 367–375, doi:10.1119/1.1632486, URL `http://link.aip.org/link/?AJP/72/367/1`, 2004.

Chapter 4

The Australia Campaign

4.1 Abstract

In this section the results of the measurement campaign of the Jena FTS system in Wollongong (AUS) are presented. Goal of the campaign was to perform a side by side intercomparison with the TCCON instrument of the University of Wollongong (UoW) and prove the system's transportability and functionality. The FTS system arrived early July 2010 after a five week transport. The duration of the campaign was 5 months. Spectral data were recorded simultaneously by the Jena FTS and the FTS of the UoW. On-site in-situ CO_2 measurements were taken at both sites to identify periods where measurements were affected by local sources.

The analysis of the total column measurements shows large scatter in the data of the Jena FTS. This is presumably caused by oscillations of the solar tracker that lead to differences between true and calculated airmass. For the intercomparison, the scatter could be removed by the calculation of daily median values. No prescreening of the Jena FTS data was performed and the data of both instruments were processed with different GFIT versions. Despite this, the resulting correlation shows that for the majority of the data both instruments agree within TCCON

requirements.

4.2 Introduction

After successfully taking part in the IMECC aircraft campaign the system was shipped to Australia for a measurement campaign. Goal of the campaign was to prove its transportability and functionality. Since the University of Wollongong (UoW) operates one of their FTIR instruments in Wollongong (Fraser et al., 2011), the campaign offered the rare opportunity to run two TCCON instruments side by side and to evaluate the comparability of their measurements.

The transport preparations in Jena took about 3 days. All exterior parts had to be removed, stored and secured inside the container for transport.

4.3 Journey and location

The system traveled $\sim$ 25000 $\mathbf{km}$ by truck, train and ship (see Fig. 4.1). During the transport it was loaded and unloaded several times with cranes and container spreaders.

After a five week journey, the system arrived at its temporal site at UoW Campus East, located 2.1 $\mathbf{km}$ north-east of the UoW FTIR system (see Fig. 4.2).

At this site, the measurement conditions were good. The solar tracker had a free field of view from short after sunrise till sunset. The system was connected to a nearby local power distribution board. However, pollen from close-by vegetation caused a slowly increasing contamination of the solar tracker mirrors at the end of the campaign. Another drawback was the unreliable and slow internet connection that did not allow real-time data transfer to Jena.

Figure 4.3 shows a one-year footprint for the total column measurements ex-

Figure 4.1: Route of the journey of the MPI-BGC FTIR system to Wollongong, Australia.

pected at Wollongong. The influence to the total column is quite large and mostly westerly orientated, including land and ocean contribution.

4.4 System functionality and stability

The system survived the journey in very good condition. After the connection to the local power supply was established, the system was set up. The check of the condition of the spectrometer showed, that it was severely misaligned due to the vibration and shocks during the transport. Once it was re-aligned, the FTS instrumental line shape (ILS) was determined (see Sec. 2.4.1). The derived ILS (see Fig. 4.4) was very symmetrical and as good as before the transport. However, the achieved modulation efficiency (see Fig. 4.5) was a little worse than in February 2010, but still within TCCON recommendations (95 %). In contrast, the corresponding phase error was even better than it had been before.

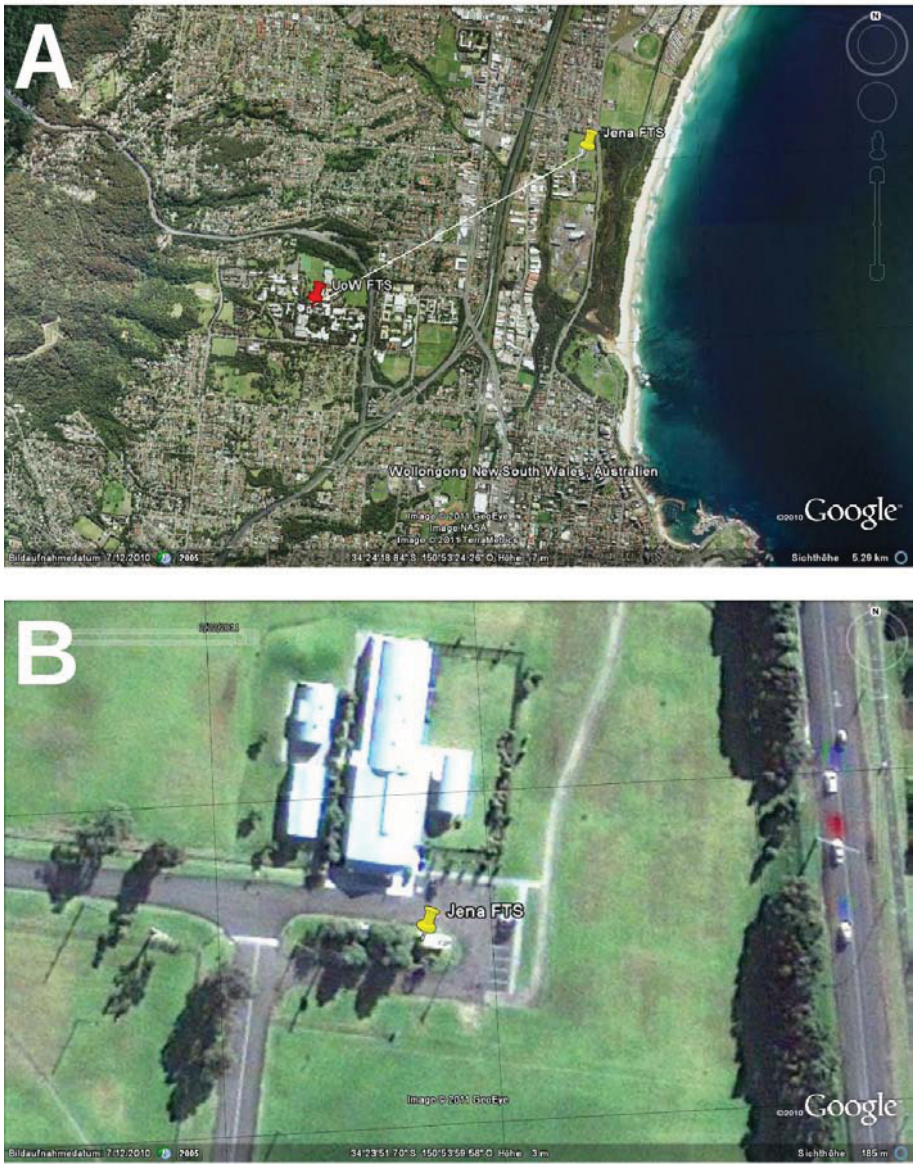

Figure 4.2: A) Satellite picture of Wollongong, Australia, showing the location of the Jena FTS and the FTS of the University of Wollongong (UoW). The distance between the two FTS is approximately 2.1 $\mathbf{km}$. B) Satellite picture of the Jena FTS system at its location on Campus East in Wollongong, Australia. The picture was taken shortly after the setup of the instrument on June 12th 2010 by GeoEye.

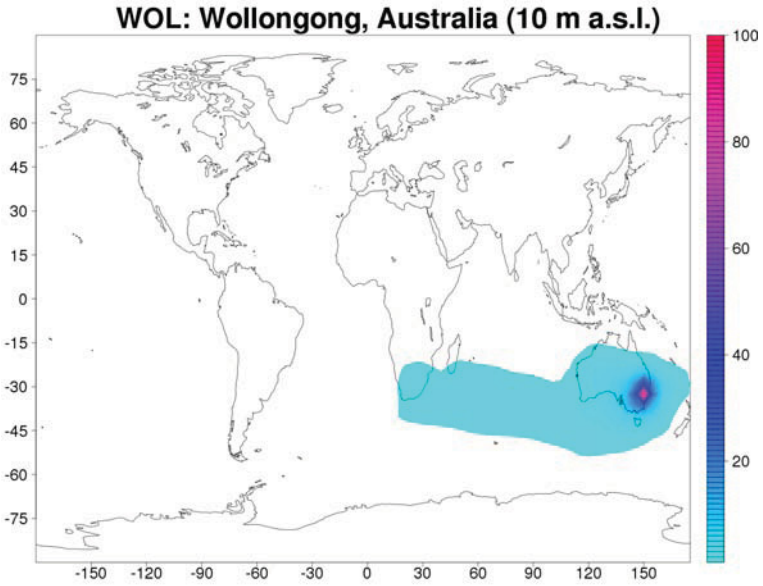

Figure 4.3: Footprint analysis for a total-column instrument on Ascension Island. The colored values represent the relative contribution to the total column for different surface regions in arbitrary units that have been normalized to 100 at the peak value. The footprint was produced using the TM3 adjoint by Rödenbeck (2005) at a horizontal resolution of $5^\circ \times 3.75^\circ$ (fine grid). Individual runs for each month of 2006 were integrated to provide this full-year footprint.

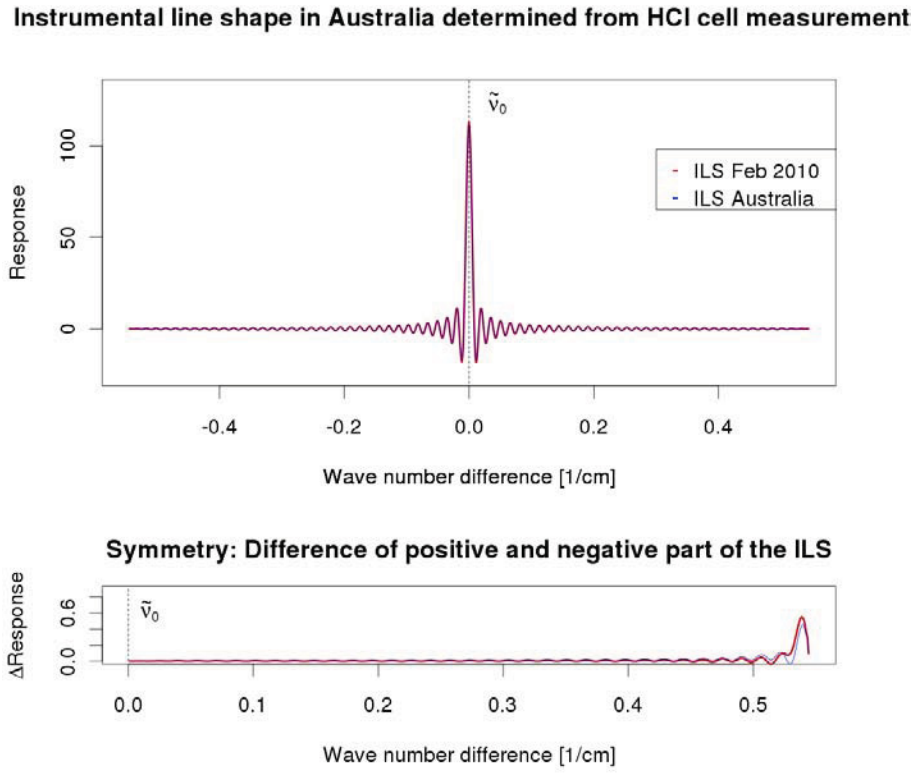

Figure 4.4: ILS of the instrument after alignment. The ILS is very symmetrical and as good as it was in February 2010.

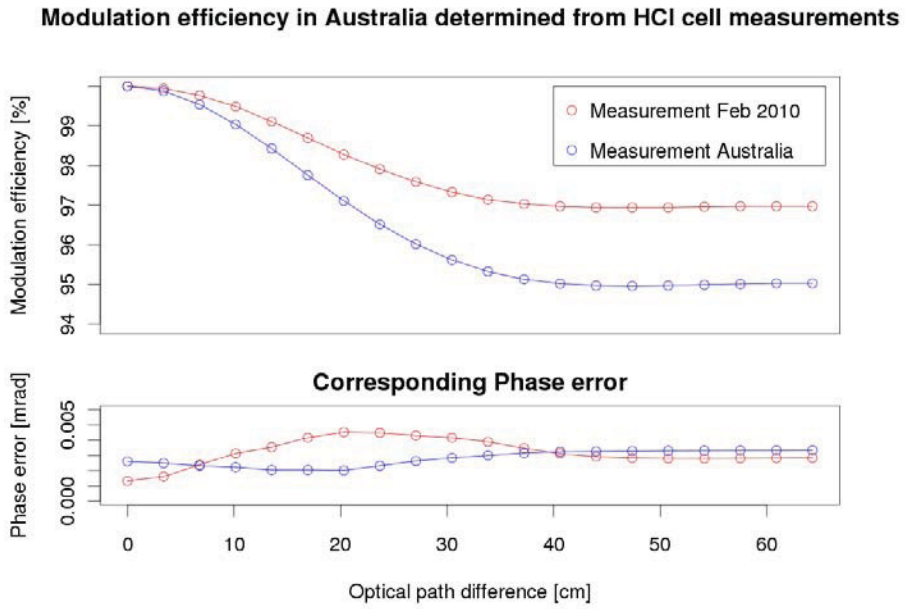

Figure 4.5: Modulation efficiency and corresponding phase error of the instrument after alignment. The modulation efficiency is not as good as in January but still within TCCON specifications. The phase error is very small.

In summary, the FTS could be well aligned again and was ready for measurements. The temperature inside the container was stabilized to +/- 1 $^{\circ}\mathrm{C}$ (see Fig. 4.6). The temperature inside the FTS typically varied only by +/- 0.1 $^{\circ}\mathrm{C}$. Regular variations during daytime are caused by the illumination of internal parts of the FTS by the incoming sunlight.

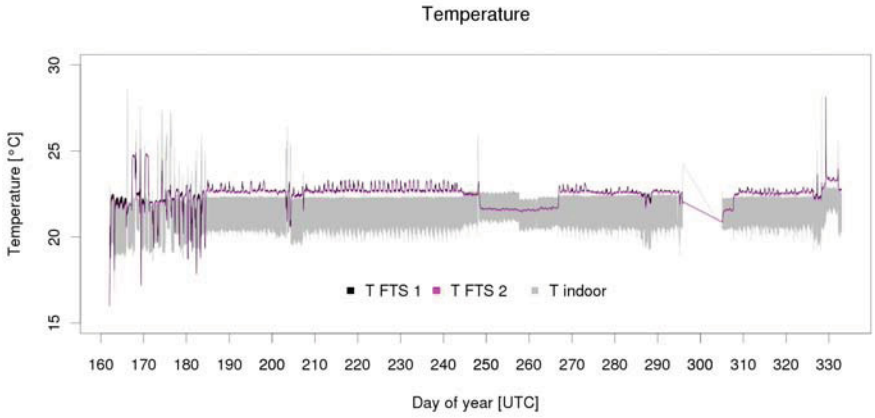

Figure 4.6: Time series of the temperature inside the container and inside the FTS.

Figure 4.7 shows a time series of pressure inside the instrument that was monitored with the internal FTS pressure sensor. The FTS was evacuated automatically before sunrise. The leak rate increased during the campaign from 0.1 $\mathbf{mbar/h}$ in the beginning to 0.3 $\mathbf{mbar/h}$ at the end. This increase was caused by a small leak that could be identified later at the handle of one of the lids of the FTS. However, the FTS was always well evacuated and so spectral contamination by water vapor was avoided.

During the campaign, the system had to manage several unforeseen events. Around September 5th (day 248), a strong storm front with wind speeds over 30 $\mathbf{m/s}$ (120 $\mathbf{km/h}$) hit the east coast (see Fig. 4.8). This storm caused a power failure that was too long to be bridged by the internal UPS of the system. The

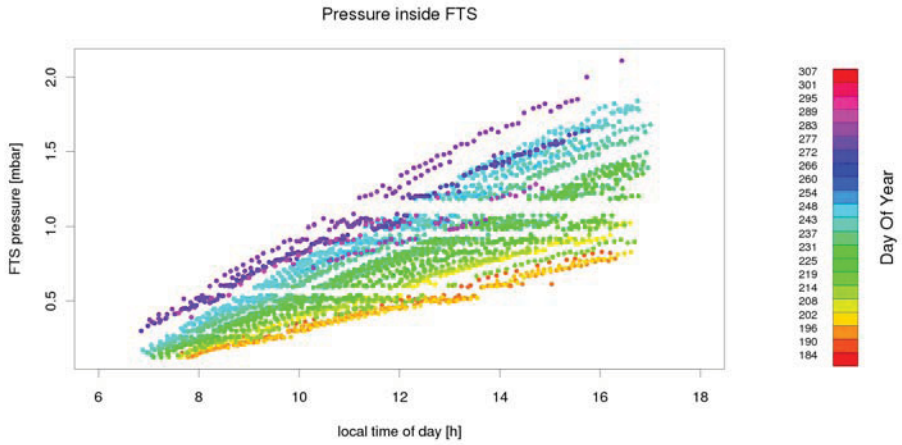

Figure 4.7: Time series of the FTS internal pressure. The color stands for the day of year.

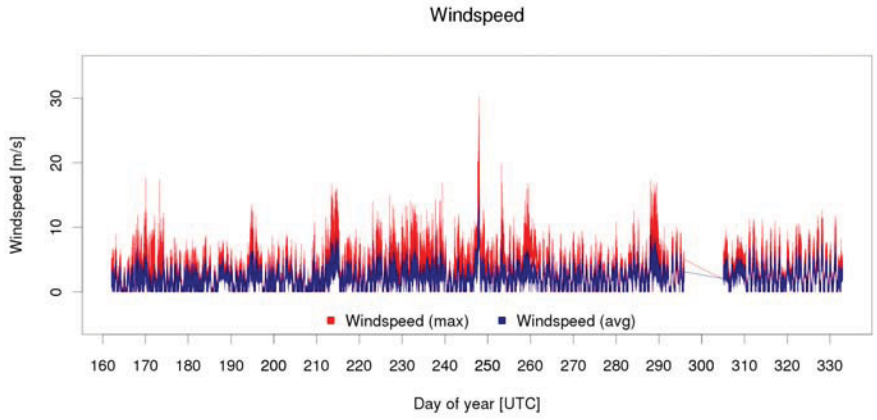

Figure 4.8: Time series of the wind speed recorded by the weather station. Around day 248, a storm front came though causing wind speeds of over 30 $\mathbf{m/s}$.

container was shut down automatically and was restarted by the PLC after the power came back. The dome protected the solar tracker and the system survived the storm without damage.

On October 23rd (day 296), the system was disconnected from electricity by the local power company for several days for a major maintenance of the power distribution board. After re-connection of the system to the power distribution, the system did not start up. This was caused by a mix-up of the neutral line and one of the 3 phases. Possible sever damage to the system was prevented by the phase control that had been retrofitted to the system shortly before the campaign. It monitors the phase sequence and the voltage of all 3 phases. Once the problem was found and fixed, the system started up and resumed the automated measurements.

Figure 4.9 shows the record of the two digital pressure sensors of the weather station. Both sensors agree perfectly for the whole data set. A requirement for exchange and re-calculation as described in Chapter 2.3.4 (see Fig. 2.7) is not yet indicated.

An overview of the full dataset of the weather station can be found in Figures H.1 to H.5 in Appendix H.

4.5 Measurements

Within the Australia campaign nearly 2800 solar spectra were recorded (see Table 4.1). Due to the bad internet connection the huge amount of data could not be transfered to Germany for analysis. The data was stored locally and transfered to the MPI-BGC at the end of the campaign using tapes. Figure 4.10 illustrates the amount of performed measurements over the progression of the campaign. The maximum number of measurements on a single day was 78 and on an av-

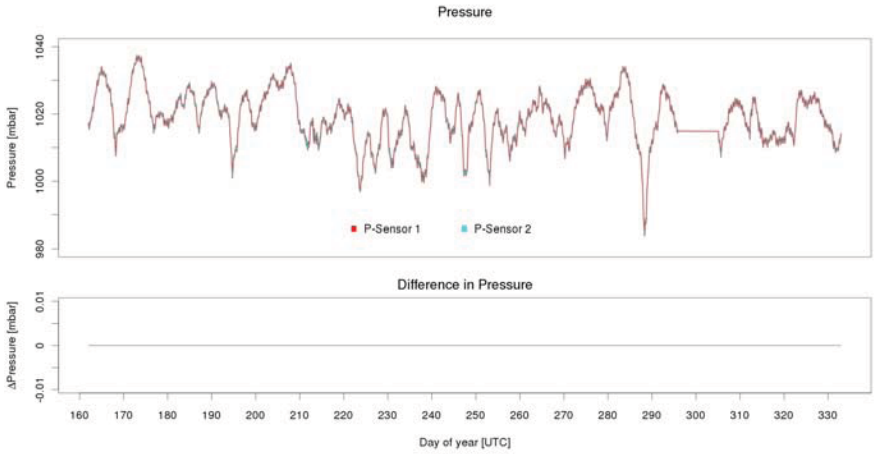

Figure 4.9: Time series of the air pressure recorded by the two digital pressure sensors of the weather station. The lower graph shows the difference between both sensors. There is no drift or offset between both pressure sensors.

Table 4.1: total column measurement statistics of the Australia campaign.

Total number of measurements	2768
Maximum number of measurements on a single day	78
Average number of measurements per measurement day	38.4
Average number of measurements per campaign day	22.3

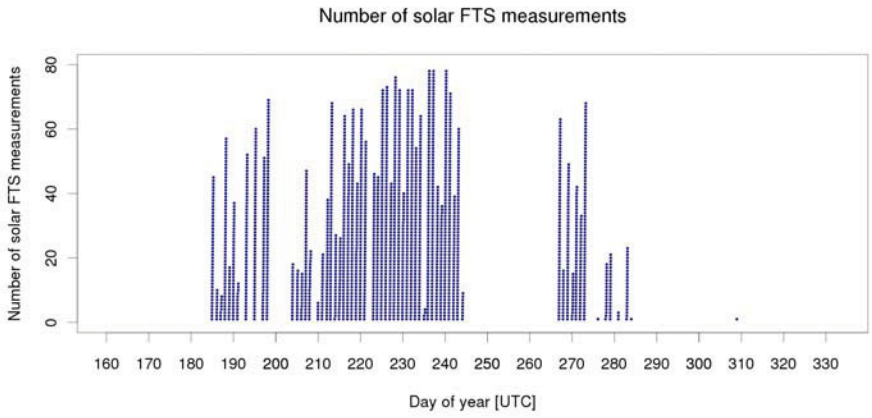

Figure 4.10: Time series of the number of total column measurements of the Australia campaign.

erage measurement day nearly 40 spectra could be recorded. The limiting factor for total column measurements is obviously the cloud coverage. An indicator for this is the global radiation that was measured by the pyranometer of the weather station (see Fig. 4.11). On a day with clear sky the profile of the recorded global radiation has a perfect Gaussian shape (days 225 and 226 in Fig. 4.11), whereas this profile is disturbed with increasing cloud coverage (days 223, 224 and 227 in Fig. 4.11). Hence, the number of measurements is smaller. On overcast days, no spectra could be recorded (see day 222 in Fig. 4.11).

Starting in the middle of September (around day 250), pollen from close-by vegetation caused a slowly increasing contamination of the solar tracker mirrors (see Fig.4.12). This lead to a decrease in radiation intensity and restrained the system in the end to perform measurements.

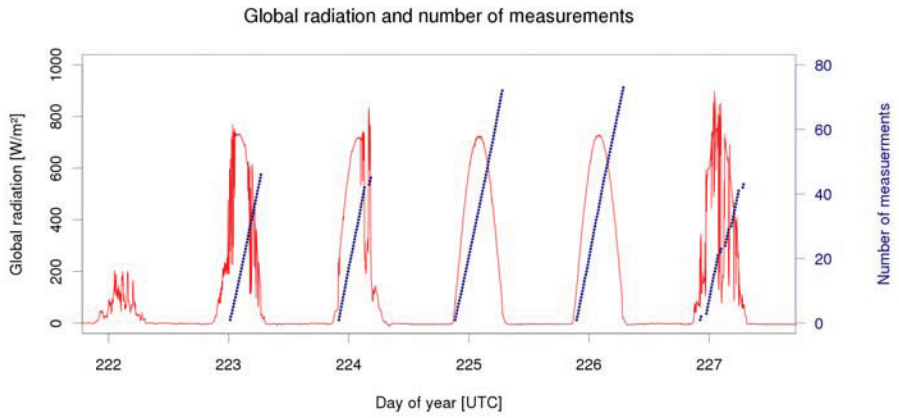

Figure 4.11: Illustration of the correlation between global radiation and number of total column measurements for a 6 day period (2010-08-10 till 2010-08-15).

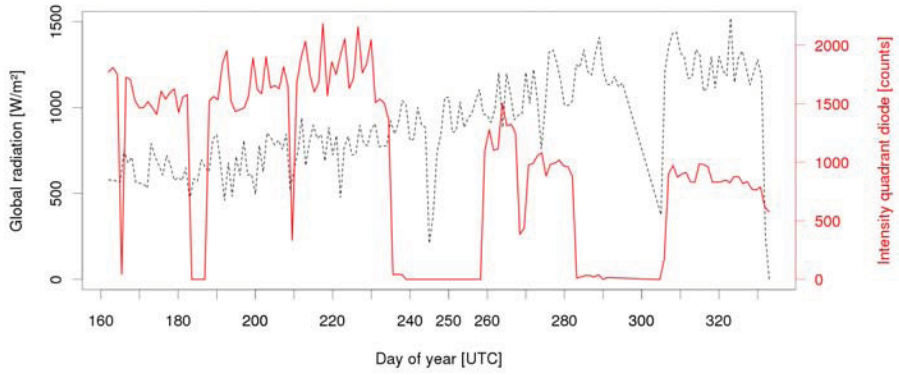

Figure 4.12: Illustration of the slowly increasing contamination of the solar tracker mirrors: Global radiation measured by the pyranometer (black dashed line) and radiation intensity at the quadrant diode of the solar tracker (red full line).

4.5.1 In-situ CO_2 measurements

The Jena FTS could not be located directly next to the Wollongong FTS. The linear distance between the two sites was $\sim$2.1 $\mathbf{km}$ (see Fig. 4.2). This posed the risk of different local sources that have different influences the total column measurements. To help to identify those possible local influences, the Jena FTS system was additionally equipped with an in-situ CO_2 sensor (Vaisala CarboCap). The time series of the in-situ CO_2 measurements is shown in Fig. 4.13. The sensor

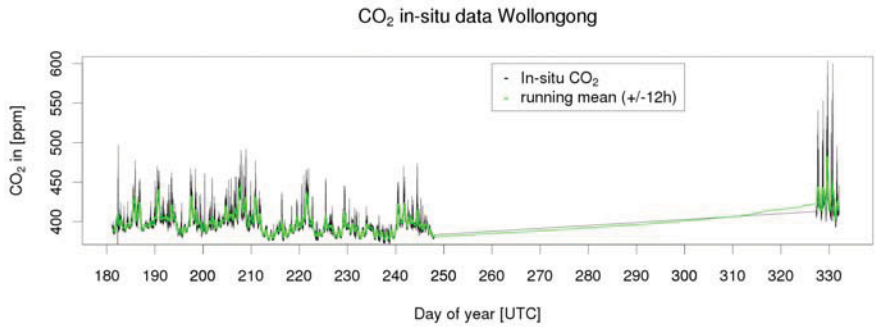

Figure 4.13: Time series of the in-situ CO_2 measurements at the Jena FTS site taken with a Vaisala CarboCap.

had to be integrated to the data acquisition of the existing system. Unfortunately, this upgrade to the system could not be tested for extreme events such as power outages. After the first power failure the data acquisition of the CO_2 sensor did not re-start properly causing a large gap in the in-situ CO_2 record. However, the acquired data of this sensor can help in the intercomparison of the FTS data to identify local events that might cause changes in the total column.

At the site of the Wollongong FTS, in-situ CO_2 measurements were performed with an in-situ FTIR trace gas analyzer “Ooofti“ similar to the one described in Deutscher (2009). The data, however, are not yet available, but it has been agreed with the UoW that the data will be provided for comparison in the near future.

4.5.2 FTIR measurements

For the Australia campaign, the acquisition of the data was changed to direct instrument communication. This way, the interferograms were delivered in "slices" (see Chapter. 3.4.1) through the web server of the instruments. For the spectral retrieval, these slices had to be pre-processed with the slice-ipp software introduced in Chapter. 3.4.1. The resulting spectra were processed with the GFIT software (Release 20091107). Possible cloud-affected measurements are not yet filtered. For further analysis, a quality control as pre-processing step has to be established to identify those spectra and remove them from the dataset.

During the campaign the tracker showed an usual high pointing error causing an oscillation in the order of +/-20% of the diameter of projection of sun on the 1st aperture. This oscillation was observed at a frequency of $\sim$1-2 $\mathbf{Hz}$. The problem occurred first after the setup of the tracker in Australia and could not be solved on-site. Reason for the inaccurate pointing of the tracker is the slow regulator circuit of the tracker's motors that causes a low-frequent oscillation. Those pointing errors cause differences between the true airmass (the length of the path that the sunlight travels through the atmosphere) and the airmass calculated for the retrieval.

Figure 4.14 shows a four day running mean of the in-situ and total column CO_2 measurements. Both measurements show good agreement: The variation of CO_2 in the boundary layer of $\sim$10 $\mathbf{ppm}$ corresponds to variations of $\sim$1 $\mathbf{ppm}$ in the total column. Assuming the variations in in-situ CO_2 are limited to the planetary boundary layer (PBL), this ratio of 10/1 relates to an average PBL height of $\sim$1 $\mathbf{km}$. Figure 4.15 shows the mean diurnal variation of in-situ and total column CO_2. The in-situ measurements show a distinct diurnal cycle with an average nocturnal build-up of $\sim$8 $\mathbf{ppm}$. Given typical stable boundary layer heights of 100 to 300 $\mathbf{m}$ and a scale height of 8 $\mathbf{km}$, this corresponds to variations of 0.1 to

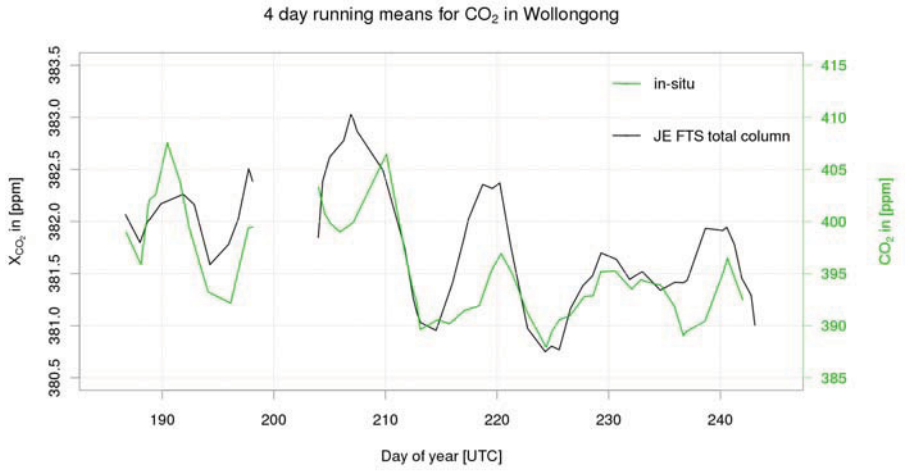

Figure 4.14: Four day running means of in-situ and total column CO_2 measurements. The in-situ data are limited to the time where FTS measurements were performed.

0.3 $\mathbf{ppm}$ in the total column. However, the observed diurnal variations in the total column measurements show a large decrease of $\sim$2 $\mathbf{ppm}$ in the morning hours and a symmetric increase in the evening. This symmetry indicates a problem at high solar zenith angles, respectively high airmass. It is probably caused by the pointing error of the solar tracker that has a higher impact at higher solar zenith angles. As a result, the expected variations in the total column due to the nocturnal build-up of CO_2 are hidden beneath those airmass effects and can not be observed at this stage of data processing.

Figures 4.16 and 4.17 show the results for X_{CO_2} and X_{CH_4} in comparison to results of the Wollongong FTS. Unfortunately, the data of the data of the Wollongong FTS are not processed with the same GFIT version what might affect the comparability. Further investigation will require uniform data processing.

The results illustrate that the data on average are roughly in agreement. However, the Jena FTS data have significantly more scatter which is caused by the

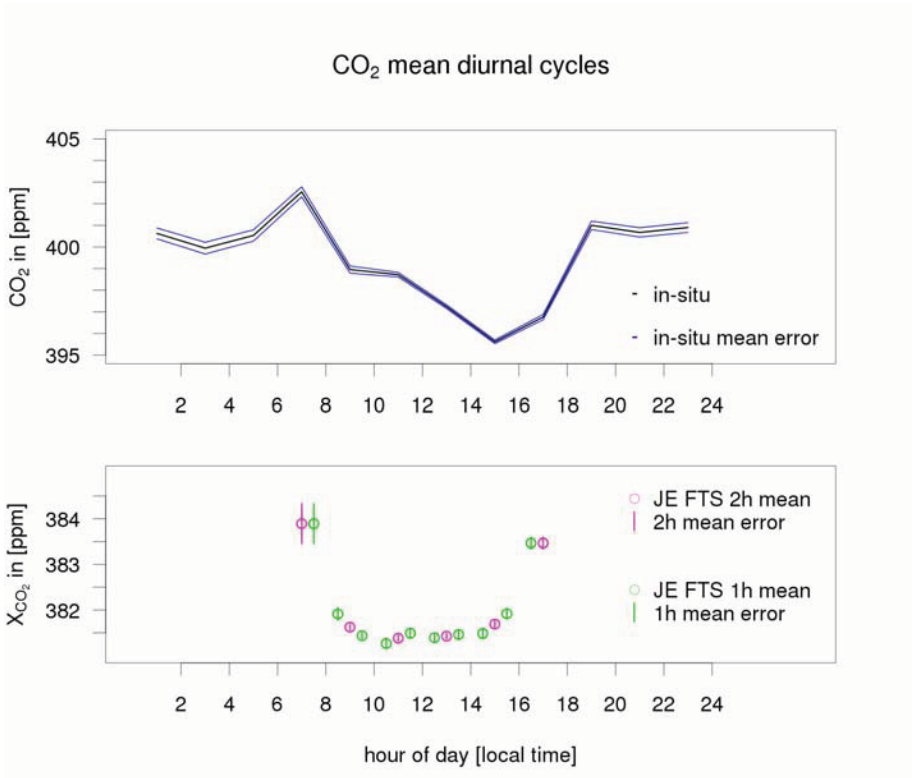

Figure 4.15: Mean diurnal variation of in-situ and total column CO_2 measurements. The upper panel shows the mean diurnal cycle for the in-situ measurements, averaged over 2h intervals. The lower panel shows the mean diurnal variation for the total column measurements, averaged over 2h and 1h intervals.

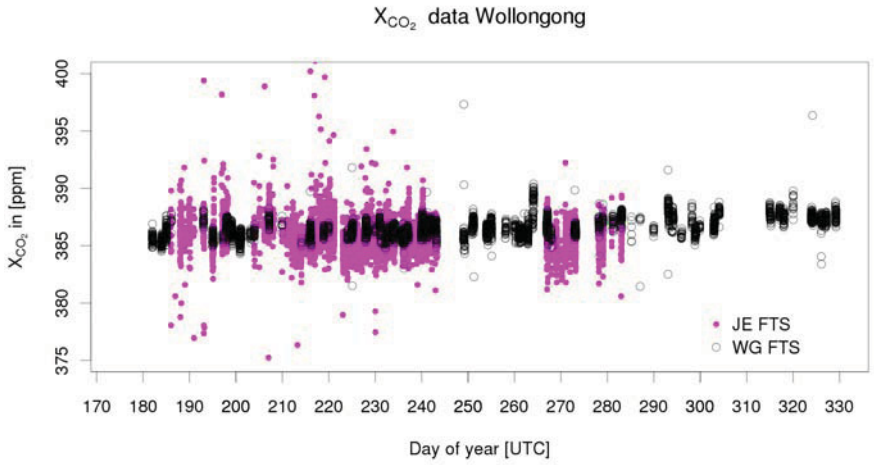

Figure 4.16: Full time series of X_{CO_2} of the Jena FTS (JE, pink) and Wollongong FTS (WG, black) taken at Wollongong (AUS). The data of the JE instrument are not filtered.

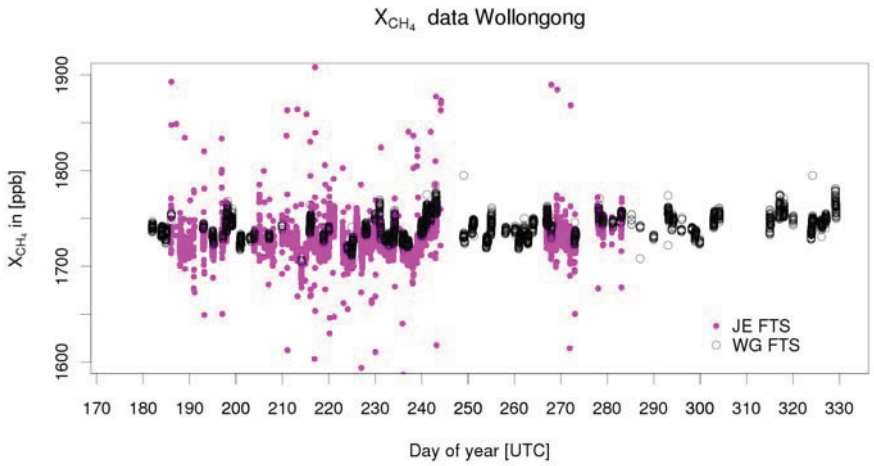

Figure 4.17: Same as Figure 4.16 but for X_{CH_4}.

pointing error of the solar tracker. Since the oscillation of the tracker is slow and symmetrical, it is highly likely that the errors in the airmass are symmetrical, too. This causes also a rather symmetrical scatter of the data points (see Fig. 4.16 and 4.17).

4.5.3 Intercomparison

To compensate the scatter of the Jena FTS, the daily median values were calculated for further intercomparison of the two FTS systems. The result show a good agreement between the Wollongong and the Jena FTS (see Fig. 4.18 and 4.19).

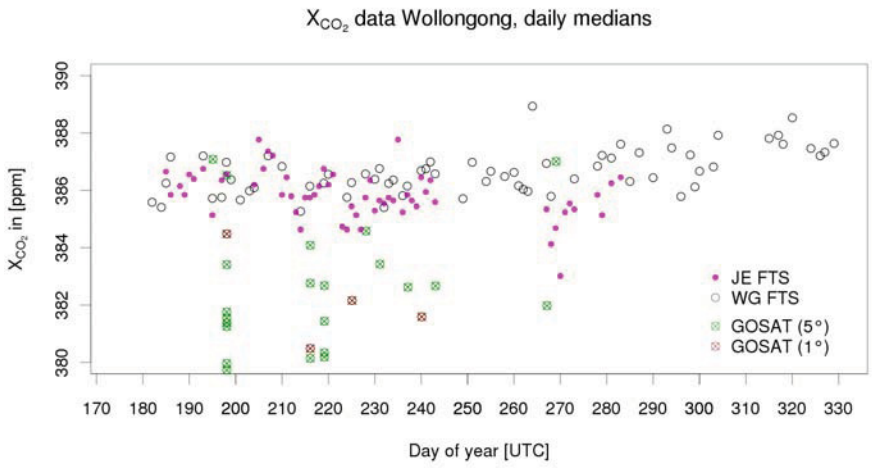

Figure 4.18: Full time series of X_{CO_2} of daily medians of the Jena FTS and UoW FTS. In addition results of the GOSAT retrievals within +/- 5 ° and +/- 1 ° distance in latitude/longitude.

For a better intercomparison of the two FTS systems, a correlation plot was made for the results for X_{CO_2} and X_{CH_4} (see Fig. 4.20). Although the data of the two FTS were processed with different GFIT versions and the data of the Jena FTS are not yet quality-screened, the agreement is quite good. For X_{CO_2} the standard

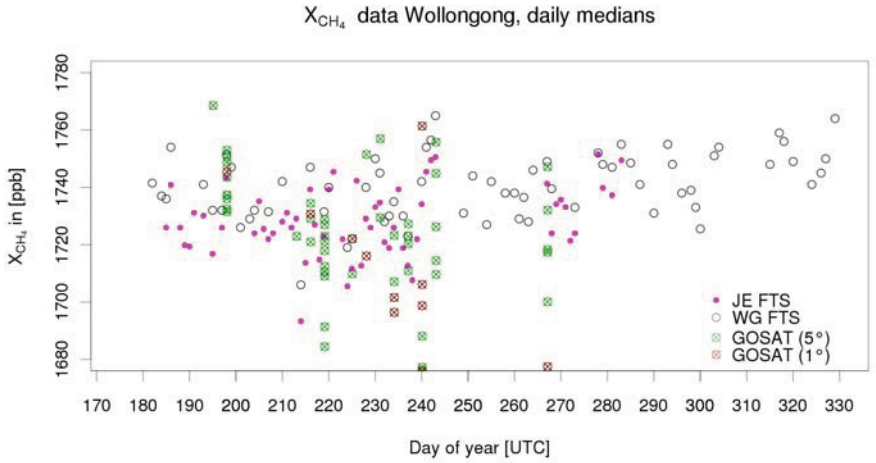

Figure 4.19: Same as Figure 4.18 but for X_{CH_4}.

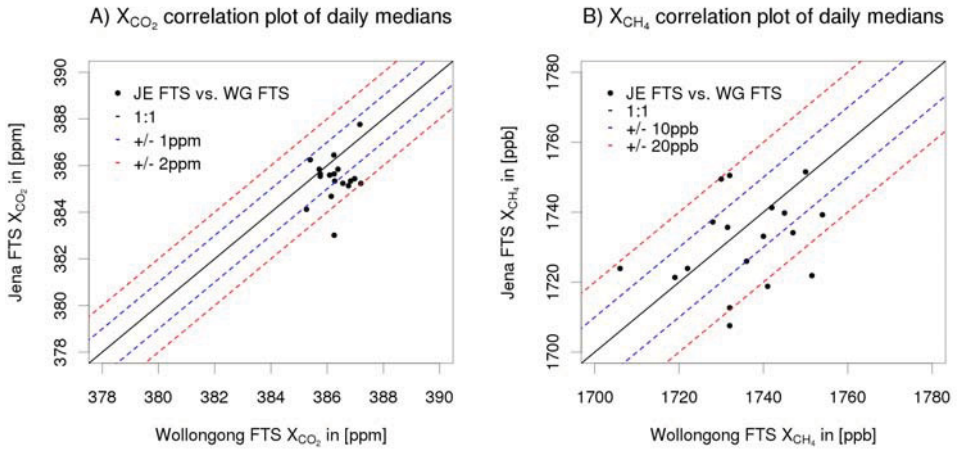

Figure 4.20: A) Correlation plot for the daily medians of X_{CO_2}. B) Correlation plot for the daily medians of X_{CH_4}.

deviation of the difference of both instruments is 0.27% (1.07 **ppm**) and so very close to the TCCON precision requirement of 0.25% (0.97 **ppm**). The offset between both instruments (JE FTS minus WG FTS) is ∼-0.9 **ppm**.

For CH_4 the standard deviation of the difference of both instruments is 0.99% (17.2 **ppb**). The offset is very small (∼-5 **ppb**) Previous intercomparisons of two FTS systems showed, that for X_{CO_2} a precision of 0.1 % (∼0.4 **ppm**) can be reached for two FTS directly next to each other (Messerschmidt et al., 2010).

However, to be able to achieve this, both instruments have to be "ghost corrected". Those ghost are artificial spectral lines caused by a periodic mis-sampling of the internal laser of the FTS and can so cause over- respectively underestimations in X_{CO_2} in the order of 1-2 **ppm** (Messerschmidt et al., 2010). For uncorrected FTS, a precision of 0.44 % (1.7 **ppm**) was reached (Messerschmidt et al., 2010). During the Australia campaign, only the Wollongong FTS was corrected for ghosts. Given the fact that different software versions were used for data processing and the Jena instrument was not corrected for ghosts, the preliminary results of the X_{CO_2} intercomparison for precision and offset lie well within expectations.

The main purpose of TCCON instruments is the validation and calibration of satellite-based measurements. To illustrate the necessity of this, the results of the GOSAT satellite retrieval for X_{CO_2} and X_{CH_4} were added to the dataset (see Fig. 4.18 and 4.19). At the current state of GOSAT retrieval of X_{CO_2} an offset of ∼9 **ppm** was observed between other TCCON FTS and GOSAT (Marshall (2011)). The results of this preliminary intercomparison show an offset of 5 +/- 2 **ppm** which is roughly in agreement with the previous findings. The X_{CH_4} data show a good agreement between the FTS and the GOSAT results. In general, the agreement of the two FTS systems is much better than the agreement between the GOSAT results and those from the FTS. This illustrates the potential of utilizing

ground-based FTS measurements - like those performed by TCCON - for satellite validation.

4.6 Conclusion

Within the Australia campaign the Jena FTS proved its reliability. It survived two power failures and wind speeds of over 30 $\mathbf{m/s}$ without damage. The spectrometer was severely misaligned after transport but could be re-aligned to TCCON standards. A time series of spectral data could be acquired, containing nearly 2800 measurements. The calculation of the mean diurnal variation of total column CO_2 revealed problems at high solar zenith angles that are probably caused by pointing errors of the solar tracker that lead to differences between true and calculated airmass. This needs to be further investigated and corrected to be able to investigate the contribution of the nocturnal build-up of boundary layer CO_2 to the total column.

The further data analysis showed a large scatter in the data of the Jena FTS that is also caused by the pointing error of the tracker. For the intercomparison, the scatter could be compensated by the calculation of daily median values. No prescreening of the Jena FTS data was performed and the data of both instruments were processed with different GFIT versions. Despite this, the resulting standard deviation of 0.27% for CO_2 shows that both instruments already agree with each other nearly within TCCON precision requirements. The results for X_{CO_2} also confirm results of earlier intercomparisons for FTS.

For next steps of the analysis, a quality control of the data of the Jena FTS has to be established. Besides that, the scatter of the data needs to be reduced. A possible solution for this problem might be the filtering of the low-frequency oscillation of the solar tracker in the interferograms. For this, the ipp-software needs

to be modified. Furthermore, a uniform data processing with the same GFIT version for the data of both FTS is indispensable, since this eliminates offsets created by unequal spectroscopy. A look at the in-situ CO_2 measurements of the Wollongong FTS site (the data were not yet available) in comparison to those made at the Jena FTS site might help to identify differences in X_{CO_2} caused by local sources. Besides that, a determination and correction of the ghosts of the Jena FTS has to be made. For the long-term operation of the system, the experience of this campaign shows, that it is crucial to keep the solar tracker mirrors clean. To identify possible contamination of the solar tracker mirrors, the intensity of the quadrant diode has to be checked and - if necessary - a cleaning of the mirrors has to be performed.

Bibliography

Deutscher, N. M.: Investigating greenhouse gases in Australia using atmospheric measurements with fourier transform spectrometry and atmospheric modeling, Ph.D. thesis, University of Wollongong, School of Chemistry, Australia, URL http://ro.uow.edu.au/theses/3112/, 2009.

Fraser, A., Chan Miller, C., Palmer, P. I., Deutscher, N. M., Jones, N. B., and Griffith, D. W. T.: The Australian methane budget: interpreting surface and train-borne measurements using a chemistry transport model, J. Geophys. Res., URL http://www.geos.ed.ac.uk/research/eochem/pubs/fraser_wetlands_agu_submit_figs.pdf, submitted, 2011.

Marshall, J.: Personal communication, information about the current status of GOSAT retrieval., 2011.

Messerschmidt, J., Macatangay, R., Nothold, J., Petri, C., Warneke, T., and Weinzierl, C.: Side by side measurements of CO2 by ground-based Fourier transform spectrometry (FTS), Tellus B, 62, 749–758, doi:10.1111/j.1600-0889.2010.00491.x, URL http://dx.doi.org/10.1111/j.1600-0889.2010.00491.x, 2010.

Rödenbeck, C.: Estimating CO_2 sources and sinks from atmospheric mixing ratio measurements using a global inversion of atmospheric transport, Tech.

Rep. 6, Max Planck Institute for Biogeochemistry, Jena, Germany, URL `http://www.bgc-jena.mpg.de/mpg/websiteBiogeochemie/Publikationen/Technical_Reports/tech_report6.pdf`, 2005.

Chapter 5

Summary and outlook

This work described the development of the MPI-BGC FTIR system in three parts: design and setup, calibration, and testing.

Chapter 2 described the principal components and the design concept of the system. The main design goals were reliability and low maintenance effort to facilitate operation at remote sites. This was realized through the interaction of independent subsystems that were kept as simple as possible. Critical components are redundant as much as possible.

The instrumental line shape of the FTIR was determined from HCl cell measurements. During a period of six months this ILS changed only slightly. From these results one can expect that – once aligned – the instrument will be very stable over long time periods.

During the installation phase at Jena, Germany, the instrument measured column-averaged X_{CO_2}, X_{CO} and X_{CH_4}. Compared to ground-based in-situ CO_2 VMR measurements, the FTIR total column X_{CO_2} showed an expected offset in the morning which mostly disappeared with the breakup of the nighttime planetary boundary layer. This effect demonstrated the reduced sensitivity of X_{CO_2} measurements to mixing processes in the planetary boundary layer and confirms results of model

simulations. Otherwise, the X_{CO_2} measurements show a distinct diurnal cycle. A part of seasonal cycle measured over Jena during the installation phase corresponded to TM3 simulation results that were extrapolated to 2009 values.

Chapter 3 introduced the results of the IMECC aircraft campaign. For CH_4 the earlier calibration factor from Wunch et al. (2010) can be confirmed. By adding the IMECC calibration points to the dataset, the uncertainty in the derivation of the calibration factor could be reduced by $\sim 68\%$. The assumption of a uniform calibration factor for the whole TCCON network could be verified.

A sensitivity study could shows, that the vertical coverage of the aircraft data affects the calibration factor. An iterative determination of a calibration factor is a possible solution to that problem. A test of this approach showed, that the calibration factor derived by the classical method introduced a $\sim 7\mathbf{ppb}$ offset for the FTS DMFs. Further investigation will assess, whether a generalization of this approach for other species such as CO_2 is suitable.

In Chapter 4 the results of a measurement campaign in Wollongong, Australia, were presented. Within that campaign the Jena FTS proved its reliability. The spectrometer was severely misaligned after transport but could be re-aligned to TCCON standards. A time series of spectral data could be acquired, containing nearly 2800 measurements. Compared to measurements from a similar instrument of the University of Wollongong (UoW), the data analysis showed a larger scatter in the data of the Jena FTS. This is caused by oscillations of the solar tracker that lead to differences between true and calculated airmass. For the intercomparison, the scatter could be annihilated by the calculation of daily median values. At the current state of the analysis, no quality control of the Jena FTS data was performed and the data of both instruments were processed with different GFIT versions. Despite this, the resulting correlation shows that for the majority of the data both instruments agree within TCCON requirements.

For further analysis, a quality control of the data of the Jena FTS has to be established. Besides that, the scatter of the data has to be reduced. A possible solution for this problem might be the filtering of the low-frequency oscillation of the solar tracker in the interferograms. For this, the IPP software needs to be modified. Furthermore, a uniform data processing with the same GFIT version for the data of both FTS is indispensable, since this eliminates offsets created by unequal spectroscopy.

Once the pointing problems of the Solar Tracker are solved, respectively their effects are compensated and other minor damages are repaired, the system is ready to be set up at its final destination Ascension Island. There it will be able to contribute to TCCON and to serve as a validation source for current and upcoming satellite missions. However, the data processing and pre-screening is to be improved to maximize the quality of the output products. For the long-term operation of the system, the experience of this campaign shows, that it is crucial to keep the solar tracker mirrors clean. To identify possible contamination of the solar tracker mirrors, the intensity of the quadrant diode has to be checked and - if necessary - a cleaning of the mirrors has to be performed.

Acknowledgements

I would like to thank several people for their contribution to this work:

- Dietrich Feist, Christoph Gerbig, Martin Heimann, and Wolfgang Weigand.
- Christian Rödenbeck for the TM3 data and Dhanyalekshmi Pillai for the WRF-VPRM simulations.
- The members of the central facilities of the MPI BGC: Reimo Leppert, Jörg Reith, Bernd Schlöffl, Rene Schwalbe, Frank Voigt.
- Gregor Surawicz from Bruker Optics for the technical support.
- All members of the TCCON, especially Frank Hase, Janina Messerschmidt,and Debra Wunch for the fruitful colaboration.
- The members of the IMECC aircraft campaign: Olaf Kolle, Martin Hertel, Stephan Baum, Huilin Chen Justus Notholt, Mathias Palm, Thorsten Warneke, Katinka Petersen, Benjamin Sampson, Christof Petri, Thomas Blumenstock, Frank Hase, Ieda Pscheidt, Markus Rettinger, Ralf Sussmann, Francois Truong, Irène Xueref-Remy, Krzysztof Katrynski, Rolf Maser, Harald Franke, Christoph Klaus, Dieter Schell, Svend Engemann.
- The Wollongong FTIR group, especially Nicholas Deuscher, David Griffith, Nicholas Jones, Graham Kettlewell, Ronald Macatangay, and Martin Riggenbach for the support during the Australia campaign.

• Max Planck Society for funding the FTIR instrument and the container.

Bibliography

Bovensmann, H., Burrows, J. P., Buchwitz, M., Frerick, J., Noël, S., Rozanov, V. V., Chance, K. V., and Goede, A. P. H.: SCIAMACHY: Mission Objectives and Measurement Modes, Journal of the Atmospheric Sciences, 56, 127–150, doi:10.1175/1520-0469(1999)056⟨0127:SMOAMM⟩2.0.CO;2, URL http://journals.ametsoc.org/doi/abs/10.1175/1520-0469%281999%29056%3C0127%3ASMOAMM%3E2.0.CO%3B2, 1999.

Bréon, F.-M. and Ciais, P.: Spaceborne remote sensing of greenhouse gas concentrations, Comptes Rendus Geoscience, 342, 412 – 424, doi:DOI:10.1016/j.crte.2009.09.012, URL http://www.sciencedirect.com/science/article/B6X1D-4Y0TDTH-1/2/557d34da1cd49b4bb328a444bcc5dbe9, atmosphére vue de l'espace, 2010.

Brohan, P., Kennedy, J. J., Harris, I., Tett, S. F. B., and Jones, P. D.: Uncertainty estimates in regional and global observed temperature changes: A new data set from 1850, J. Geophys. Res., 111, doi:10.1029/2005JD006548, 2006.

Chen, H., Winderlich, J., Gerbig, C., Hoefer, A., Rella, C. W., Crosson, E. R., Van Pelt, A. D., Steinbach, J., Kolle, O., Beck, V., Daube, B. C., Gottlieb, E. W., Chow, V. Y., Santoni, G. W., and Wofsy, S. C.: High-accuracy contin-

uous airborne measurements of greenhouse gases (CO_2 and CH_4) using the cavity ring-down spectroscopy (CRDS) technique, Atmospheric Measurement Techniques, 3, 375–386, doi:10.5194/amt-3-375-2010, 2010.

Crisp, D., Atlas, R. M., Breon, F. M., Brown, L. R., Burrows, J. P., Ciais, P., Connor, B. J., Doney, S. C., Fung, I. Y., Jacob, D. J., Miller, C. E., O'Brien, D., Pawson, S., Randerson, J. T., Rayner, P., Salawitch, R. J., Sander, S. P., Sen, B., Stephens, G. L., Tans, P. P., Toon, G. C., Wennberg, P. O., Wofsy, S. C., Yung, Y. L., Kuang, Z., Chudasama, B., Sprague, G., Weiss, B., Pollock, R., Kenyon, D., and Schroll, S.: The Orbiting Carbon Observatory (OCO) mission, Advances in Space Research, 34, 700 – 709, doi:DOI:10.1016/j.asr.2003.08.062, URL http://www.sciencedirect.com/science/article/B6V3S-4C7DC5T-F/2/2cc8ffed09701a5cf111c2b339c28f59, trace Constituents in the Troposphere and Lower Stratosphere, 2004.

Deutscher, N. M.: Investigating greenhouse gases in Australia using atmospheric measurements with fourier transform spectrometry and atmospheric modeling, Ph.D. thesis, University of Wollongong, School of Chemistry, Australia, URL http://ro.uow.edu.au/theses/3112/, 2009.

Deutscher, N. M., Griffith, D. W. T., Bryant, G. W., Wennberg, P. O., Toon, G. C., Washenfelder, R. A., Keppel-Aleks, G., Wunch, D., Yavin, Y., Allen, N. T., Blavier, J.-F., Jiménez, R., Daube, B. C., Bright, A. V., Matross, D. M., Wofsy, S. C., and Park, S.: Total column CO_2 measurements at Darwin, Australia - site description and calibration against in situ aircraft profiles, 3, 947–958, doi:10.5194/amt-3-947-2010, URL http://www.atmos-meas-tech.net/3/947/2010/, 2010.

Dufour, E., Bréon, F.-M., and Peylin, P.: CO_2 column averaged mixing ratio from

inversion of ground-based solar spectra, J. Geophys. Res., 109, D09 304, doi: 10.1029/2003JD004469, 2004.

Frankenberg, C., Warneke, T., Butz, A., Aben, I., Hase, F., Spietz, P., and Brown, L. R.: Pressure broadening in the $2\nu 3$ band of methane and its implication on atmospheric retrievals, Atmos. Chem. Phys, 8, 5061–5075, 2008.

Fraser, A., Chan Miller, C., Palmer, P. I., Deutscher, N. M., Jones, N. B., and Griffith, D. W. T.: The Australian methane budget: interpreting surface and train-borne measurements using a chemistry transport model, J. Geophys. Res., URL `http://www.geos.ed.ac.uk/research/eochem/pubs/fraser_wetlands_agu_submit_figs.pdf`, submitted, 2011.

Geibel, M. C., Gerbig, C., and Feist, D. G.: A new fully automated FTIR system for total column measurements of greenhouse gases, Atmospheric Measurement Techniques, 3, 1363–1375, doi:10.5194/amt-3-1363-2010, URL `http://www.atmos-meas-tech.net/3/1363/2010/`, 2010.

Gerbig, C., Schmitgen, S., Kley, D., Volz-Thomas, A., Dewey, K., and Haaks, D.: An improved fast-response vacuum-UV resonance fluorescence CO instrument, Journal Geophysical Research, 104, 1699–1704, 1999.

Gerbig, C., Körner, S., and Lin, J. C.: Vertical mixing in atmospheric tracer transport models: error characterization and propagation, Atmos. Chem. Phys., 8, 591–602, doi:10.5194/acp-8-591-2008, 2008.

GLOBALVIEW-CO2: Cooperative Atmospheric Data Integration Project - Carbon Dioxide. CD-ROM, NOAA ESRL, Boulder, Colorado, URL `ftp://ftp.cmdl.noaa.gov/ccg/co2/GLOBALVIEW`, 2009a.

GLOBALVIEW-CO2: Cooperative Atmospheric Data Integration Project - Carbon Dioxide. CD-ROM, NOAA ESRL, Boulder, Colorado, URL `ftp://ftp.cmdl.noaa.gov/ccg/co2/GLOBALVIEW`, 2010b.

Gloor, M., Fan, S.-M., Pacala, S., and Sarmiento, J.: Optimal sampling of the atmosphere for purpose of inverse modeling: A model study, Global Biogeochem. Cycles, 14, 407–428, doi:10.1029/1999GB900052, 2000.

Gordon, I. E., Kassi, S., Campargue, A., and Toon, G. C.: First identification of the electric quadrupole transitions of oxygen in the solar and laboratory spectra, Journal of Quantitative Spectroscopy and Radiative Transfer, 2010.

Griffiths, P. R. and de Haseth, J. A.: Fourier Transform Infrared Spectrometry, Wiley-Interschience, 1986.

Gurney, K. R., Rachel M. Law, A. S. D., Rayner, P. J., Baker, D., Bousquet, P., Bruhwiler, L., Chen, Y.-H., Ciais, P., Fan, S., Fung, I. Y., Gloor, M., Heimann, M., Higuchi, K., John, J., Maki, T., Maksyutov, S., Masarie, K., Peylin, P., Prather, M., Pak, B. C., Randerson, J., Sarmiento, J., Taguchi, S., Takahashi, T., and Yuen, C.-W.: Towards robust regional estimates of CO_2 sources and sinks using atmospheric transport models, Nature, 415, 626–630, doi:10.1038/415626a, 2002.

Hase, F.: Linefit spectrum fitting algorithm, URL `http://www-imk.fzk.de/asf/ftir/linefit.htm`, 2010.

Hase, F., Blumenstock, T., and Paton-Walsh, C.: Analysis of the instrumental line shape of high-resolution Fourier Transform IR spectrometers with gas cell measurements and new retrieval software, Appl. Opt., 38, 3417–3422, doi:10.1364/AO.38.003417, 1999.

Irion, F. W., Gunson, M. R., Toon, G. C., Chang, A. Y., Eldering, A., Mahieu, E., Manney, G. L., Michelsen, H. A., Moyer, E. J., Newchurch, M. J., Osterman, G. B., Rinsland, C. P., Salawitch, R. J., Sen, B., Yung, Y. L., and Zander, R.: Atmospheric Trace Molecule Spectroscopy (ATMOS) Experiment Version 3 data retrievals, Appl. Opt., 41, 6968–6979, doi:10.1364/AO.41.006968, 2002.

Janssen, M. A.: Atmospheric Remote Sensing by Microwave Radiometry, Wiley-Interschience, 1993.

Jenouvrier, A., Daumont, L., Regalia-Jarlot, L., Tyuterev, V. G., Carleer, M., Vandaele, A. C., Mikhailenko, S., and Fally, S.: Fourier transform measurements of water vapor line parameters in the 4200-6600 cm-1 region, Journal of Quantitative Spectroscopy and Radiative Transfer, 105, 326 – 355, 2007.

Kalnay, E., Kanamitsu, M., Kistler, R., Collins, W., Deaven, D., Gandin, L., Iredell, M., Saha, S., White, G., Woollen, J., Zhu, Y., Leetmaa, A., Reynolds, R., Chelliah, M., Ebisuzaki, W., Higgins, W., Janowiak, J., Mo, K. C., Ropelewski, C., Wang, J., Jenne, R., and Joseph, D.: The NCEP/NCAR 40-Year Reanalysis Project, Bulletin of the American Meteorological Society, 77, 437–471, doi:10.1175/1520-0477(1996)077⟨0437:TNYRP⟩2.0.CO;2, URL http://journals.ametsoc.org/doi/abs/10.1175/1520-0477%281996%29077%3C0437%3ATNYRP%3E2.0.CO%3B2, 1996.

Karion, A., Sweeney, C., Tans, P., and Newberger, T.: AirCore: An Innovative Atmospheric Sampling System, Journal of Atmospheric and Oceanic Technology, 27, 1839–1853, doi:10.1175/2010JTECHA1448.1, URL http://journals.ametsoc.org/doi/abs/10.1175/2010JTECHA1448.1, 2010.

Keeling, C. D. and Whorf, T. P.: A Compendium of Data on Global Change, chap. Atmospheric CO2 records from sites in the SIO air sampling network, U.S. Department of Energy, Oak Ridge, Tenn., U.S., 2005.

Keeling, C. D., Bacastow, R. B., Bainbridge, A. E., Ekdahl, C. A., Guenther, P. R., Waterman, L. S., and Chin, J. F. S.: Atmospheric carbon dioxide variations at Mauna Loa Observatory, Hawaii, Tellus, 28, 538–551, doi:10.1111/j.2153-3490.1976.tb00701.x, URL http://dx.doi.org/10.1111/j.2153-3490.1976.tb00701.x, 1976.

Keppel-Aleks, G., Toon, G. C., Wennberg, P. O., and Deutscher, N. M.: Reducing the impact of source brightness fluctuations on spectra obtained by Fourier-transform spectrometry, Appl. Opt., 46, 4774–4779, doi:10.1364/AO.46.004774, URL http://ao.osa.org/abstract.cfm?URI=ao-46-21-4774, 2007.

Kuze, A., Suto, H., Nakajima, M., and Hamazaki, T.: Thermal and near infrared sensor for carbon observation Fourier-transform spectrometer on the Greenhouse Gases Observing Satellite for greenhouse gases monitoring, Appl. Opt., 48, 6716–6733, doi:10.1364/AO.48.006716, URL http://ao.osa.org/abstract.cfm?URI=ao-48-35-6716, 2009.

Lean, J. L. and Rind, D. H.: How will Earth's surface temperature change in future decades?, Geophys. Res. Lett., 36, doi:10.1029/2009GL038932, l15708, 2009.

Luo, M., Cicerone, R. J., and Russell III, J. M.: Analysis of Halogen Occultation Experiment HF versus CH4 correlation plots: Chemistry and transport implications, J. Geophys. Res., 100, 13,927–13,937, doi:10.1029/95JD00621, 1995.

Marshall, J.: Personal communication, information about the current status of GOSAT retrieval., 2011.

Masarie, K. A. and Tans, P. P.: Extension and integration of atmospheric carbon dioxide data into a globally consistent measurement record, J. Geophys. Res., 100, doi:10.1029/95JD00859, 1995.

Messerschmidt, J., Macatangay, R., Nothold, J., Petri, C., Warneke, T., and Weinzierl, C.: Side by side measurements of CO2 by ground-based Fourier transform spectrometry (FTS), Tellus B, 62, 749–758, doi:10.1111/j.1600-0889.2010.00491.x, URL http://dx.doi.org/10.1111/j.1600-0889.2010.00491.x, 2010a.

Messerschmidt, J., Macatangay, R., Notholt, J., Petri, C., Warneke, T., and Weinzierl, C.: Side by side measurements of CO2 by ground-based Fourier transform spectrometry (FTS), doi:10.1111/j.1600-0889.2010.00491.x, 2010b.

Messerschmidt, J., Geibel, M. C., Blumenstock, T., Chen, H., Deutscher, N. M., Engel, A., Feist, D. G., Gerbig, C., Gisi, M., Hase, F., Katrynski, K., Kolle, O., Lavrič, J. V., Notholt, J., Palm, M., Ramonet, M., Rettinger, M., Schmidt, M., Sussmann, R., Toon, G. C., Truong, F., Warneke, T., Wennberg, P. O., Wunch, D., and Xueref-Remy, I.: Calibration of TCCON column-averaged CO_2: the first aircraft campaign over European TCCON sites, Atmospheric Chemistry and Physics Discussions, 11, 14 541–14 582, doi:10.5194/acpd-11-14541-2011, URL http://www.atmos-chem-phys-discuss.net/11/14541/2011/, 2011.

Newman, S. M., Lane, I. C., Orr-Ewing, A., Newnham, D. A., and Ballard, J.: Integrated absorption intensity and Einstein coefficients for the O2 a 1 Delta g-X 3 Sigma g-(0, 0) transition: A comparison of cavity ringdown and high resolution Fourier transform spectroscopy with a long-path absorption cell, Journal of Chemical Physics, 110, 10 749–10 757, 1999.

Norton, R. H. and Rinsland, C. P.: ATMOS data processing and science analysis methods, Appl. Opt., 30, 389–400, doi:10.1364/AO.30.000389, 1991.

Notholt, J., Toon, G., Stordal, F., Solberg, S., Schmidbauer, N., Becker, E., Meier, A., and Sen, B.: Seasonal variations of atmospheric trace gases in the high Arctic at 79°N, J. Geophys. Res., 102, 12,855–12,861, doi:10.1029/97JD00337, 1997.

Parry, M., Canziani, O.F. andPalutikof, J., van der Linden, P., and Hanson, C., eds.: IPCC Fourth Assessment Report: Climate Change 2007 (AR4), chap. Working Group II: Impacts, Adaptation and Vulnerability, Cambridge University Press, Cambridge, United Kingdom and New York, NY, USA., 2007.

Peters, W., Jacobson, A. R., Sweeney, C., Andrews, A. E., Conway, T. J., Masarie, K., Miller, J. B., Bruhwiler, L. M. P., Pétron, G., Hirsch, A. I., Worthy, D. E. J., van der Werf, G. R., Randerson, J. T., Wennberg, P. O., Krol, M. C., and Tans, P. P.: An atmospheric perspective on North American carbon dioxide exchange: CarbonTracker, PNAS, 104, 18 925–18 930, 2007.

Petersen, A. K., Warneke, T., Frankenberg, C., Bergamaschi, P., Gerbig, C., Notholt, J., Buchwitz, M., Schneising, O., and Schrems, O.: First ground-based FTIR-observations of methane in the tropics, Atmos. Chem. Phys., 10, 2303–2320, doi:10.5194/acpd-10-2303-2010, URL `http://www.atmos-chem-phys-discuss.net/10/2303/2010/`, 2010.

Pillai, D., Gerbig, C., Marshall, J., Ahmadov, R., Kretschmer, R., Koch, T., and Karstens, U.: High resolution modeling of CO_2 over Europe: implications for representation errors of satellite retrievals, Atmos. Chem. Phys., 10, 83–94, doi:10.5194/acp-10-83-2010, URL `http://www.atmos-chem-phys.net/10/83/2010/`, 2010.

Popa, M. E., Gloor, M., Manning, A. C., Jordan, A., Schultz, U., Haensel, F., Seifert, T., and Heimann, M.: Measurements of greenhouse gases and related tracers at Bialystok tall tower station in Poland, Atmospheric Measurement Techniques, 3, 407–427, doi:10.5194/amt-3-407-2010, URL `http://www.atmos-meas-tech.net/3/407/2010/`, 2010.

Pscheidt, I.: Personal communication, information about results of the PROFFIT retival of Karlsuhe data, 2009.

Rayner, P. J. and O'Brien, D. M.: The utility of remotely sensed CO_2 concentration data in surface source inversions, Geophys. Res. Lett., 28, 175–178, doi:10.1029/2000GL011912, 2001.

Rayner, P. J., Enting, I. G., Francey, R. J., and Langenfelds, R.: Reconstructing the recent carbon cycle from atmospheric CO_2, $\delta^{13}C$ and O_2/N_2 observations, Tellus, 51B, 213–232, doi:10.1034/j.1600-0889.1999.t01-1-00008.x, 1999.

Rödenbeck, C.: Estimating CO_2 sources and sinks from atmospheric mixing ratio measurements using a global inversion of atmospheric transport, Tech. Rep. 6, Max Planck Institute for Biogeochemistry, Jena, Germany, URL `http://www.bgc-jena.mpg.de/mpg/websiteBiogeochemie/Publikationen/Technical_Reports/tech_report6.pdf`, 2005.

Rodgers, C. D. and Connor, B. J.: Intercomparison of remote sounding instruments, J. Geophys. Res., 108, 4116–4229, doi:10.1029/2002JD002299, 2003.

Rosenzweig, C., Karoly, D., Vicarelli, M., Neofotis, P., Wu, Q., Casassa, G., Menzel, A., Root, T. L., Estrella, N., Seguin, B., Tryjanowski, P., Liu, C., Rawlins, S., and Imeson, A.: Attributing physical and biological impacts to anthropogenic climate change, Nature, 453, 353 – 357, doi:10.1038/nature06937, 2008.

Rothman, L., Gordon, I., Barbe, A., Benner, D., Bernath, P., Birk, M., Boudon, V., Brown, L., Campargue, A., Champion, J.-P., Chance, K., Coudert, L., Dana, V., Devi, V., Fally, S., Flaud, J.-M., Gamache, R., Goldman, A., Jacquemart, D., Kleiner, I., Lacome, N., Lafferty, W., Mandin, J.-Y., Massie, S., Mikhailenko, S., Miller, C., Moazzen-Ahmadi, N., Naumenko, O., Nikitin, A., Orphal, J., Perevalov, V., Perrin, A., Predoi-Cross, A., Rinsland, C., Rotger, M., Simeckova, M., Smith, M., Sung, K., Tashkun, S., Tennyson, J., Toth, R., Vandaele, A., and Auwera, J. V.: The HITRAN 2008 molecular spectroscopic database, Journal of Quantitative Spectroscopy and Radiative Transfer, 110, 533 – 572, doi:DOI:10.1016/j.jqsrt.2009.02.013, URL `http://www.sciencedirect.com/science/article/B6TVR-4VPM5M4-2/2/464a427cb2670a9be660fe6e0e4d0272`, 2009.

Solomon, S., Qin, D., Manning, M., Chen, Z., Marquis, M., Averyt, K., Tignor, M., and Miller, H., eds.: IPCC Fourth Assessment Report: Climate Change 2007 (AR4), chap. Working Group I: The Physical Science Basis, Cambridge University Press, Cambridge, United Kingdom and New York, NY, USA., 2007.

Tans, P.: NOAA/ESRL: Trends in Atmospheric Carbon Dioxide, URL `http://www.esrl.noaa.gov/gmd/ccgg/trends`, 2011.

Tans, P. P., Fung, I. Y., and Takahashi, T.: Observational constraints on the global atmospheric CO_2 budget, Science, 247, 1431–1438, doi:10.1126/science.247.4949.1431, 1990.

Thompson, R. L., Manning, A. C., Gloor, E., Schultz, U., Seifert, T., Hänsel, F., Jordan, A., and Heimann, M.: In-situ measurements of oxygen, carbon monoxide and greenhouse gases from Ochsenkopf tall tower in Germany, Atmo-

spheric Measurement Techniques, 2, 573–591, doi:10.5194/amt-2-573-2009, URL http://www.atmos-meas-tech.net/2/573/2009/, 2009.

Toon, G., Blavier, J.-F., Washenfelder, R., Wunch, D., Keppel-Aleks, G., Wennberg, P., Connor, B., Sherlock, V., Griffith, D., Deutscher, N., and Notholt, J.: Total Column Carbon Observing Network (TCCON), in: Fourier Transform Spectroscopy, OSA Technical Digest (CD), p. paper JMA3, Optical Society of America, Vancouver, Canada, URL http://www.opticsinfobase.org/abstract.cfm?uri=FTS-2009-JMA3, 2009.

Toth, R.: Measurements of positions, strengths and self-broadened widths of H2O from 2900 to 8000cm-1:line strength analysis of the 2nd triad bands, Journal of Quantitative Spectroscopy and Radiative Transfer, 94, 51–107, 2005.

Toth, R. A., Brown, L. R., Miller, C. E., Malathy Devi, V., and Benner, D.: Spectroscopic database of CO2 line parameters: 4300–7000cm- 1, Journal of Quantitative Spectroscopy and Radiative Transfer, 109, 906–921, 2008.

Warneke, T., Yang, Z., Olsen, S., Körner, S., Notholt, J., Toon, G. C., Velazco, V., Schulz, A., and Schrems, O.: Seasonal and latitudinal variations of column averaged volume-mixing ratios of atmospheric CO_2, Geophys. Res. Lett., 32, L03 808, doi:10.1029/2004GL021597, 2005.

Warneke, T., Petersen, A. K., Gerbig, C., Jordan, A., Rödenbeck, C., Rothe, M., Macatangay, R., Notholt, J., and Schrems, O.: Co-located column and in situ measurements of CO_2 in the tropics compared with model simulations, Atmos. Chem. Phys., 10, 5593–5599, doi:10.5194/acp-10-5593-2010, URL http://www.atmos-chem-phys.net/10/5593/2010/, 2010.

Washenfelder, R. A., Wennberg, P. O., and Toon, G. C.: Tropospheric methane

retrieved from ground-based near-IR solar absorption spectra, Geophys. Res. Lett., 30, 2226, doi:10.1029/2003GL017969, 2003.

Washenfelder, R. A., Toon, G. C., Blavier, J.-F., Yang, Z., Allen, N. T., Wennberg, P. O., Vay, S. A., Matross, D. M., and Daube, B. C.: Carbon dioxide column abundances at the Wisconsin Tall Tower site, J. Geophys. Res., 111, D22 305, doi:10.1029/2006JD007154, 2006.

Winderlich, J., Chen, H., Höfer, A., Gerbig, C., Seifert, T., Kolle, O., Kaiser, C., Lavrič, J. V., and Heimann, M.: Continuous low-maintenance CO_2/CH_4/H_2O measurements at the Zotino Tall Tower Observatory (ZOTTO) in Central Siberia, Atmospheric Measurement Techniques Discussions, 3, 1399–1437, doi:10.5194/amtd-3-1399-2010, URL `http://www.atmos-meas-tech-discuss.net/3/1399/2010/`, 2010.

Wunch, D.: Personal communication, information about different atm linelists and details about fitting procedure, 2010.

Wunch, D., Toon, G. C., Wennberg, P. O., Wofsy, S. C., Stephens, B. B., Fischer, M. L., Uchino, O., Abshire, J. B., Bernath, P., Biraud, S. C., Blavier, J.-F. L., Boone, C., Bowman, K. P., Browell, E. V., Campos, T., Connor, B. J., Daube, B. C., Deutscher, N. M., Diao, M., Elkins, J. W., Gerbig, C., Gottlieb, E., Griffith, D. W. T., Hurst, D. F., Jiménez, R., Keppel-Aleks, G., Kort, E. A., Macatangay, R., Machida, T., Matsueda, H., Moore, F., Morino, I., Park, S., Robinson, J., Roehl, C. M., Sawa, Y., Sherlock, V., Sweeney, C., Tanaka, T., and Zondlo, M. A.: Calibration of the Total Carbon Column Observing Network using aircraft profile data, Atmospheric Measurement Techniques, 3, 1351–1362, doi:10.5194/amt-3-1351-2010, URL `http://www.atmos-meas-tech.net/3/1351/2010/`, 2010.

Wunch, D., Toon, G. C., Blavier, J.-F. L., Washenfelder, R., Notholt, J., Connor, B. J., Griffith, D. W. T., Sherlock, V., and Wennberg, P. O.: The Total Carbon Column Observing Network (TCCON), 369, 2087–2112, doi: 10.1098/rsta.2010.0240, 2011.

Yang, Z., Toon, G. C., Margolis, J. S., and Wennberg, P. O.: Atmospheric CO_2 retrieved from ground-based IR solar spectra, Geophys. Res. Lett., 29, 1339, doi:10.1029/2001GL014537, 2002.

Yang, Z., Wennberg, P., Cageao, R., Pongetti, T., Toon, G., and Sander, S.: Ground-based photon path measurements from solar absorption spectra of the O2 A-band, Journal of Quantitative Spectroscopy and Radiative Transfer, 90, 309–321, 2005.

Yokota, T., Yoshida, Y., Eguchi, N., Ota, Y., Tanaka, T., Watanabe, H., and Maksyutov, S.: Global concentrations of CO_2 and CH_4 retrieved from GOSAT: first preliminary results, 5, 160–163, doi:10.2151/sola.2009-041, 2009.

York, D., Evensen, N. M., Martínez, M. L., and Delgado, J. D. B.: Unified equations for the slope, intercept, and standard errors of the best straight line, American Journal of Physics, 72, 367–375, doi:10.1119/1.1632486, URL `http://link.aip.org/link/?AJP/72/367/1`, 2004.

Zöphel, H.: Test and installation of an automatic weather station to provide ground-based FTIR measurements for TCCON, Master's thesis, University of Applied Sciences, Jena, Germany, URL `http://www.bgc-jena.mpg.de/bgc-systems/pmwiki2/uploads/PhdAmpDiplomaThesis/zoephel.pdf`, 2008.

Appendices

Appendix A

The Dome

A.1 Part list

Table A.1: Components of the Solar Tracker Dome

Component	Part	Specification
Frame	X-Profile	SMT Profile 5 20x20
		SMT Profile 5 40x20
	Brackets	SMT Bracketset 5 20x20 ZN
	Brackets	SMT Bracketset 5 40x40 ZN
	Hinges	SMT S205SCHPA
	Slot nuts	SMT S205NSMS5
	Slot nuts	SMT S205NSOS5
	Cover	Aluminum plates
Drive train	Motor	Framo-Morat 6-30-MR 30K
	Axis	Maedler splined shaft KN16x20x1500 C45, type 64843500
	Additional parts	Maedler splined hub KN16x20, type 6489305
	Additional parts	Maedler splined hub with flange KN16x20, type 64899505
	Additional parts	Maedler clamp ring KN16x20, type 64899605
	Tooth belt	Wieland SECA tooth belt 50AT10/2500V
	Belt pulley	Wieland tooth wheel 66AT10/20-2
	Belt pulley	Wieland tooth wheel 66AT10/60-0
Electronics	Contactors	ABB BC 6-30-01 (GJL1213001R0011)
	Overload switch	Telemecanique GV2ME10
	Position Sensors	Honeywell GLEB01C

A.2 Dimensional drawings

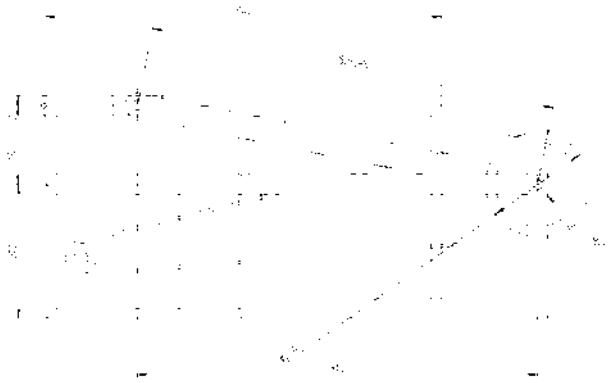

Figure A.1: Dimensional drawing of the BGC Solar Tracker Dome (side view in closed state). The half-round top cover panel is not shown in this drawing.

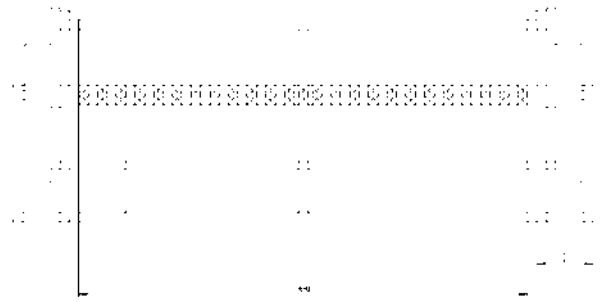

Figure A.2: Same as A.1 but back view in closed state.

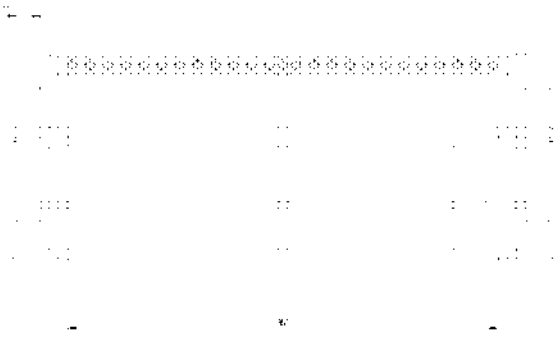

Figure A.3: Same as A.1 but front view in closed state.

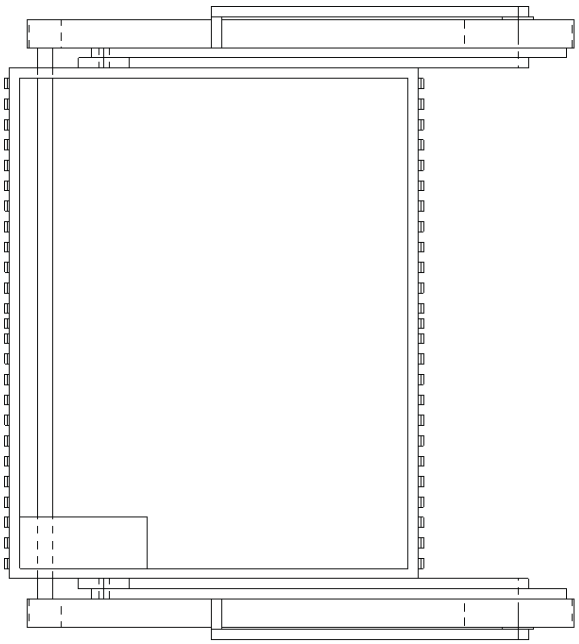

Figure A.4: Same as A.1 but top view in closed state.

Figure A.5: Same as A.1 but side view in half-open state.

A.3 Dome electronics

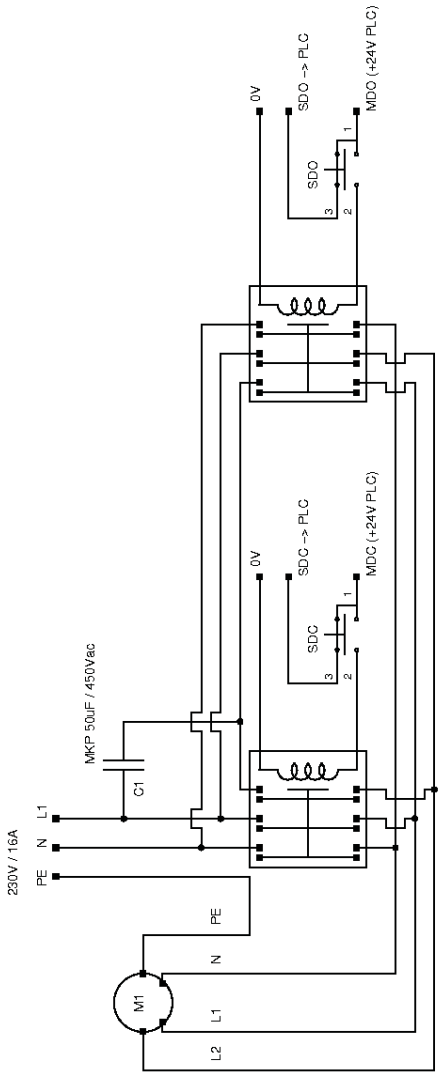

Figure A.6: Circuit diagram of the Solar Tracker Dome electronics.

Appendix B

The Shutter

B.1 Part list

Table B.1: Components of the Shutter

Component	Part	Specification
Frame	Shutter Block	Material: Polyamide
	Rails	Maedler type 64799420
	Rail mountings	Maedler type 64642000
	Ball bearings	Maedler type 64652020
	Baseplate	Material: Aluminum
Drive train	Motor	Framo-Morat Mini 0 W/D 450-30-250
Electronics	Contactors	ABB BC 6-30-01 (GJL1213001R0011)
	Overload switch	Telemecanique GV2ME10
	Position Sensors	Honeywell GLEB01C

B.2 Dimensional drawings

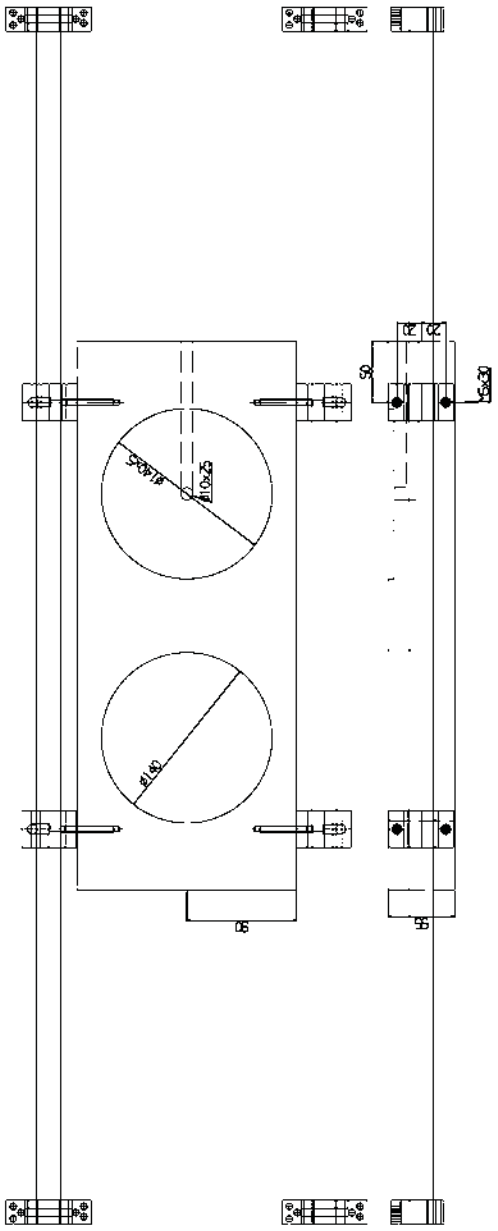

Figure B.1: Dimensional drawing of the Shutter (top and side view without base-plate and motor).

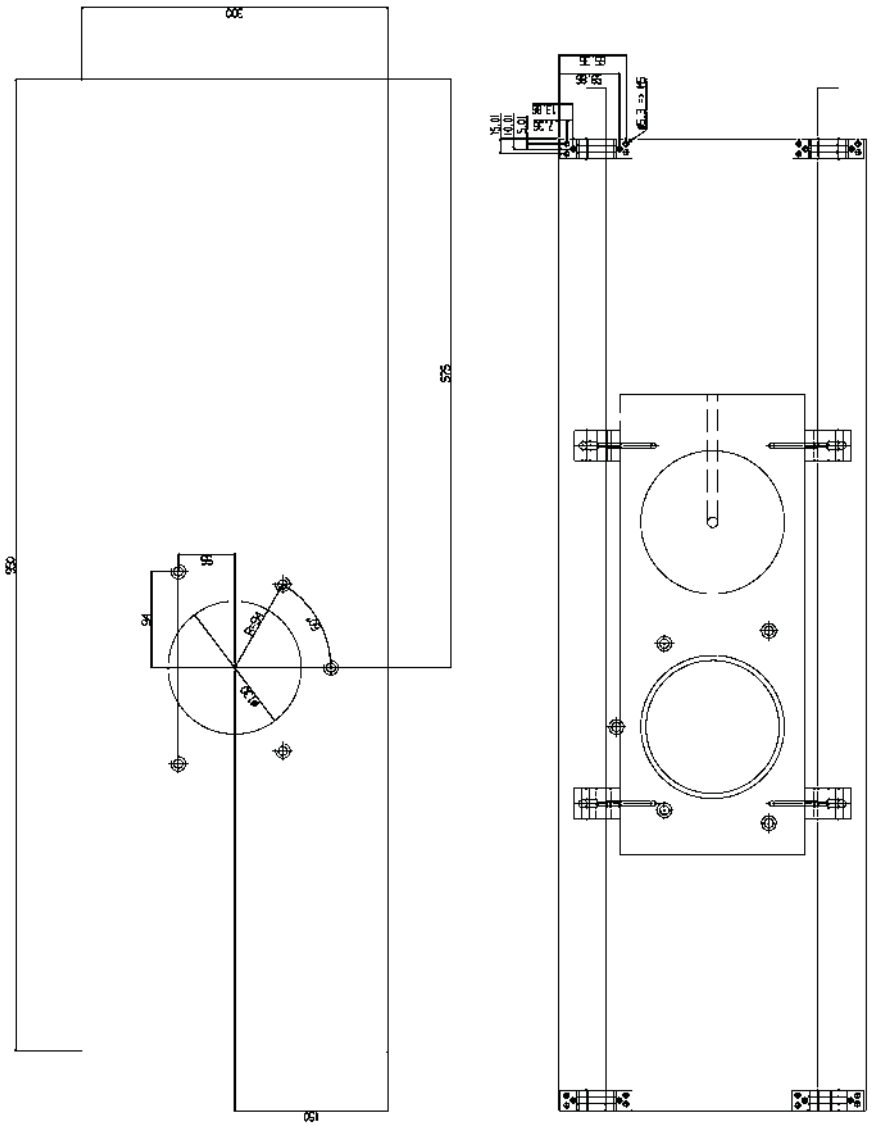

Figure B.2: Dimensional drawing of the Shutter and its baseplate (bottom and top view without motor).

B.3 Shutter electronics

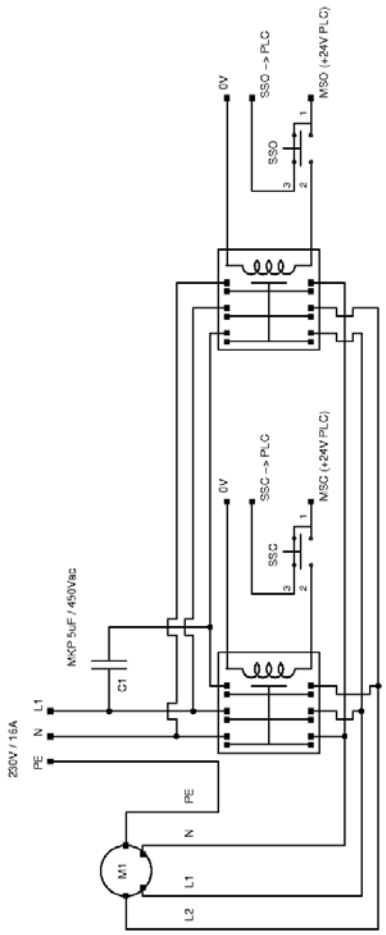

Figure B.3: Circuit diagram of the Shutter electronics.

Appendix C

PLC

C.1 Part List

Table C.1: Components of the Programmable Logic Controller (PLC)

Component	Part	Quantity
Controller	Unitronics Vision570-57-T40B + Ethernetport (V200-19-ET1)	1
Expansion Adapter	Unitronics EX-A1	1
Input Modules	Unitronics IO-DI16	2
Relay Modules	Unitronics IO-RO8	3
Software Version		Visilogic V8.0.1

C.2 Connection scheme

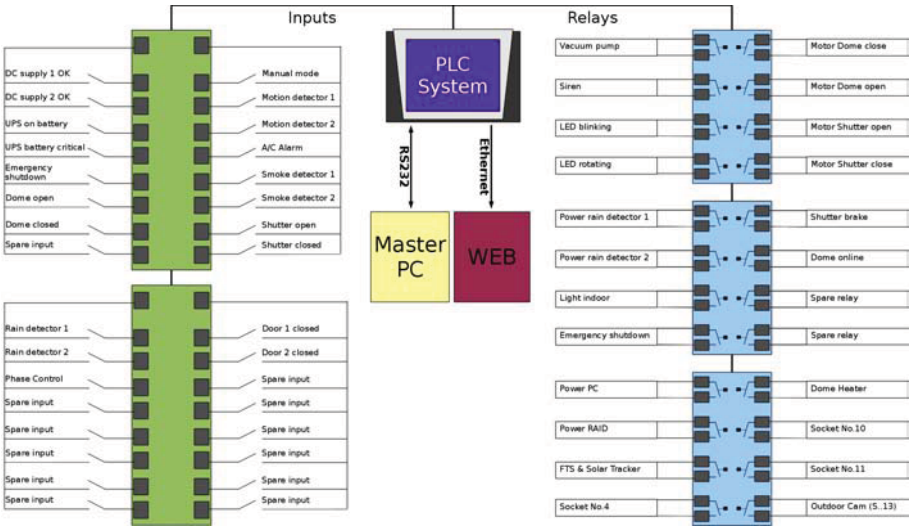

Figure C.1: Connection scheme of the PLC system.

C.3 PLC serial communication

Table C.2: Table of PLC commands for RS232 communication

Command	Operation
MDC1	Close Dome
MDO1	Open Dome
MSC1	Close Shutter
MSO1	Open Shutter
PMP0	Switch off Pump
PMP1	Switch on Pump
PR10	Disable Signal Rain Sensor 1
PR11	Enable Signal Rain Sensor 1
PR20	Disable Signal Rain Sensor 2
PR21	Enable Signal Rain Sensor 2
LLI0	Switch off LabLight
LLI1	Switch on LabLight
DOL1	Dome Online
DOL0	Dome Offline
ESD1	Turn on Emergency Shutdown sequence
ESD0	Turn off Emergency Shutdown sequence
R261	Switch on Relay 2.6
R260	Switch off Relay 2.6
R271	Switch on Relay 2.7
R270	Switch off Relay 2.7
FTS1	Switch on FTS and Tracker (Relay 3.2)
FTS0	Switch off FTS and Tracker (Relay 3.2)
R331	Switch on Socket 4
R330	Switch off Socket 4
HTR1	Switch on Dome Heater (Relay 3.4)
HTR0	Switch off Dome Heater (Relay 3.4)
R351	Switch on Socket 10
R350	Switch off Socket 10
R361	Switch on Socket 11
R360	Switch off Socket 11
R371	Switch on Cam3 - Dome
R370	Switch off Cam3 - Dome
STAT	No Operation

Table C.3: Table of PLC input and output strings for RS232 communication

String 1: Status of all Outputs Suffix 0 = inactive Suffix 1 = active	**Explanation**	**String 2: Status of all Inputs** Suffix 0 = inactive Suffix 1 = active	**Explanation**
MDC	Motor Dome Close Status	MAN	PLC Manual Mode Status
MDO	Motor Dome Open Status	MO1	Motion Detector 1 Status
MSC	Motor Shutter Close Status	MO2	Motion Detector 2 Status
MDO	Motor Shutter Open Status	ACA	A/C Alarm Status
PMP	Pump Status	SM1	Smoke Detector 1 Status
SIR	Siren Status	SM2	Smoke Detector 2 Status
LEB	LED Blinking Status	SSC	End Switch Shutter Closed Status
LER	LED Rotating Status	SSO	End Switch Shutter Open Status
PR1	Signal Rain Sensor 1 Status	DC1	24V Supply 1 Status
PR2	Signal Rain Sensor 2 Status	DC2	24V Supply 2 Status
LLI	Lab Light Status	BAT	UPS on AC Status
SBR	Shutter Brake Status	SDN	UPS Battery OK
ESD	Emergency Shutdown (Relay)	112	Input 1.12 Status
DOL	Dome Online Status	ESA	Emergency Shutdown (Input Signal)
R26	Relay 2.6 Status	SDC	End Switch Dome Closed Status
R27	Relay 2.7 Status	SDO	End Switch Dome Open Status
PC1	Power PC Status	RN1	Rain Detected Sensor 1 Status
PC2	Power RAID Status	RN2	Rain Detected Sensor 2 Status
FTS	FTS and Tracker (Relay 3.2) Status	DR1	Front Door Closed Status
R33	Relay 3.3 Status	DR2	Back Door Closed Status
HTR	Dome Heater (Relay 3.4) Status	PCS	Phase Control Switch Status
R35	Relay 3.5 Status	205	Input 2.05 Status
R36	Relay 3.6 Status	206	Input 2.06 Status
CM3	Cam3 - Dome - Status	207	Input 2.07 Status
		208	Input 2.08 Status
		209	Input 2.09 Status
		208	Input 2.08 Status
		209	Input 2.09 Status
		210	Input 2.10 Status
		211	Input 2.11 Status
		212	Input 2.12 Status
		213	Input 2.13 Status
		214	Input 2.14 Status
		215	Input 2.15 Status

Table C.4: Table of PLC alarm string for RS232 communication

String 3: Status of Alarm	Explanation
A1_MOVING	Dome or Shutter moving
A2_BATTERY	UPS on Battery
A2_MOTION	Motion detected
A2_DOORS	Door open
A3_SHUTDOWN	UPS Shutdown
A3_SMOKE	Smoke detected
A3_AIRCON	A/C Alarm
A3_RESTART	PC Restart
A3_DOME_ERROR	Dome Error
A3_SHUTTER_ERROR	Shutter Error
A3_EMERGENCY_SHUTDOWN	Emergency Shutdown active (5min countdown)

Appendix D

Flight tracks of the IMECC campaign overflights

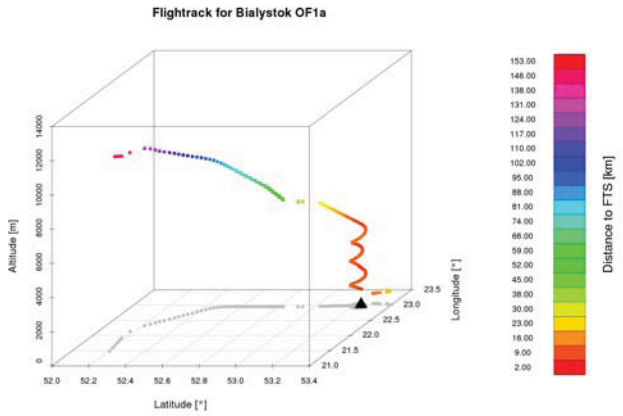

Figure D.1: Flight track of overflight Bialystok OF1a.

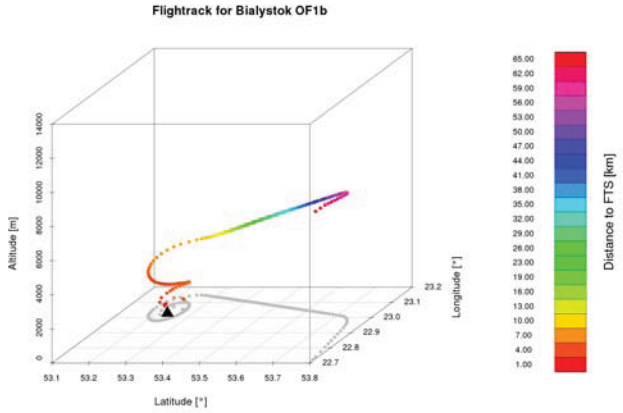

Figure D.2: Flight track of overflight Bialystok OF1b.

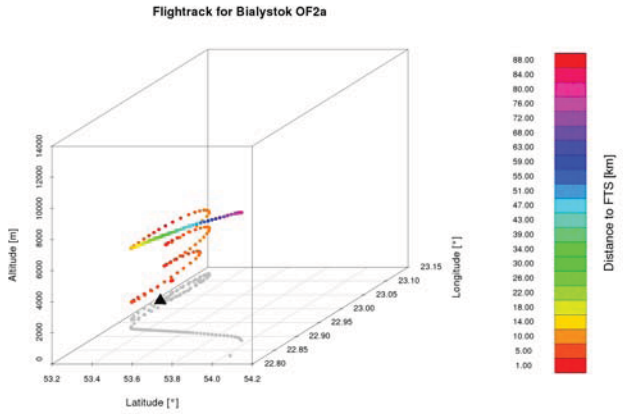

Figure D.3: Flight track of overflight Bialystok OF2a.

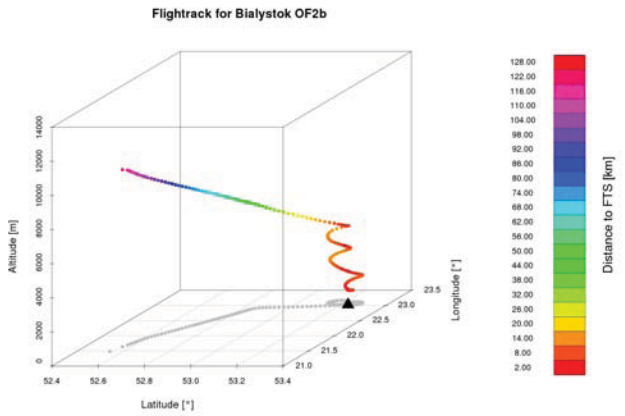

Figure D.4: Flight track of overflight Bialystok OF2b.

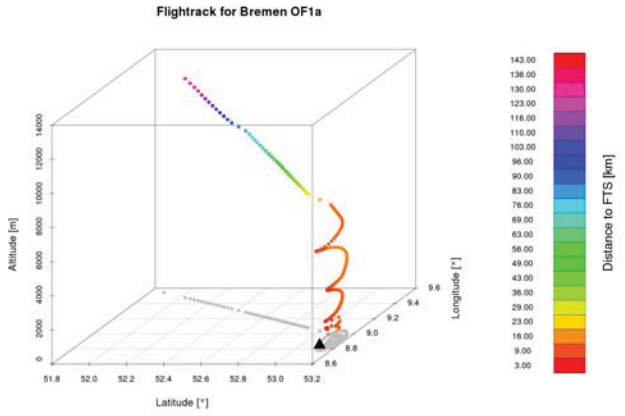

Figure D.5: Flight track of overflight Orleans OF1a.

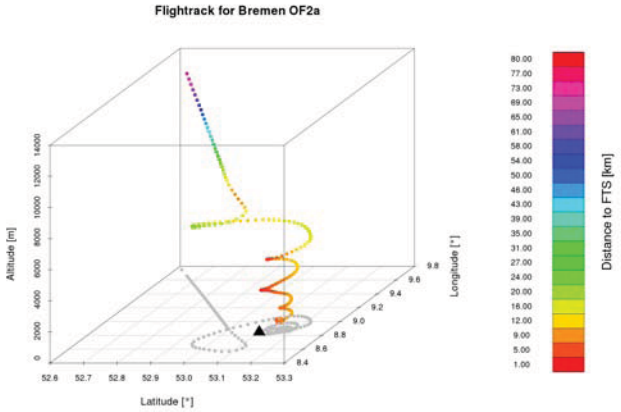

Figure D.6: Flight track of overflight Bremen OF2a.

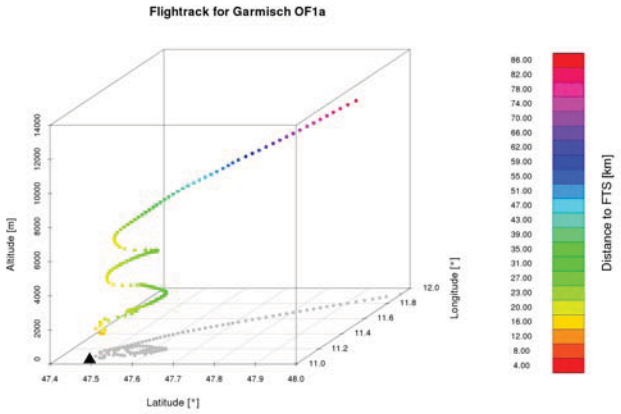

Figure D.7: Flight track of overflight Garmisch OF1a.

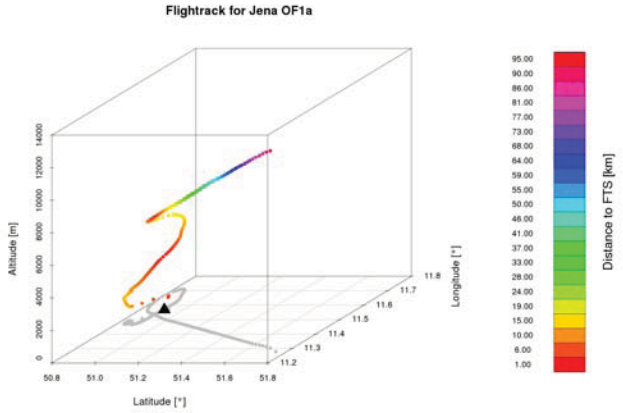

Figure D.8: Flight track of overflight Jena OF1a.

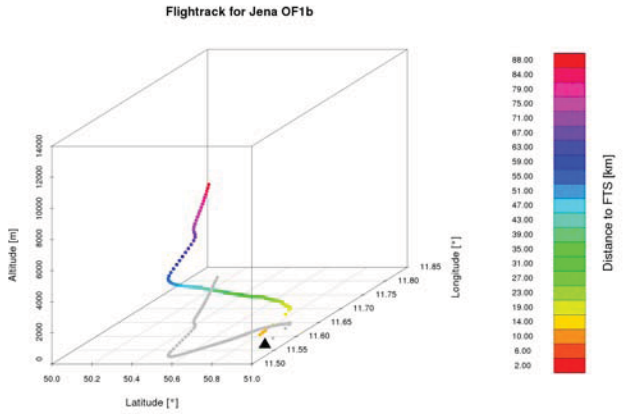

Figure D.9: Flight track of overflight Jena OF1b.

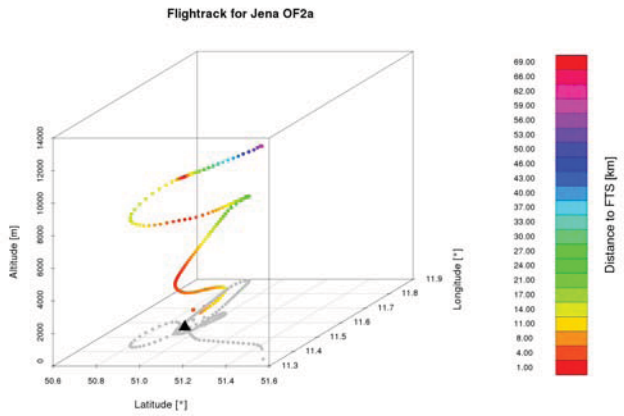

Figure D.10: Flight track of overflight Jena OF2a.

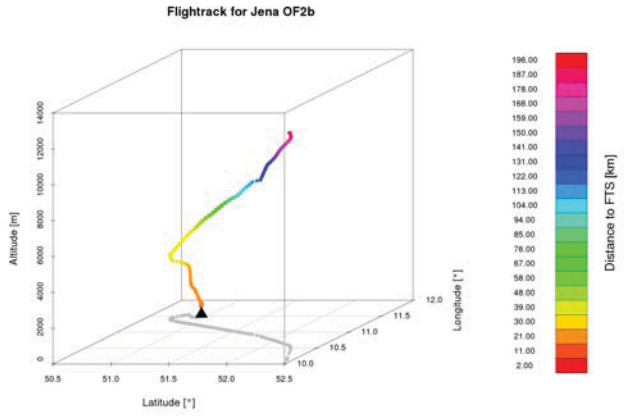

Figure D.11: Flight track of overflight Jena OF2b.

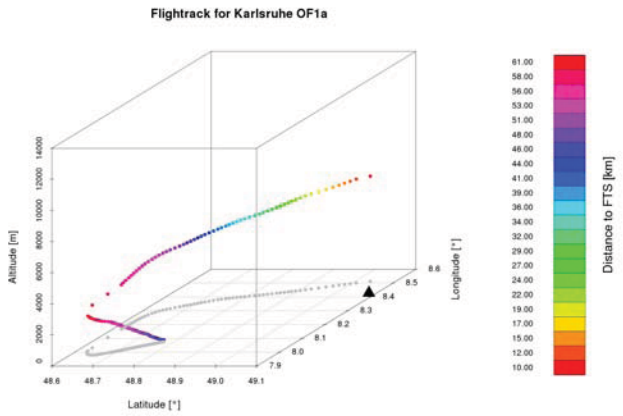

Figure D.12: Flight track of overflight Karlsruhe OF1a.

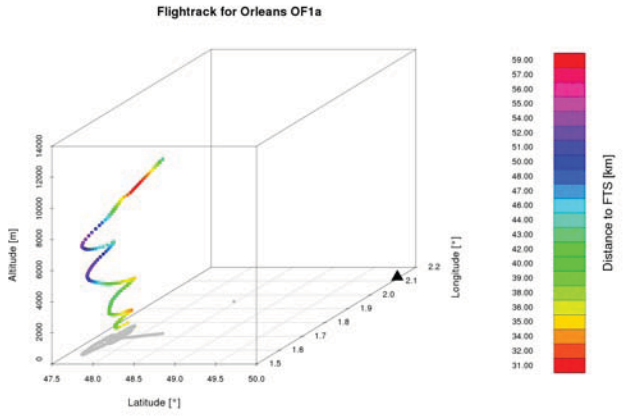

Figure D.13: Flight track of overflight Orleans OF1a.

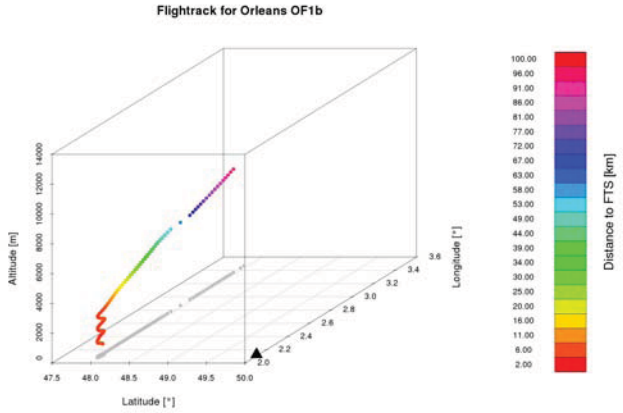

Figure D.14: Flight track of overflight Orleans OF1b.

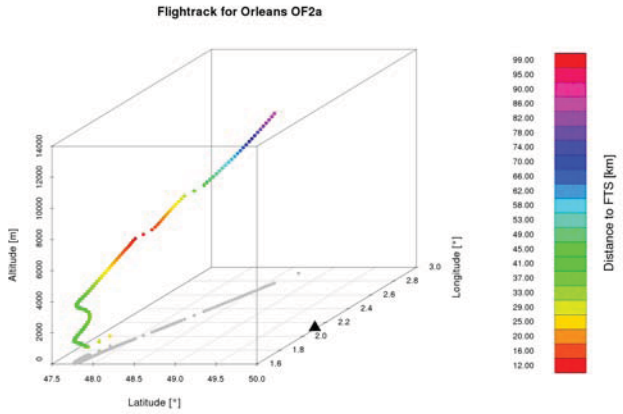

Figure D.15: Flight track of overflight Orleans OF2a.

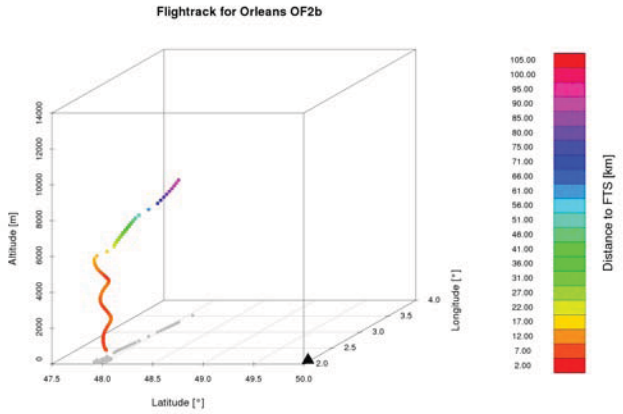

Figure D.16: Flight track of overflight Orleans OF2b.

Appendix E

Aircraft data of the IMECC campaign overflights

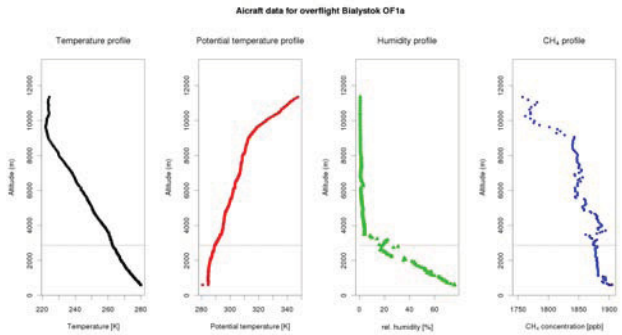

Figure E.1: Aircraft data of overflight Bialystok OF1a.

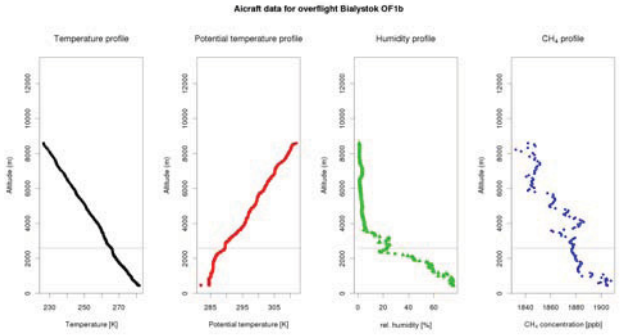

Figure E.2: Aircraft data of overflight Bialystok OF1b.

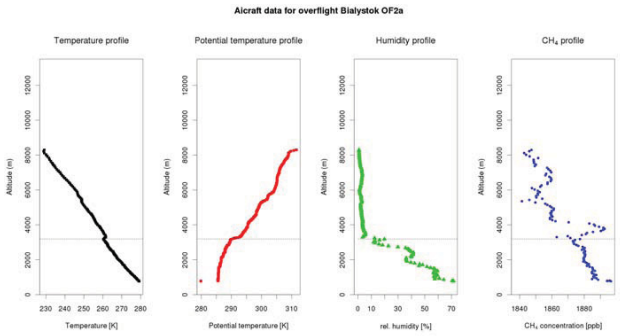

Figure E.3: Aircraft data of overflight Bialystok OF2a.

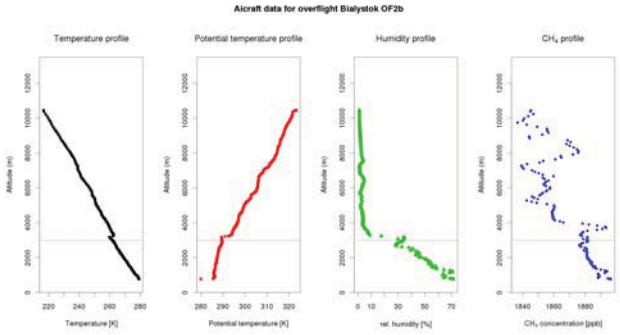

Figure E.4: Aircraft data of overflight Bialystok OF2b.

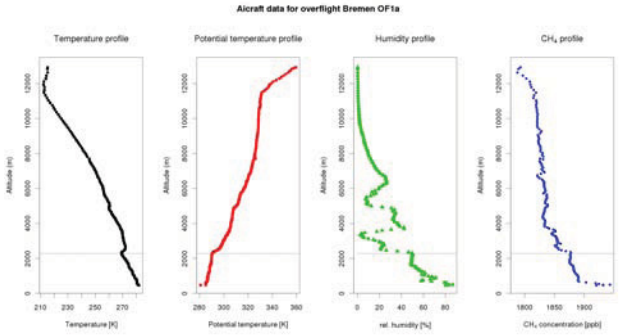

Figure E.5: Aircraft data of overflight Orleans OF1a.

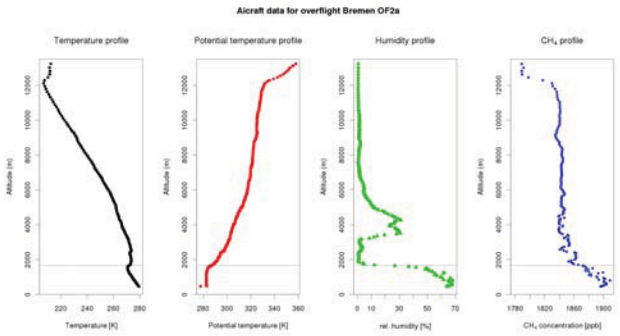

Figure E.6: Aircraft data of overflight Bremen OF2a.

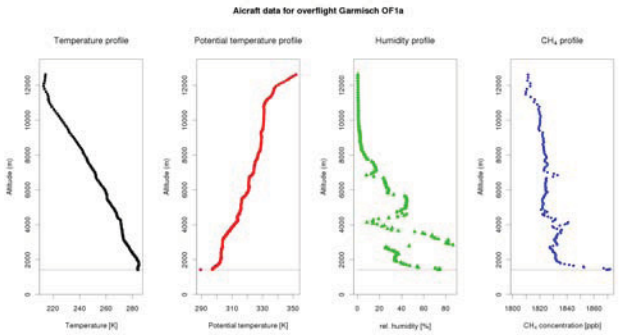

Figure E.7: Aircraft data of overflight Garmisch OF1a.

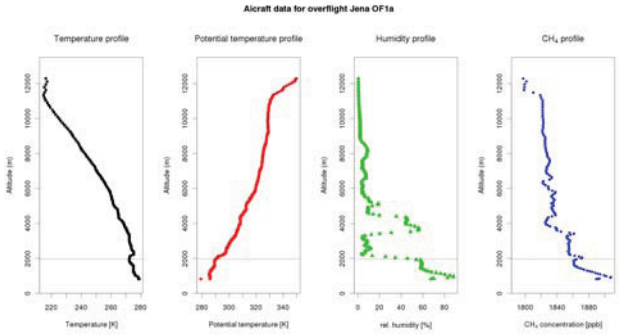

Figure E.8: Aircraft data of overflight Jena OF1a.

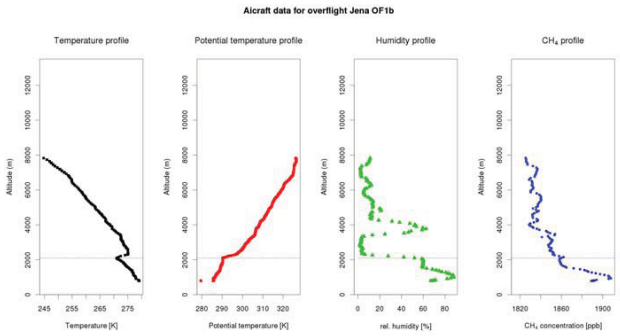

Figure E.9: Aircraft data of overflight Jena OF1b.

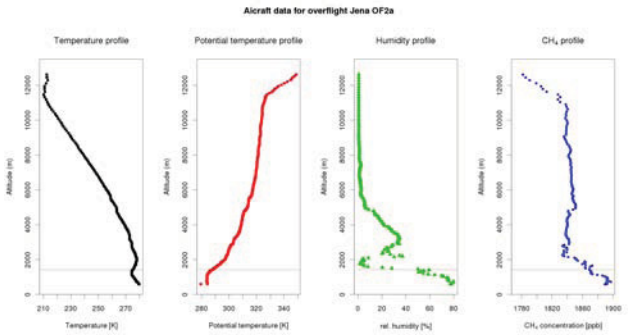

Figure E.10: Aircraft data of overflight Jena OF2a.

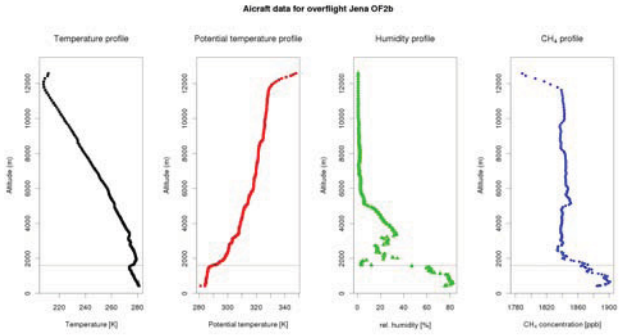

Figure E.11: Aircraft data of overflight Jena OF2b.

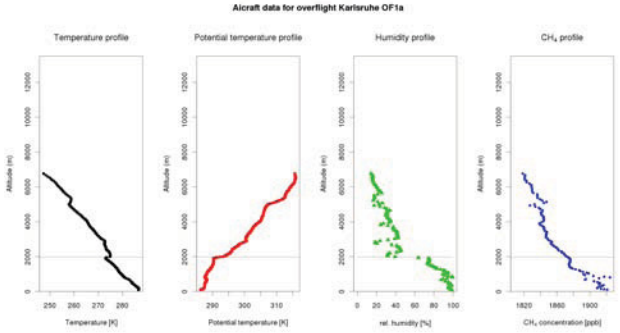

Figure E.12: Aircraft data of overflight Karlsruhe OF1a.

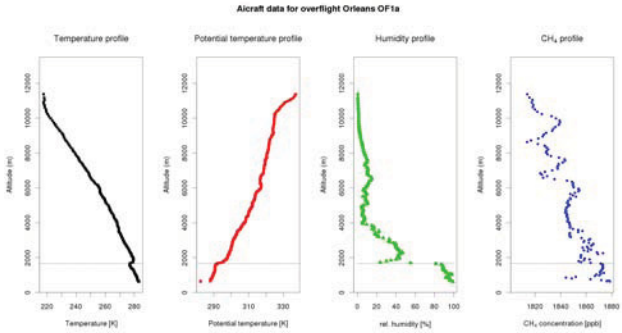

Figure E.13: Aircraft data of overflight Orleans OF1a.

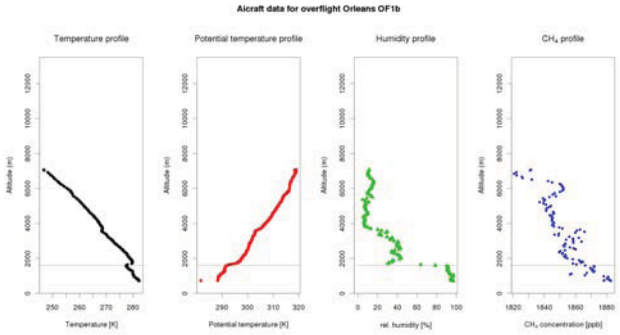

Figure E.14: Aircraft data of overflight Orleans OF1b.

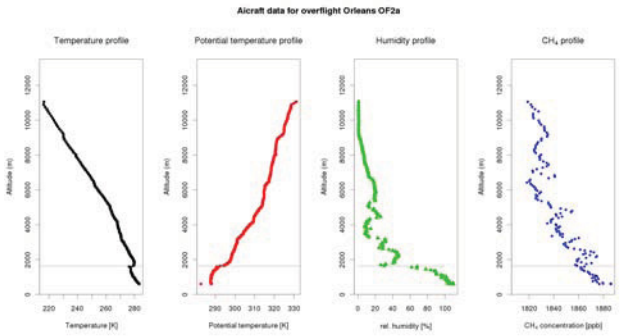

Figure E.15: Aircraft data of overflight Orleans OF2a.

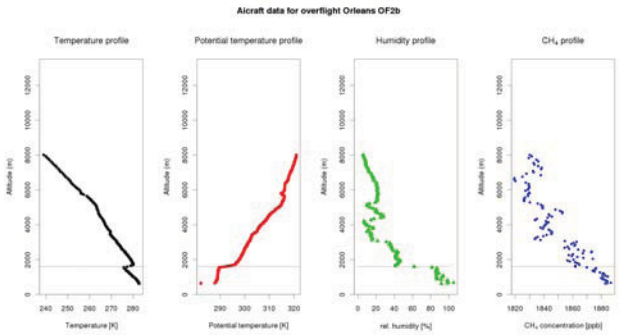

Figure E.16: Aircraft data of overflight Orleans OF2b.

Appendix F

Extension of the aircraft data to total columns

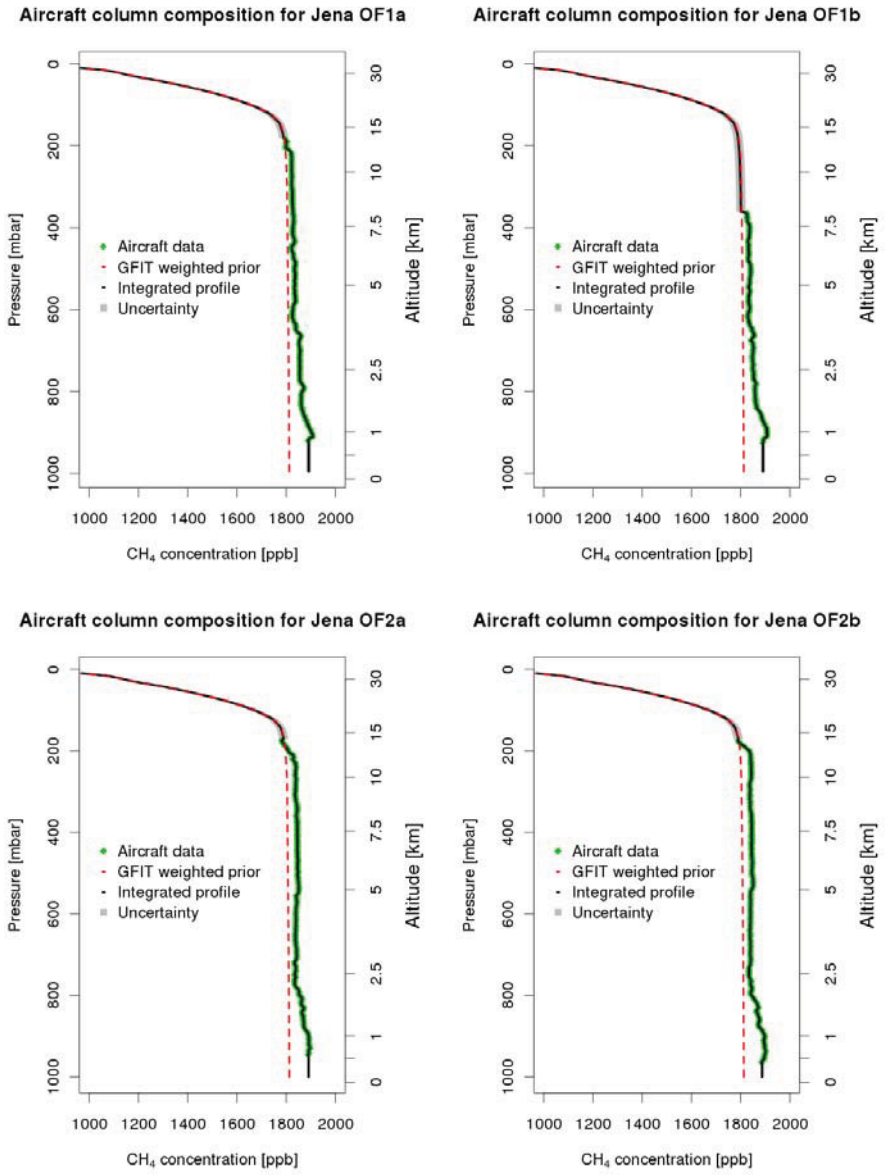

Figure F.1: Contribution to the extension of the aircraft profiles for the individual overpasses for Jena. The green partial column represent the aircraft in-situ data. This column was extended by the weighted GFIT a-priori in the stratosphere. The lower part was extended to the ground by adding ground-based in-situ data where available. Otherwise the profile was extrapolated to the surface. The grey area represent the uncertainty of the extended parts. The red line represents the weighted GFIT a-priori profile.

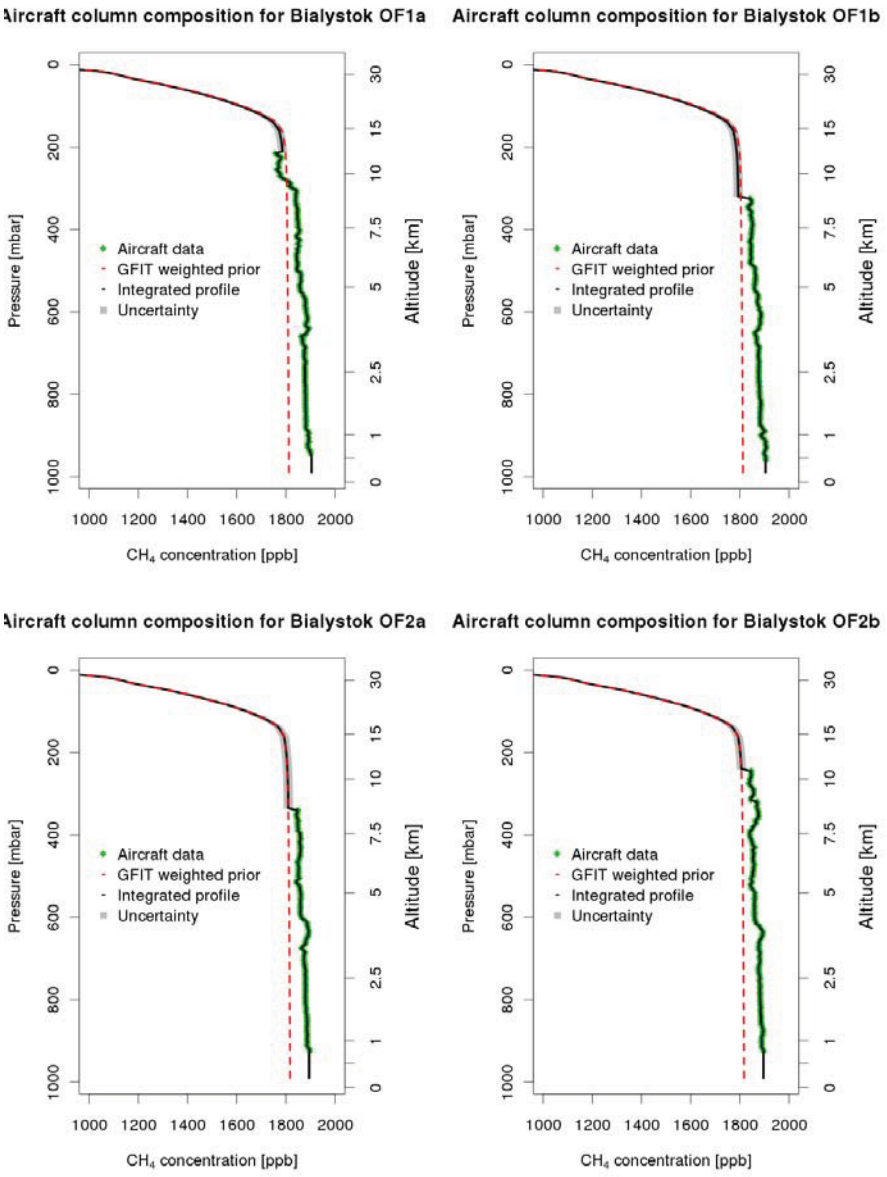

Figure F.2: Same as F.1 but for the individual overpasses for Bialystok.

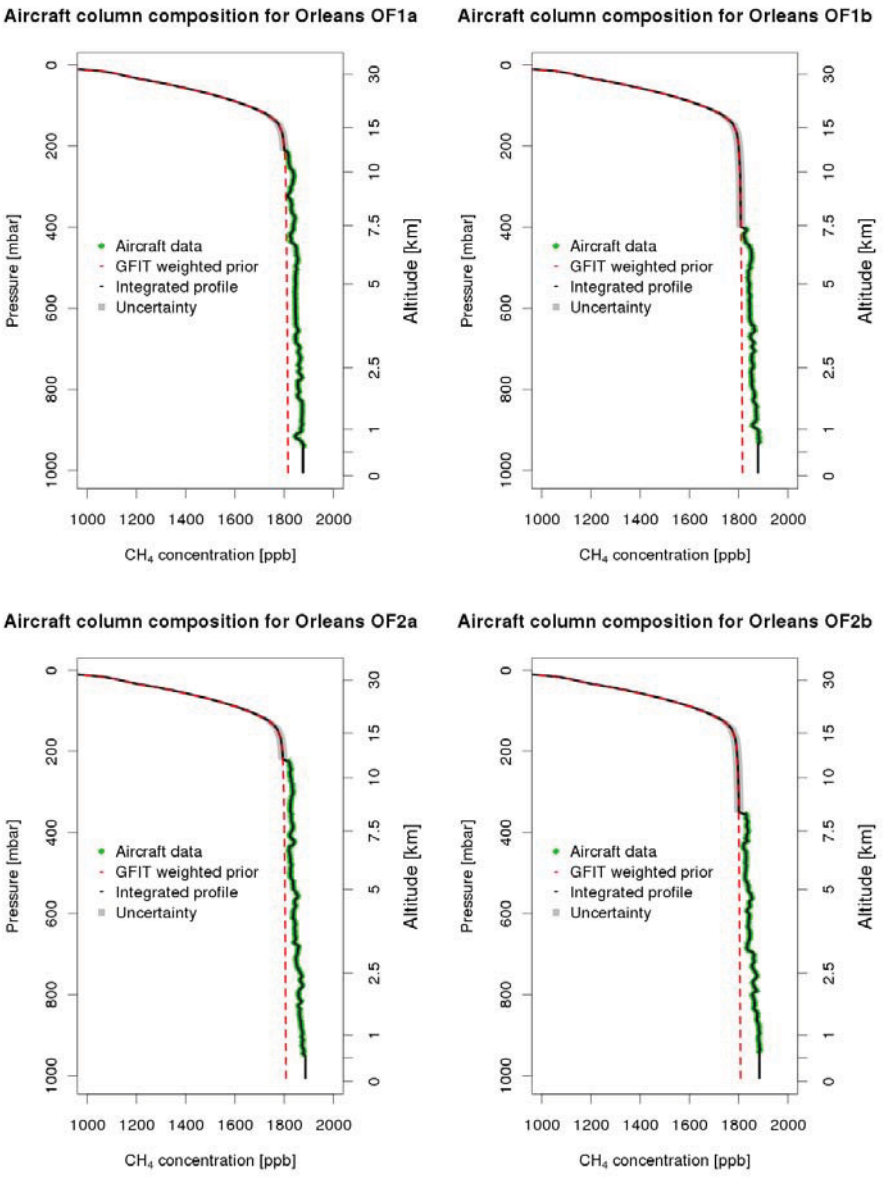

Figure F.3: Same as F.1 but for the individual overpasses for Orleans.

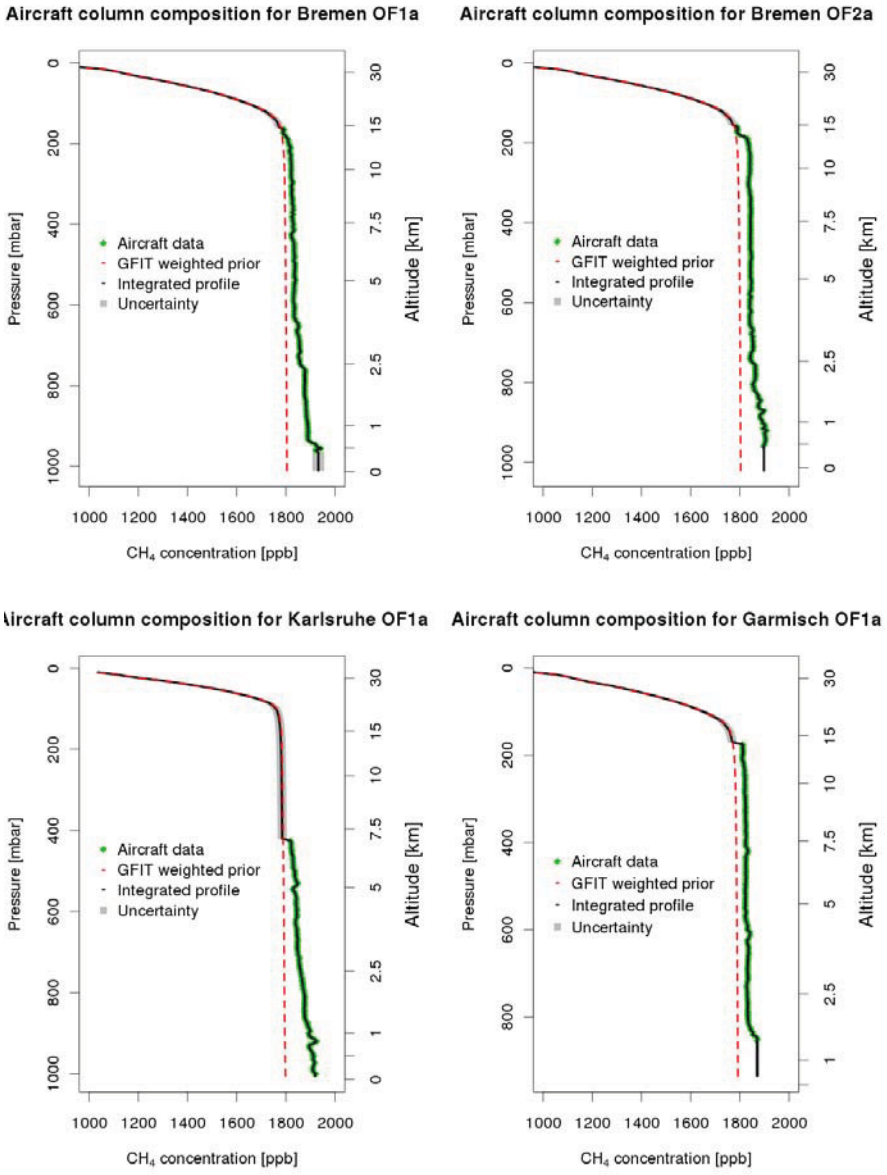

Figure F.4: Same as F.1 but for the individual overpasses for Bremen, Karlsruhe and Garmisch.

Appendix G

Least squares fit

The method iteratively minimizes the weighted residuals in both x and y. The x- and y- errors are assumed independent. The weight function is based on the assigned x and y uncertainty vectors.
The equations (1) – (4) are used to determine the slope, intercept and the corresponding errors according to York et al. (2004). Equation (G.2) must be solved iteratively.

$$a = \bar{Y} - b\bar{X} \tag{G.1}$$

$$b = \frac{\sum W_i \beta_i V_i}{\sum W_i \beta_i U_i} \tag{G.2}$$

$$\sigma_a^2 = \frac{1}{\sum W_i} + \bar{x^2}\sigma_b^2 \tag{G.3}$$

$$\sigma_b^2 = \frac{1}{\sum W_i u_i^2} \tag{G.4}$$

with:

- a,b = y-intercept and slope for the best line, $y = a + bx$
- $\bar{Y}$,$\bar{X}$ = weighted averages of the observed values X_i and Y_i
- W_i – weight function

- β_i – defined below (point 5.)
- V_i,U_i – residuals for x and y
- σ_a,σ_b – LSE standard errors of the intercept and slope
- $\bar{x}$ – adjusted weighted average for x

Calculation sequence

Note: the index i refers to the element i of the data vectors X and Y, and it is not the iteration index.

1. Calculate an initial value of b by ordinary least squares method
2. Determine the partial weights $\omega(X_i)$ and $\omega(Y_i)$ for each of the measurement points,based on the assigned uncertainty vectors σ_x and σ_y:

$$\omega(X_i) = \frac{1}{\sigma_x^2} \tag{G.5}$$

$$\omega(Y_i) = \frac{1}{\sigma_y^2} \tag{G.6}$$

3. Compute the weight function W_i for each point based on the weights $\omega(X_i)$ and $\omega(Y_i)$ and the last estimated slope b:

$$W_i = \frac{\omega(X_i)\omega(Y_i)}{\omega(X_i)b^2\omega(Y_i)} \tag{G.7}$$

4. Calculate $\bar{X}$ and $\bar{Y}$ using the observed points (X_i, Y_i), and W_i

$$\bar{X} = \frac{\sum W_i X_i}{\sum W_i} \tag{G.8}$$

$$\bar{Y} = \frac{\sum W_i Y_i}{\sum W_i} \tag{G.9}$$

5. Calculate U_i, V_i and β_i

$$U_i = X_i - \bar{X} \tag{G.10}$$

$$V_i = Y_i - \bar{Y} \tag{G.11}$$

$$\beta_i = W_i \left[\frac{U_i}{\omega(Y_i)} + \frac{bV_i}{\omega(X_i)} \right] \tag{G.12}$$

6. Calculate a new value for b, using equation (G.2) and the last estimated W_i, U_i, V_i and β_i

7. Use the new b and repeat the steps 3, 4, 5 and 6 until successive estimates of b agree within a chosen tolerance (in this case the tolerance was set at 10^{-6})

8. From the final values of b, $\bar{X}$ and $\bar{Y}$ calculate a using equation (G.1)

9. For each point X_i calculate the adjusted values x_i

$$x_i = \bar{X} + \beta_i \tag{G.13}$$

10. From x_i and W_i calculate $\bar{x}$ and u_i

$$\bar{x} = \frac{\sum W_i x_i}{\sum W_i} \tag{G.14}$$

$$u_i = x_i - \bar{x} \tag{G.15}$$

11. From W_i , $\bar{x}$ and u_i calculate σ_a and σ_b using the equations (G.4), respective (G.3)

Appendix H

Meteorology data of the Australia campaign

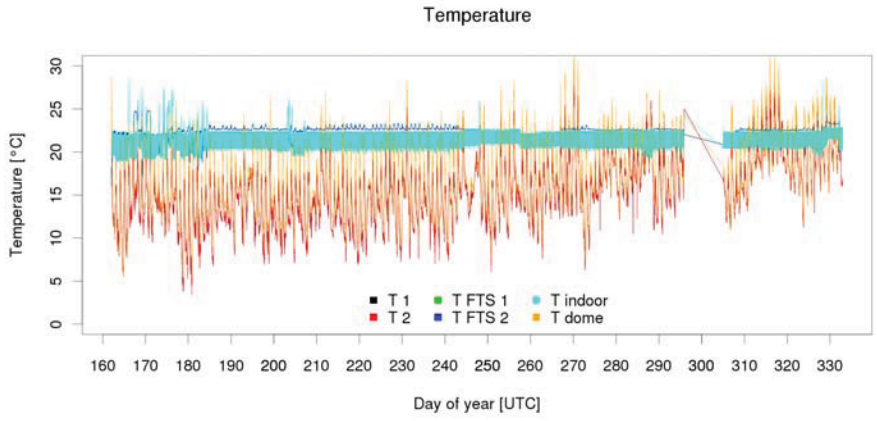

Figure H.1: Time series of the temperature measurements at the Jena FTS site taken with the sensors of the weather station.

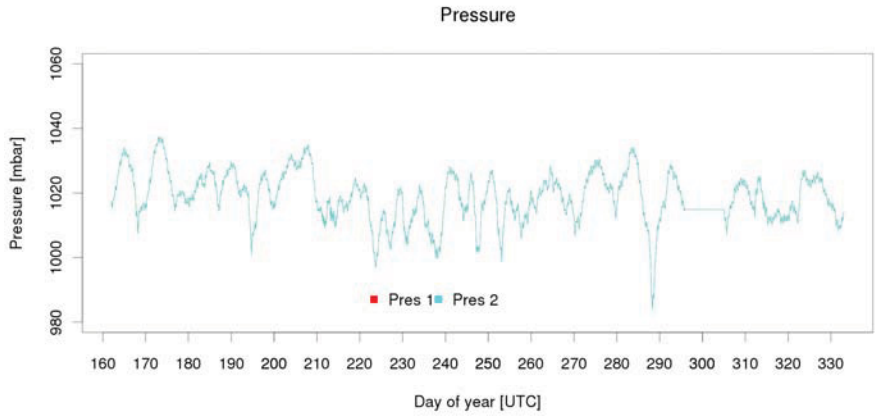

Figure H.2: Time series of the pressure measurements at the Jena FTS site taken with the sensors of the weather station.

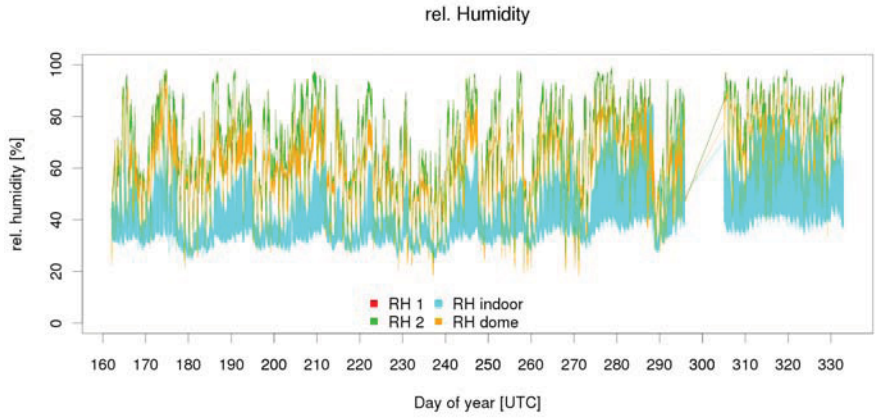

Figure H.3: Time series of the pressure humidity at the Jena FTS site taken with the sensors of the weather station.

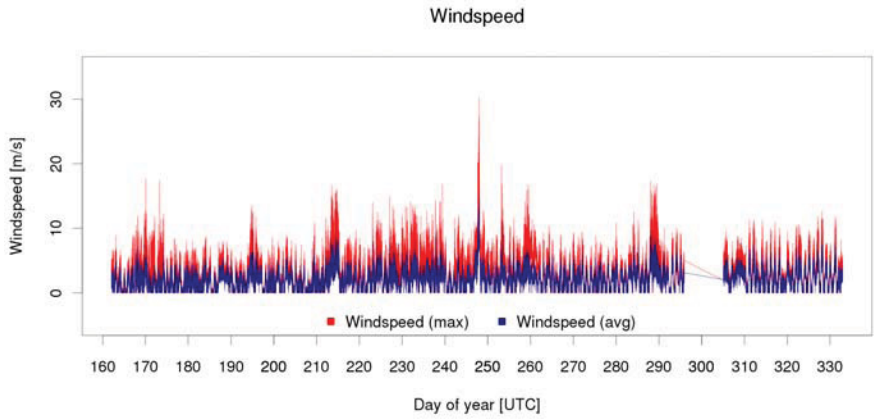

Figure H.4: Time series of the windspeed measurements at the Jena FTS site taken with the sensors of the weather station.

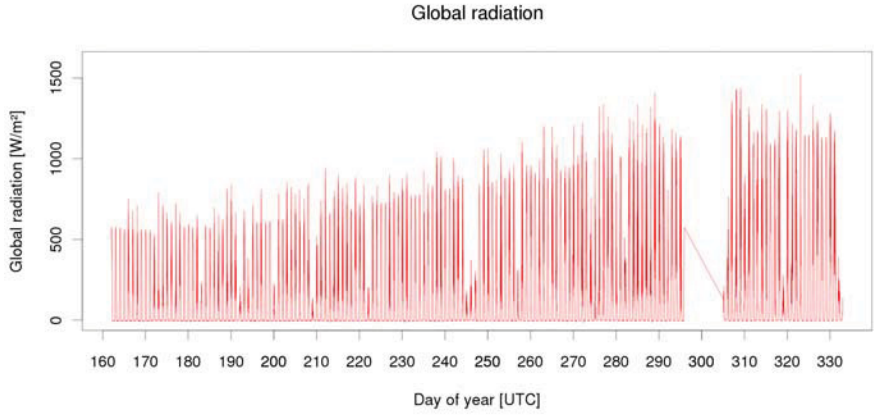

Figure H.5: Time series of the global radiation measurements at the Jena FTS site taken with the sensors of the weather station.